DLR-IB-AE-GO-2023-95

Gust Load Prediction on Supersonic Fighter Aircraft using Aerodynamic Panel Methods

Bachelor Thesis

Jan Baier

Institute of Aeroelasticity
Göttingen

DLR Deutsches Zentrum für Luft- und Raumfahrt

Document Properties

Title	Gust Load Prediction on Supersonic Fighter Aircraft using Aerodynamic Panel Methods
Subject	Bachelor Thesis
Institute	Institute of Aeroelasticity
Compiled by	Jan Baier
Participants	
Checked by	Dr.-Ing. Arne Voß Arne Voß Digital signiert von Arne Voss DN: C=DE, S=Nordrhein-Westfalen, L=Koeln, O=Deutsches Zentrum fuer Luft- und Raumfahrt e.V. (DLR), SN=Voss, G=Arne, CN=Arne Voss Grund: Ich habe dieses Dokument geprüft Ort: Datum: 2024.01.16 09:46:18+01'00' Foxit PDF Reader Version: 2023.2.0
Release by	Prof. Dr.-Ing. Wolf Reiner Krüger W. Krüger Digital signiert von Wolf-Reiner Krueger DN: C=DE, O=Deutsches Zentrum fuer Luft- und Raumfahrt e.V. (DLR), SN=Krueger, G=Wolf-Reiner, CN=Wolf-Reiner Krueger Grund: Ich genehmige dieses Dokument Ort: Datum: 2024.01.16 09:55:19+01'00' Foxit PDF Editor Version: 13.0.1
Date	01. December 2023
Version	1.0
File Path	

Chair of Aircraft Design
Lehrstuhl für Luftfahrtsysteme

Gust Load Prediction on Supersonic Fighter Aircraft using Aerodynamic Panel Methods

Bachelor Thesis

Submitted in partial fulfillment of the requirements for the degree B.Sc. Mechanical Engineering at the TUM School of Engineering and Design of the Technical University of Munich.

Supervised by	Prof. Dr.-Ing. Mirko Hornung Fanglin Yu, M.Sc. Chair of Aircraft Design
Submitted by	Jan Baier Student ID: 03723697

Submitted on	01. December 2023
Sequential number	**LS-BA 23/06**

Abstract

Military supersonic fighter configurations, due to their high maneuverability requirements, are usually sized through maneuver loads. This work investigates if gusts can exert higher loads on the main structure and outer wing areas as well, possibly exceeding the maneuver loads. In order to determine whether gust loads need to be considered as a design criterion for supersonic combat aircraft, this work presents a comprehensive gust load analysis at different flight conditions within the sub- and supersonic regime. For this, mission profiles, certification requirements, and current research outcomes are assessed and gust load computations using aerodynamic panel methods are executed at the example of the DLR Future Fighter Demonstrator configuration. As the aircraft is naturally unstable within the subsonic regime, a simplified pitch controller is implemented to allow for feasible closed-loop time domain simulations.

The results of the gust load campaign suggest that the quasi-steady method is not able to accurately predict the gust loads acting on a supersonic combat aircraft, significantly falling short of the dynamic gust loads. Although the maneuver loads envelope is generally larger for positive loads, negative peak bending moments exceed the maneuver loads and may thus be a sizing factor for the aircrafts lower skin. High accelerations due to short gust impacts can be observed on the wing tips, possibly sizing payload and attachment points.

Keywords: aeroelastic analysis, gust loads, supersonic combat aircraft, panel methods, feed-back control

Kurzfassung

Aufgrund ihrer hohen Anforderungen an die Manövrierfähigkeit werden militärische Überschallkampfflugzeugkonfigurationen in der Regel durch Manöverlasten dimensioniert. In dieser Arbeit wird untersucht, ob Böen derart hohe Lasten auf die Hauptstruktur und die äußeren Flügelbereiche ausüben können, sodass sie möglicherweise über die Manöverlasten hinausgehen. Um zu entscheiden, ob Böenlasten als Auslegungskriterium für Überschallkampfflugzeuge zu berücksichtigen sind, wird in dieser Arbeit eine gründliche Analyse der Böenlasten unter verschiedenen Flugbedingungen im Unter- und Überschallbereich durchgeführt. Hierfür werden die Missionsprofile, Zulassungsanforderungen und aktuelle Forschungsergebnisse bewertet und Böenlastberechnungen mithilfe von aerodynamischen Panelmethoden anhand der DLR Future Fighter Demonstrator Konfiguration durchgeführt. Da militärische Kampfflugzeuge üblicherweise im Unterschallbereich von Natur aus instabil sind, wird ein vereinfachter Nick-Regler implementiert, um physikalisch sinnvolle closed-loop Zeitbereichssimulationen zu ermöglichen.

Die Ergebnisse der Böenlastkampagne veranschaulichen, dass die quasistationäre Methode die auf ein Überschallkampfflugzeug einwirkenden Böenlasten nicht exakt vorhersagen kann und deutlich unter den dynamischen Böenlasten liegt. Obwohl der Bereich der Manöverlasten für positiven Schnittlasten im Allgemeinen größer ausfällt, überschreiten die negativen Biegemomente über den Flügel hinweg die Manöverlasten und können somit einen Faktor bei der Dimensionierung der aerodynamischen Struktur auf der Unterseite des Flügels darstellen. An den Flügelspitzen treten vermehrt hohe Beschleunigungen durch kurze Böen auf, welche einen möglichen Einfluss auf die Dimensionierung von Nutzlast und Befestigungspunkten haben können.

Stichwörter: Aeroelastische Analyse, Böenlasten, Überschall-Kampfflugzeuge, Panel-Methoden, Feed-Back-Regelung

Table of Contents

Abstract II

Kurzfassung IV

List of Figures VIII

List of Tables X

Nomenclature XI

1. Motivation and Outline 1
- 1.1. Motivation 1
- 1.2. Thesis Outline 3

2. Theoretical Background and Literature Review 5
- 2.1. Background of Gust Response Analysis and Certification Requirements 5
- 2.1.1. Quasi-static Methods 6
- 2.1.2. Transient Methods 11
- 2.1.3. Continuous Turbulence Methods 15
- 2.2. State-of-the-Art in Gust Load Analysis for Military Configurations 16
- 2.3. Deflection Rate Limits 19
- 2.4. Objectives and Scientific Contribution 22

3. Applied Methodology on the Future Fighter Demonstrator 25
- 3.1. Characteristics of the Configuration 25
- 3.2. Steady and Unsteady Aerodynamics 26
- 3.3. Structural and Mass Model 28
- 3.4. Modal Analysis and Equations of Motion 30
- 3.5. Dynamic Gust Simulation and Trim Conditions 35
- 3.6. Operating Points 36
- 3.7. Deflection Rate Limits 44

4. Control System Development 45
- 4.1. The Necessity for a Flight Control System 45
- 4.2. Analysis Methodology and Derivation of Gains 50
- 4.3. Proposed Architecture for a Simplified Stability Augmentation System 55
- 4.4. Intermediate Results of the Stability Augmentation System 64

5. Gust Load Analysis on the DLR-FFD Configuration 71
5.1. Quasi-steady Gust Load Analysis 71
5.2. Transient 1-cos Gust Load Analysis 73
5.3. Comparison to Maneuver Loads 77
5.4. Accelerations due to Gust Impact 78

6. Conclusion and Outlook 85
6.1. Conclusion 85
6.2. Outlook 86

Bibliography 87

List of Figures

Figure 1.1: The DLR Future Fighter Demonstrator, CPACS file visualized in the TiGL Viewer 2
Figure 2.1: Basic step gust 6
Figure 2.2: Comparison of the knock-down factor for the sub- and supersonic regime 8
Figure 2.3: Shape and velocity of the basic 1-cos gust 8
Figure 2.4: Comparison of reference gust velocities given in CS23 and MIL-A-8861B 10
Figure 2.5: Comparison of reference gust velocities given in CS23, MIL-A-8861B and CS25 12
Figure 2.6: Gust appearance at sea-level and Fg=1.0 according to CS25 13
Figure 2.7: Depiction of turbulent air and derived approximation of a 1-cos gust 15
Figure 3.1: Discretization of a lifting surface using the DLM 26
Figure 3.2: Aerodynamic mesh for DLM & ZONA51 including correction for camber and twist (indicated by color) 27
Figure 3.3: Structural model of the DLR Future Fighter Demonstrator, extracted from [76] 28
Figure 3.4: Mass configurations M1-M4 of the FFD 29
Figure 3.5: DLR FFD M2, Mode 1 31
Figure 3.6: DLR FFD M2, Mode 2 31
Figure 3.7: DLR FFD M2, Mode 3 31
Figure 3.8: DLR FFD M2, Mode 4 32
Figure 3.9: DLR FFD M2, Mode 5 32
Figure 3.10: DLR FFD M2, Mode 6 32
Figure 3.11: DLR FFD M2, Mode 7 33
Figure 3.12: DLR FFD M2, Mode 8 33
Figure 3.13: DLR FFD M2, Mode 9 33
Figure 3.14: DLR FFD M2, Mode 10 34
Figure 3.15: Monitoring stations used for the loads analysis on the FFD 35
Figure 3.16: Design velocities and example maneuver envelope for the FFD; civil and military notation 38
Figure 3.17: Comparison of gust velocities for large gust gradients 39
Figure 3.18: Flight profile alleviation factor Fg of the DLR FFD and the DLR XRF1 40
Figure 3.19: Turbulence severity and exceedance probability, extracted from [23] 41
Figure 3.20: Vertical 1-cos gust 43
Figure 4.1: Location of the aerodynamic center for the subsonic and supersonic flight state 46
Figure 4.2: Response of pitch angle Θ, load factor Nz and pitch rate q to a range of gusts in both stability configurations 47
Figure 4.3: Eigenvalues and modal participation, M2, FL000, Ma04-Ma06 49
Figure 4.4: Pilot assessment of handling qualities for different characteristics of the short period mode, derived from [7] 51

Figure 4.5: Transfer function for a step input of one, using the optimal values ζ_opt and ω_opt in comparison with the upper and lower limits for ζ_required of flight phase 1 52
Figure 4.6: Pole comparison of the reduced 2DoF system to the full system 53
Figure 4.7: Comparison of aircraft behavior to a step input with current gains compared to the ideal behavior.. 54
Figure 4.8: SAS to control longitudinal instability of the DLR FFD configuration allowing for feasible gust analysis calculations 55
Figure 4.9: Example V-n diagram depicting the location of the corner point....................................... 56
Figure 4.10: Control architecture for the outer attitude control loop 58
Figure 4.11: Derived gains for the attitude control.. 59
Figure 4.12: Control architecture for the outer pitch control loop... 60
Figure 4.13: Derived gains for the pitch control... 61
Figure 4.14: Control architecture for the outer actuator control loop 62
Figure 4.15: Derived gains for the actuator control 63
Figure 4.16: Transfer function of closed-loop system in the unstable subsonic regime after 750 generations... 64
Figure 4.17: Transfer function of closed-loop system in the stable supersonic regime after 750 generations... 65
Figure 4.18: Comparison of the open loop and close loop responses for different gust impacts 67
Figure 4.19: Loads acting on the wing root of the FFD, comparing open loop and closed loop loads ... 68
Figure 4.20: Loads acting on the horizontal tale plane of the FFD, comparing open-loop and closed-loop loads 69
Figure 5.1: Quasi-steady Pratt gust loads.. 72
Figure 5.2: Comparison of different gust gradient sets for the transient 1-cos gust analysis 73
Figure 5.3: Transient 1-cos gust loads 74
Figure 5.4: Comparison of quasi-steady Pratt gust loads and transient 1-cos gust loads 75
Figure 5.5: Comparison of maneuver loads and gust loads 77
Figure 5.6: Accelerations at various sections of the aircraft, gust with $H = 9\ m$ and $0°$ inclination 79
Figure 5.7: Accelerations at various sections of the aircraft, gust with $H = 56\ m$ and $0°$ inclination... 80
Figure 5.8: Accelerations at various sections of the aircraft, gust with $H = 56\ m$ and $180°$ inclination 81
Figure 5.9: Accelerations at various sections of the aircraft, gust with $H = 107\ m$ and $0°$ inclination. 82

List of Tables

Table 2.1: Comparison of flight speed notations for civil and military aircraft...................................... 11
Table 2.2: Gust gradients and corresponding peak velocities depicted in Figure 2.6............................ 13
Table 2.3: Comparison of gust load certification requirements 14
Table 2.4: Deflection rate limits for various control surfaces and aircraft configurations 21
Table 3.1: Overview of the DLR Future Fighter Demonstrator (FFD) key design parameters, reproduced from [31].. 25
Table 3.2: Overview of mass configurations 29
Table 3.3: Considered altitudes during the gust load campaign.. 37
Table 3.4: Mass ratio µg and knock-down factor Kg for both subsonic and supersonic regimes........... 39
Table 3.5: Selected gust gradient sets for the dynamic analysis.. 42
Table 3.6: Overview of gust load cases 43
Table 3.7: Control surface deflection limits of the F-22 Raptor, extracted from [99] 44
Table 4.1: Comparison of static margin for subsonic and supersonic flight states................................ 46
Table 4.2: Aircraft categories and characteristics as specified by MIL-F-8785C 50
Table 4.3: Relative damping requirements ζ_required according to Flight phase and level of Flying qualities as specified by MIL-F-8785C 50

Nomenclature

Abbreviations

AGARD	NATO Advisory Group for Aerospace Research and Development
BFDM	Basic Flight Design Mass
CAP	Combat Air Patrol
CAS	Close Air Support
CFD	Computational Fluid Dynamics
DLM	Doublet Lattice Method
DLR	Deutsches Zentrum für Luft- und Raumfahrt
DoF	Degree of Freedom
EASA	European Aviation Safety Agency
EFCS	Electronic Flight Control System
EOM	Equation of Motion
FAA	Federal Aviation Administration
FE	Finite Element
FFD	Future Fighter Demonstrator
FL	Flight Level
FPA	Flight Profile Alleviation
FSM	Force Summation Method
GLA	Gust Load Alleviation
HGM	Harmonic Gradient Method
LABS	Low Altitude Bombing Systems
MTOM	Maximum Take Off Mass
NACA	National Advisory Committee for Aeronautics
NATO	North Atlantic Treaty Organization
OCA	Supersonic Intercept
OEM	Operational Empty Mass

OP	Optimal Performance	
PIO	Pilot Induced Oscillation	
RFA	Rational Function Approximation	
RTO	NATO Research and Technology Organization	
SAS	Stability Augmentation System	
SEAD	Suppression of Enemy Air Defense	
SM	Static Margin	
SMT	Shear-Moment-Torque	
TLAR	Top-Level Aircraft Requirements	
VGH	Vertical-Acceleration-Altitude	
VLM	Vortex Lattice Method	

Variables and Parameters

Latin

AC	Aerodynamic center	
AIC	Matrix of aerodynamic influence coefficients	
CG	Center of gravity	
F_z	Shear force	N
H	Gust gradient	m
$K_{P,I,D}$	PID-Controller coefficients	
Ma	Mach number	
MAC	Mean aerodynamic chord	m
M_x	Bending moment	Nm
M_y	Torsional moment	Nm
N_z	Load factor	
U	Gust velocity	m/s
V	Onflow velocity	m/s
c_{ref}	Reference length	m
p, q, r	Angular rates in flight physical coordinate system	rad/s

q_∞	Dynamic pressure	Pa
s	Complex Laplace variable	
t	Time	s
u	Nodal displacement vector	m, rad
u, v, w	Velocities in flight physical coordinate system	m/s
x, y, z	Position in inertial coordinate system	m

Greek

α	Angle of attack	$°, rad$
θ	Pitch angle	$°, rad$
Φ	Eigenvector	
η	Elevator deflection	$°, rad$
λ	Eigenvalue	
ρ	Air density	Pa
ω	Angular rate	rad/s

1. Motivation and Outline

1.1. Motivation

Maximizing the performance and safety of supersonic fighter jets is crucial. Fighter jet pilots experience significant physical and mental strain both during routine flights and particularly during combat action. Especially in combat situations, maintaining a sharp focus on the ever-changing environment is essential, and worrying about allowable maneuver loads in turbulent air should not be an active concern for the pilot. They must trust that sudden gust impacts will not result in immediate transgression of the pilots' limit loads nor structural damage.

To the author's best knowledge, there are only limited number of publications concerning the wide field of gust load analysis for supersonic fighter aircraft. Most of the available publications consider gust computations to be less significant than maneuver loads due to the very high agility requirements set for combat maneuvers. However, contrasting views from other publications suggest that gusts are potentially influencing the structural sizing of specific parts of the aircraft such as wingtips, attachments and payload. Additionally, with climate change leading to larger gust loads on aircraft [67] in turbulent air, precisely predicting gust loads is becoming increasingly vital for ensuring aircraft safety and overall flight performance in various weather conditions.

Although gust computations are a familiar topic, computing gust loads accurately has been a long-standing point of content. To identify critical points in the envelope, which and how many gust loads should be explored? Are quasi-steady methods, which are the required method for certifying combat aircraft, capable of providing satisfactory results? Are the underlying assumptions made in the certification requirements viable for all configurations and mission profiles? Reasoning behind certification requirements is often opaque, and it is unclear which assumptions accurately determine the correct gust loads of a considered configuration. Wrong assumptions can thus lead to wrong results. According to extensive literature, gust load certification for military aircraft often falls short of civil requirements. Although some publications suggest that quasi-static gust load methods are unsuitable for military supersonic jets, they remain the only required discrete gust method (apart from continuous turbulent gust models) according to the US military standard MIL-A-8861. Furthermore, various publications suggest that transient elastic gust analysis is the industry standard at most defense companies involved in the production of fighter jets.

Motivated by the investigation of aeroelastic behavior and characteristics of supersonic combat aircraft, a conceptual design for a supersonic future fighter aircraft is developed within an DLR-intern project. Figure 1.1 presents the DLR Future Fighter Demonstrator (FFD).

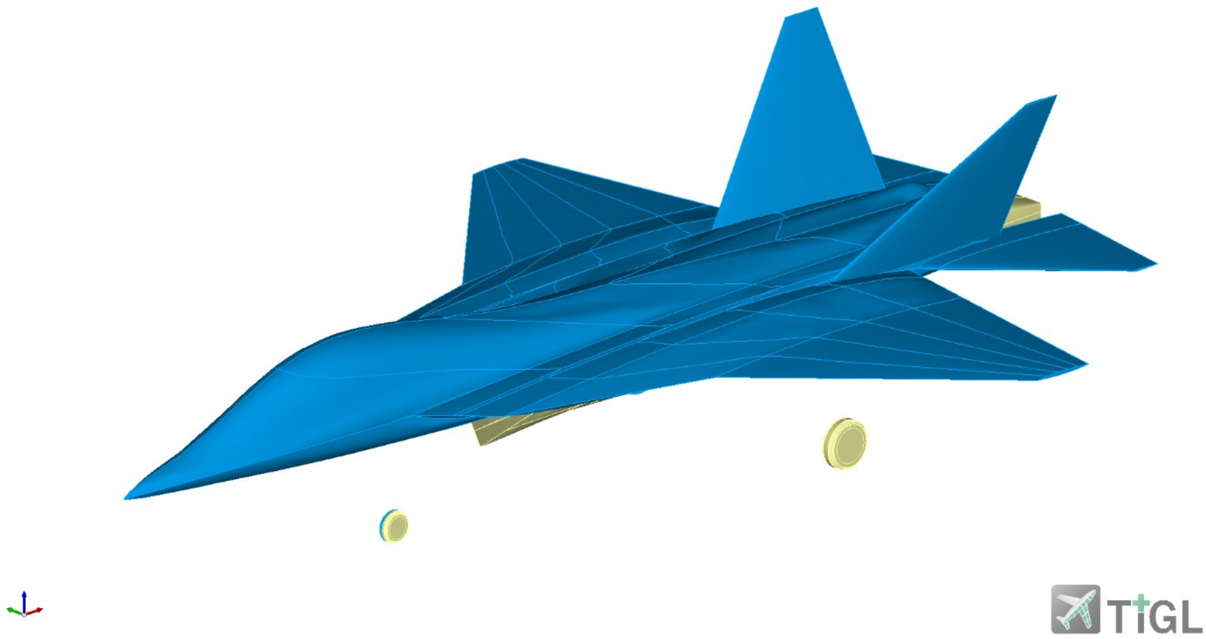

Figure 1.1: The DLR Future Fighter Demonstrator, CPACS file visualized in the TiGL Viewer

Structural sizing has been determined through maneuver load analysis, but evaluating the gust loads is still necessary for a comprehensive aeroelastic analysis. As gust loads have not yet been studied on this configuration, the question of whether gust loads could impact certain parts of the configuration structure is yet to be resolved. Typically, combat aircraft are longitudinally unstable due to the aerodynamic center (AC) being placed in front of the center of gravity (CG) in the subsonic regime, thus the AC having a large travel distance across different Mach numbers. This renders gust load computations unfeasible if no longitudinal stability augmentation system is incorporated, as the aircraft will diverge upon gust impact and the simulations will produce only nonphysical load results. However, at the preliminary design stage, the model does not yet incorporate an electronic flight control system (EFCS).

1.2. Thesis Outline

Chapter two will discuss and explain different methods and models used in gust load analysis, ranging from empirical quasi-static approaches based on statistical data to more sophisticated physical methods such as dynamic analysis using FEM. The methods are followed by the review of available publications on the subject of gust loads on military combat aircraft. These will be used to establish fundamental research areas that the author will explore in this work. Subsequently, available data on deflection rate limits for control surfaces is briefly summarized, as these values are crucial for the implementation of a realistic control system architecture that encapsulates real aircraft behavior. Chapter three provides an overview of the applied methodology by means of the reference aircraft configuration including mass and aerodynamic models for the gust load computations. Combining the data extracted from the literature review with the presented characteristics of the configuration, the gust load assumptions and operating points are discussed. Chapter four will focus on the development of a stability augmentation system to make gust computations on this model physically meaningful. The necessity for the control system will be discussed, along with several approaches for the derivation of the gains and their subsequent validation. Chapter five presents the results of the gust load campaign. A comparison between quasi-static, transient and maneuver loads will be made. Subsequently, the vertical accelerations are extracted at several points of the aircraft and compared to the specified load limits. Finally, the last chapter will draw a conclusion on the findings and discuss further research aspects on the topic of gust loads for supersonic combat aircraft.

2. Theoretical Background and Literature Review

Based on the motivation from chapter one, the following literature review aims to establish a comprehensive understanding of gust load simulations, gust load certification requirements for civil and military aviation as well as the state-of-the-art in gust load analysis and flying characteristics for military configurations.

2.1. Background of Gust Response Analysis and Certification Requirements

Effects of atmospheric turbulence on aircraft have been a continuous target of studies since the early days of aeronautics, with the first published National Advisory Committee for Aeronautics (NACA) report in 1915 [102], where Wilson and Hunsacker underlined the technical interest of structural loads of aircraft during gust encounters. Indeed, even the North Atlantic Treaty Organization Advisory Group for Aerospace Research and Development (NATO AGARD) named gust loads to be one of their major concerns since its conception [39].

Throughout the years, extensive research has been conducted to improve the understanding and the quantification of the impact of gusts on aircraft structures. Accurate prediction of gust loads is crucial for maintaining the structural integrity of aircraft within safe boundaries, while also allowing for reasonable safety margins without oversizing the structure [76]. The Federal Aviation Administration (FAA) established uniform certification regulations in 1927 to guarantee the structural safety of aircraft during gusty conditions. Today, together with the European Union Aviation Safety Agency (EASA), it provides the most relevant certification guidelines for civil aircraft, while the US Department of Defense (US DoD) publishes certification requirements for military aircraft. Design and certification requirements dynamically change through time, continuously pushing fidelity in gust load analysis to better approximation of the real-life events. Similarly, certification requirements for gust load simulation have undergone constant modifications (such as the switch from quasi-steady to transient gust load analysis for large transport aircraft) due to acquired knowledge from previous events and empirical data, shifts in aircraft design principles, and advancements in computational power and analysis methods [29].

The gust load analysis methods specified in the certification requirements can be distinguished on their determinism and fidelity as: quasi-static, transient, and continuous turbulence. All methods estimate design maximum loads that potentially occur once in the service life of an aircraft [39]. All authorities still require a combination of static and continuous turbulence methods to cover all gust effects. No single method is appropriate for every case, as every turbulence model can be proved inaccurate under certain conditions [101]. A short examination of each of the above-mentioned categories is provided in the subsequent subsections. For more detailed information, the origin of turbulence in the atmosphere is illustrated by Brockhaus [10], Hoblit [37] provides a detailed summary of gust loads acting on aircraft, while Fuller [29] offers a complete overview of the background and design requirements for gust load certification.

2.1.1. Quasi-static Methods

Although turbulence is a naturally transient phenomenon, many reported accidents resulting in the total loss of an aircraft can be traced back to single upset gust events [29]. Based on this phenomenon, representing gusts as instantaneous static loads is a good initial approximation. Rhode and Lundquist first introduced the sharp-edge gust concept in 1931 [70], which forms the basis for quasi-static gust load analysis and laid the foundation of the first gust load regulation introduced in 1934 [53]. In the case of a sharp-edge gust, a rigid airplane experiences an instantaneous change in vertical velocity, modeled as a step function, with an intensity of U. The incremental lift due to the gust is given by the basic lift equation

$$\Delta L = \frac{1}{2}\rho V^2 S C_{L_\alpha} \Delta\alpha = \frac{1}{2}\rho V^2 S C_{L_\alpha}\, arctan\left(\frac{U_{de}}{V}\right) \tag{2.1}$$

where C_{L_α} is the lift curve slope, S the reference wing area and $\Delta\alpha$ the incremental angle of attack. Following this equation, the incremental vertical acceleration of the sharp-edge gust profile, also called load factor n, can simply be calculated by

$$\Delta n = \frac{\Delta L}{W} \tag{2.2}$$

Figure 2.1 shows the basic step gust impact and the resulting velocities on the aircraft.

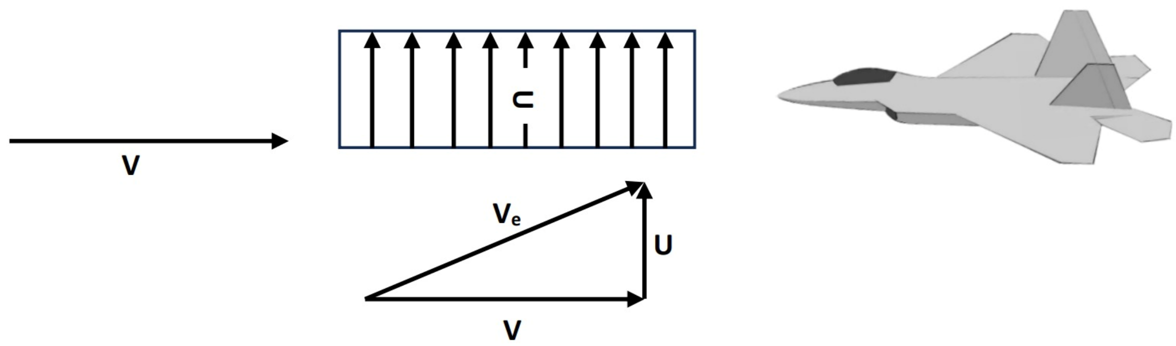

Figure 2.1: Basic step gust

Although a good initial approximation, this simple approach neglects unsteady aerodynamics due to gust penetration and vertical motion of the aircraft. With increasing speeds and wing loading, this basic model was no longer deemed satisfactory for newer generation aircraft anymore [29]. To account for these effects, including the characteristics of flexible aircraft, a revised gust formula was introduced. First published in NACA Report 1206 in 1953 by Pratt and Walker [65], also commonly referred to as the *Pratt-Method*, it constitutes as a revised model of the sharp edge gust and represents the dominant rational quasi-static method to this day.

Decoupling aeroelastic and flight dynamic responses, an Equation of motion (EOM) for the aircraft is set up within following assumptions:

I. The aircraft is a rigid body.
II. The aircraft forward speed is constant.
III. The aircraft is in steady level flight prior to entry into the gust.
IV. The aircraft can rise but cannot pitch.
V. The lift increments of the fuselage and horizontal tail are negligible in comparison with the wing lift increment.
VI. The gust velocity is uniform across the wingspan and is parallel to the vertical axis of the aircraft at any instant.

The basic EOM neglects the changes in forward velocity, pitch, pitch rates as well as transient lift forces. To account for the unsteady aerodynamic effects and the time lag in the build-up of aerodynamic lift, the Küssner unsteady lift function and the Wagner function are introduced. The Küssner function accounts for the lift delay caused by the gradual entry of the chord into the gust, whereas the Wagner function accounts for the impact of unsteady circulatory effects [18]. The motion is expressed as a single degree-of-freedom equation allowing only for plunge. To generalize the equation for different aircraft configurations, the dimensionless mass ratio

$$\mu_g = \frac{2(W/S)}{\rho c g C_{L_\alpha}} \tag{2.3}$$

is introduced into the EOM, with W denoting the aircraft weight, c being the mean aerodynamic chord and ρ the local air density.
By solving the resulting flight dynamic equation for a range of values μ_g, a knock-down factor K_g (2.4) for the original sharp-edge gust formula is obtained. Pratt introduced a curve fit approximation for this knock-down factor, utilizing the generalized mass ratio, to avoid recurring evaluation of the EOM for every new aircraft configuration. This knock-down factor K_g was derived for aircraft operating at subsonic speeds. In order to consider the distinct features of lift buildup that occur in supersonic regimes beyond the critical Mach number, a supersonic knock-down factor (2.5) is introduced in MIL-A-8861B [85].

$$K_{g_{subsonic}} = \frac{0.88\mu_g}{(5.3 + \mu_g)} \tag{2.4}$$

$$K_{g_{supersonic}} = \frac{{\mu_g}^{1.03}}{(6.95 + {\mu_g}^{1.03})} \tag{2.5}$$

Following Figure 2.2 compares both the subsonic and the supersonic knock-down factor K_g.

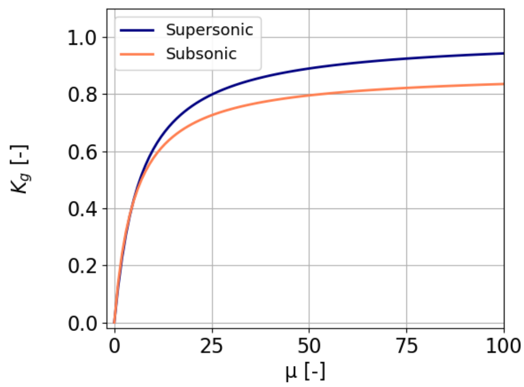

Figure 2.2: Comparison of the knock-down factor for the sub- and supersonic regime

The resulting incremental load factor acting on the aircraft center of gravity is therefore calculated by (2.6), which is superposed with the 1g level flight at considered design point to obtain the load acting on the aircraft.

$$\Delta n_z = \frac{K_g \rho_0 U_{de} V C_{L_\alpha}}{2(W/S)} \tag{2.6}$$

V denotes the current true airspeed. The gust speed U_{de} used in (2.1) and (2.6) describes a derived equivalent gust speed. The relationship between U_{de} and U_0 presented in Figure 2.3 is given through

$$U_{de} = U_0 \cdot \sqrt{\rho/\rho_0} \tag{2.7}$$

thus the subscript equivalent. The derived subscript comes from solving for U_{de} in (2.6), using flight data collected during operational flight. Hence, it does not represent an actual physical velocity, but a fictious gust velocity based on arbitrary assumptions derived from empirical data [37]. Accelerations through turbulent air encounters for aircraft operating in the subsonic regime were measured in several Airspeed, Vertical acceleration and Altitude (VGH) test campaigns. Each reference amplitude is assumed to result from a vertical acceleration caused by encountering a known-shape gust [6] as seen in Figure 2.3.

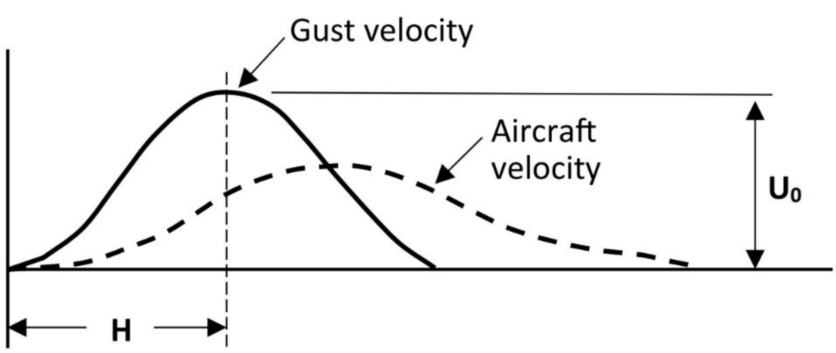

Figure 2.3: Shape and velocity of the basic 1-cos gust

Then, from these measurements, a relationship between gust probability and amplitude is derived. The results were empirically studied by Walker [98], Peckham [61] and Tolefson [83]. Later, the derivation of values for U_{de} was provided by Press [66]. Still, this data on reference gust velocities is only valid for subsonic aircraft. Love and Ehrenberger [50] studied gust velocities for aircraft operating in the supersonic regime. They found that gust occurrences at supersonic cruise altitude are more sporadic compared to those in the upper troposphere due to lower wind speeds and greater static stability caused by the near isothermal temperature profile. They concluded that, as the altitude increases, less time will be spent in turbulent air. This is supported by the data collected by Ehrenberger [23], who compiled gust velocity measurements of the considered research aircraft.
The specific gust velocity, incorporating the gust length $2H$ is

$$U = \frac{U_{de}}{2}(1 - cos\,(\frac{2\pi s}{2H})) \tag{2.8}$$

In the quasi-steady Pratt Method, the gust gradient H is assumed as 12.5 spatial chord lengths c, resulting in following equation for the specific gust velocity

$$U = \frac{U_{de}}{2}(1 - cos\,(\frac{2\pi s}{25c})) \tag{2.9}$$

The gust gradient is the distance penetrated into the gust until it reaches its peak velocity. Empirical data collected in the 1940s shows that the highest gust excitations on legacy aircraft occur at a gradient corresponding to 12.5 spatial chord lengths on average [18]. Hoblit [37] points out two reasons why chord lengths, rather than feet, were selected for this matter: Chord lengths were found to yield less scatter compared to feet when plotting gust velocity data over gradient distance, and secondly the calculation of K_g could be simplified by having a generalized measurement. The value of a gust gradient of 12.5 spatial chord lengths is not necessarily optimal for all configurations, but rather a convenient value based on averaged empirical data. Nevertheless, considering the quasi-static gust formula's insensitivity to varying gust gradients, this inaccuracy does not significantly affect the calculations [37]. Albeit certification for larger aircraft requires more rational analysis, exploration of large design envelopes during preliminary design still makes use of the Pratt method due to its ease of use, little computational power required, and shorter processing time compared to other methods.

Side note: Reference gust velocities are not the sole result of actual measurements. The selected gust velocities are determined by the acceleration measured during flight campaigns rather than the actual peak gust velocities. For instance, in the 1960 National Severe Storms Project [6]*, the derived peak gust velocity was 50 fps, while the maximum true vertical gust measured was 208 fps. This discrepancy can be attributed to the gust wavelength, which was greater than 25 chords, resulting in only minor acceleration on the aircraft, for which it was disregarded. Moreover, the reference gust velocities are also based on empirical considerations. Donely* [18] *developed the initial frequency distribution for the reference gust velocities based on the B-247 as the reference aircraft. The gust velocities were defined as "effective", derived from the solutions of the simple sharp-edge gust formula without including any alleviation factor. An alleviation factor K was later introduced to incorporate discrepancies in the response of other aircraft relative to the B-247. As many aircraft certified with the step gust method had flown safely for many years, historical data of these safe aircraft was taken into account while introducing the new certification method using the Pratt method. Therefore, reference gust speeds were* *selected so as to produce comparable incremental accelerations for both old and new certification methods* [37]*. This indicates that certification requirements are not always intended to precisely or extensively depict the real world, but to ensure that newly developed aircraft are built in a secure manner.*

The Pratt method is used by all certification authorities that require a quasi-steady simulation approach, including the certification of small commuter aircraft by the European Aviation Safety Agency's (EASA) CS23 [21], the Federal Aviation Administration's (FAA) FAR23 [21], and the certification of military aircraft under MIL-A-8861B [85]. It is also described as a method for structural load dimensioning by JSSG-2006 [84] and MIL-STD-1797 [89]. However, civil and military authorities have imposed different reference gust velocities for this method.
The reference gust velocities are defined in CS23.333 (c)(1), and MIL-A-8861B 3.5.1.1 respectively. The reference gust velocities in these documents are derived through different directives and can be compared in Figure 2.4.

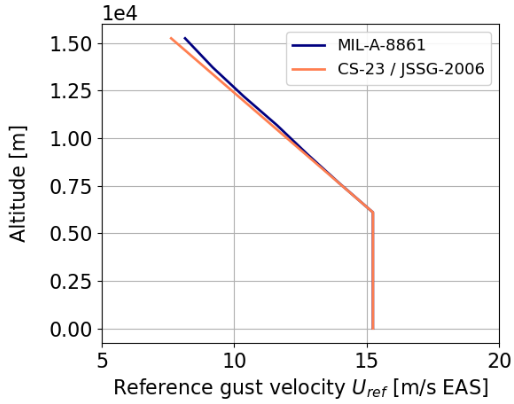

Figure 2.4: Comparison of reference gust velocities given in CS23 and MIL-A-8861B

The gust speed is defined in CS23 as follows: For cruise speed VC, U_{ref} equals 15.24 m/s at sea level to an altitude of 6096 meters and linearly decreases to 7.62 m/s between 6096 and 15240 meters. At dive speed VD, U_{ref} is halved concerning the specified value for VC for probabilistic reasons. Conversely, MIL-A-8861B defines U_{ref} at cruise speed VC to be 15.24 m/s at sea level until 6096 meters. Beyond this height, the reference gust velocity is reduced by a factor that varies with air density and can be found in Table 2.3. At dive speed VD, U_{ref} is halved concerning the specified value for VC for probabilistic reasons.
According to MIL-A-8861B, flight speeds are indicated in a different notation, albeit the underlying definitions are congruent. Following Table 2.1 compares the civil and military notations. In this work, speeds will solely be indicated in the civil notation to facilitate readability.

Table 2.1: Comparison of flight speed notations for civil and military aircraft

Civil Notation	Definition	Military Notation	Definition
VA	Design maneuvering speed	VE	Minimum speed to attain design limit load factor
VC	Design cruise speed	VH	Maximum speed for level flight
VD	Design dive speed	VL	Limit speed
VS	Stall speed	VS	Stall speed

2.1.2. Transient Methods

As the characteristics of planes changed in terms of speed, size, and structural flexibility, accounting for flexibility and dynamic loads became a crucial factor in aircraft design. Since the publication of Amendment 14 of EASAs JAR25 (now CS25) in 1994 [22], dynamic gust analysis has been mandatory for the certification of large transport aircraft. The underlying differential equation is now integrated with respect to spatial and temporal discretization instead of sole quasi-steady peak accelerations, thus allowing for the inclusion of the combined flight dynamics with aeroelastic effects. With these changes, lag in the buildup of lift is accounted for as well as the coupling of the various modes of the aircraft. The certification specifications for large airplanes provided in CS25.341 assume that the plane is subjected to symmetrical vertical and lateral discrete gusts with a 1-cos shape during level flight. The 1-cosine gust profile serves as a simplified representation approximating the actual atmospheric turbulence, enabling easier calculations of transient events.
The shape of the gust velocity is constructed similarly to (2.8) as following:

$$U = \frac{U_{ds}}{2}(1 - \cos(\frac{2\pi s}{2H})) \qquad \textbf{(2.10)}$$

where U_{ds} denotes the design gust velocity. Here, s indicates the distance of the aircraft penetrated into the gust, and H denotes the gust gradient, representing the distance the aircraft penetrated into the gust until the gust reaches its peak velocity. The dynamic, unlike the quasi-steady response, is sensitive to different gust gradients, for which reason a so-called *tuning* of the gust is mandated. According to CS25 and MIL-F-8785C [87], the gust must be tuned to an adequate series of gust gradients H in the range of 9 to 107 meters. Each of these gradients must be analyzed for every load case in the envelope to determine the specific critical response. If 12.5 spatial chord lengths exceed 107m, then an appropriate extension is required. Regarding the number of individual gust gradients, it was found that 10-20 different gradient distances were enough to identify the gust gradient that leads to the peak loads [21].

The design gust velocity U_{ds} used in (2.10) is defined in CS.25.341 (a)(6) and given through

$$U_{ds} = U_{ref} F_g (H/107)^{1/6} \quad \textbf{(2.11)}$$

U_{ref} represents the reference gust velocities specified in CS25.341 (a)(5)(i). Figure 2.5 these reference gust velocities to those given in CS23.333 (c)(1) and MIL-A-8861B 3.5.1.1. The intensity of the gusts varies depending on the equivalent airspeed (EAS) and altitude. In case of the cruise speed VC, U_{ref} equals 17.03 m/s at sea level. Then, it decreases linearly to 13.41 m/s from sea level to 4572 meters, and further decreases to 6.36 m/s from 4572 to 15240 meters. At dive speed VD, U_{ref} is halved concerning the specified value for VC for probabilistic reasons.

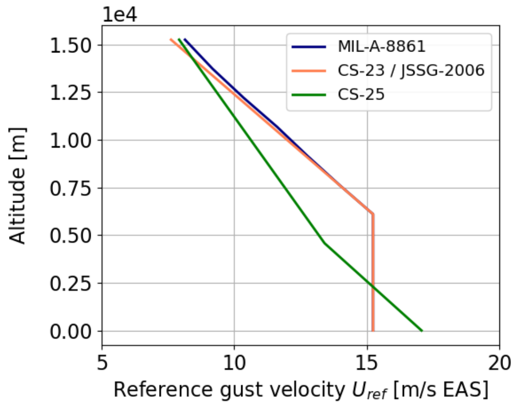

Figure 2.5: Comparison of reference gust velocities given in CS23, MIL-A-8861B and CS25

The reference gust velocity, assumed with a gradient distance of 107 meters, is defined as a single peak event occurring every 70.000 hours if the plane would fly 100 percent of its service life at the respective altitude. First, it is normalized by the gust gradient to account for the reduced reference velocity of gust with shorter gradients. Then, an alleviation factor F_g given in (2.12) is applied to account for the specific mission profiles of considered aircraft based on the anticipated service time it spends at each altitude. The flight profile alleviation factor is calculated as follows:

$$F_g = 0.5(F_{gz} + F_{gm}) \quad \textbf{(2.12)}$$

where

$$F_{gz} = 1 - \frac{Z_{mo}}{76200} \quad \textbf{(2.13)}$$

$$F_{gm} = \sqrt{R_2 \tan\left(\pi R_1 \frac{1}{4}\right)} \quad \textbf{(2.14)}$$

with

$$Z_{mo} = maximum\ operating\ altitude\ ,$$
$$R_1 = Maximum\ landing\ weight\ /\ Maximumtake\ off\ weight$$
$$R_2 = Maximum\ zero\ fuel\ weight\ /\ Maximumtake\ off\ weight$$

Figure 2.6 illustrates the gust profiles at sea level and a flight profile alleviation factor of $F_g = 1.0$, with the corresponding gust gradients and their peak velocities listed in Table 2.2.

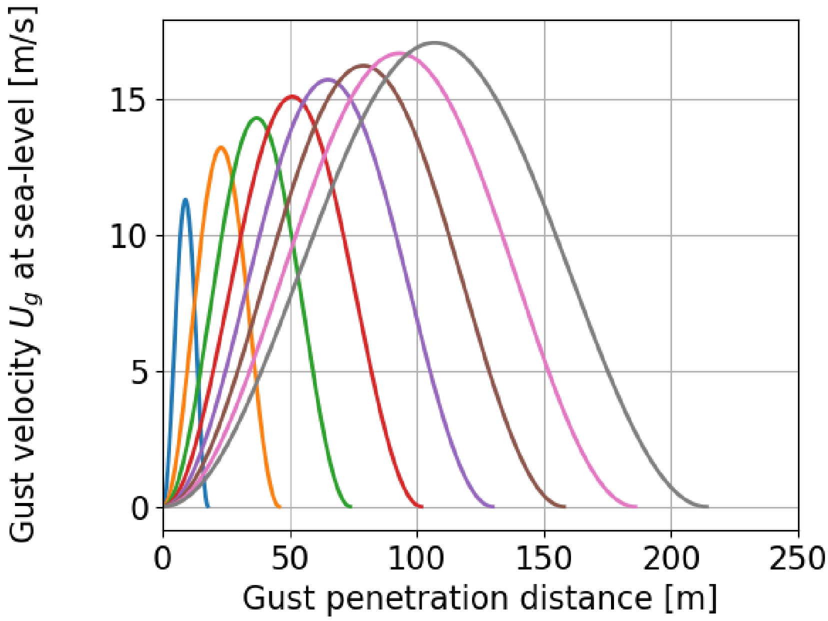

Figure 2.6: Gust appearance at sea-level and F_g=1.0 according to CS25

Table 2.2: Gust gradients and corresponding peak velocities depicted in Figure 2.6

Gust gradient	**9**	**23**	**37**	**51**	**65**	**79**	**93**	**107**
Peak velocity	11.3	13.2	14.3	15.1	15.7	16.2	16.7	17.03

A comparison of the various gust load certification methods described in section 2.1.1 and 2.1.2, and their distinctive features are collected in Table 2.3.

Table 2.3: Comparison of gust load certification requirements

Name of Document (Issuing Authority)	Applicability	Last Revision	Distinctive Features	Gust Gradients	Reference Gust Velocities at V_C EAS
CS-23 (EASA, 2003) / FAR-23 (FAA, 1965)	**Civil Aviation - Small and Utility Aircraft**	**2023 / 2023**		**H = 12.5 c**	**From 0 to 6096 meters:** **-> *15.24 m/s*** **From 6096 to 15240 meters:** **-> *Linear reduction from 15.24 m/s to 7.62 m/s*** 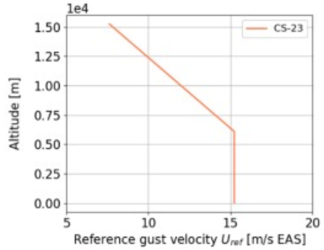
JSSG-2006 (US DoD, 1998) / MIL-STD-1797 (US DoD, 1990)	**Military Aviation - Entire US Military**	**2019 / 2006**		**H = 12.5 c / Various gradient lengths**	**From 0 to 6096 meters:** **-> *15.24 m/s*** **From 6096 to 15240 meters:** **-> *Linear reduction from 15.24 m/s to 7.62 m/s*** **Above 15240 meters:** **->** $\sqrt{\sigma_{altitude}}/\sqrt{\sigma_{15240m}}$ **with** $\sigma = \rho/\rho_0$ 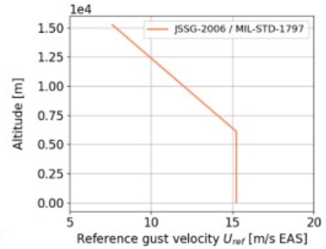
MIL-A-8861B (US DoD, 1986)	**Military Aviation - US Navy**	**2019**	**Requires superposition of gust loads with 0.6 * Nz (Design maximum limit load factor)**	**H = 12.5 c**	**From 0 to 6096 meters:** **-> *15.24 m/s*** **From 6096 to 15240 meters:** **->** $\sqrt{\sigma_{altitude}}/\sqrt{\sigma_{15240m}}$ **with** $\sigma = \rho/\rho_0$ 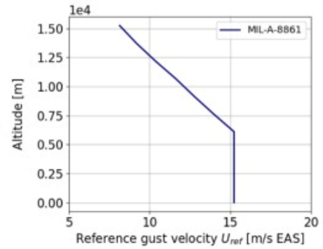
CS-25 (EASA, 2003) / FAR-25 (FAA, 1965)	**Civil Aviation - Large Transport Aircraft**	**2023 / 2023**	**Knockdown of reference gust velocities by Flight profile alleviation factor Fg**	**Sufficient number of gust gradients H in range of 9 – 107 meters**	**From 0 to 4572 meters:** **-> *Linear reduction from 17.07 m/s to 13.41 m/s*** **From 4572 to 15240 meters:** **-> *Linear reduction from 13.41 m/s to 7.92 m/s*** 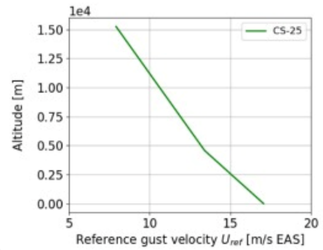

2.1.3. Continuous Turbulence Methods

Until the 1980s, turbulence loads were modeled as a sequence of discrete events [27]. Atmospheric turbulence was thought to be adequately represented by isolated discrete gusts of defined size and wavelength. In the past, this method was very effective when applied to aircraft that were relatively rigid and operated at low speeds. However, this approach is inadequate for accurately determining how today's flexible, high-speed aircraft respond to gusts as it neglects the interaction between dynamic responses and generalized aerodynamic forces [3].

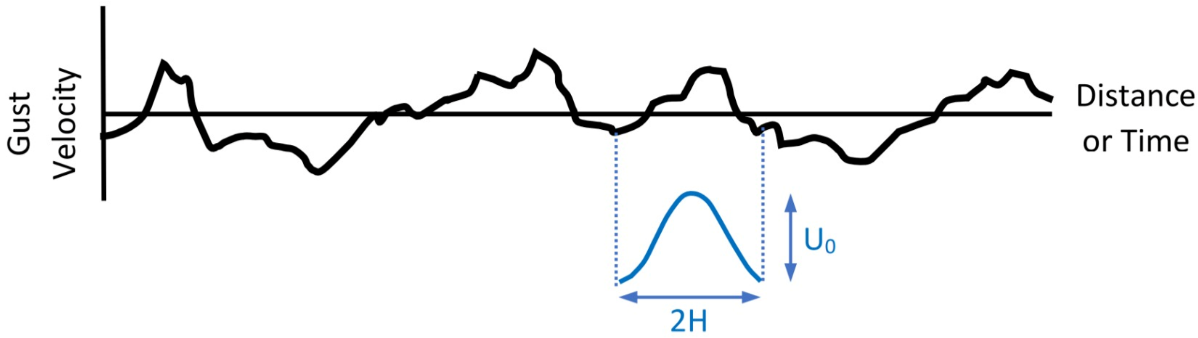

Figure 2.7: Depiction of turbulent air and derived approximation of a 1-cos gust

First introduced in 1955 by Press and Houbolt, power spectral methods gained ever more recognition in the gust load simulation field throughout the years [40]. Since gusts occur continuously when an aircraft is flying in turbulent air, the concepts of continuous atmospheric turbulence and power spectral density techniques were introduced to more accurately depict these probabilistic considerations [37]. In the context of continuous turbulence, it is assumed that atmospheric fluctuations occur in patches where the gust velocity and aircraft response exhibit continuous variations. It is not possible to establish a direct correlation between a specific response load and a particular velocity fluctuation. Consequently, turbulence loads can only be described within statistical terms [39].

Well-established methods like the continuous turbulence model by Karman or Dryden, as well as several other approaches for stochastic gust load models can be found with more detailed descriptions in the North Atlantic Treaty Organization Research and Technology Organization (NATO RTO) publication on design loads for future aircraft [75]. Although continuous turbulence is a part of the certification process in the civil aviation code CS25/FAR25 as well as the military code MIL-A-8861B, the investigation of continuous turbulence is beyond the scope of this work, as this work will focus solely on the discrete gust load analysis methods.

2.2. State-of-the-Art in Gust Load Analysis for Military Configurations

Compared to civil aviation, the literature and publications on gust load analysis for military aircraft are rather sparse. There are two main reasons for this: Research and development in the defense sector is crucial for national security and is often confidential. Moreover, according to the NATO RTO Task Group [75], combat aircraft structural design considerations are mainly dependent on maneuvering loads, rather than gust loads. As a result, gust loads are not considered as a critical factor and are of less interest, therefore most sizing of the full structure is accomplished through maneuver loads [96]. Consequently, JSSG-2006 states that discrete gust analysis is a sufficiently precise simulation method for aircraft in which maneuver loads are assumed to be the dimensioning factor. Supplemental continuous turbulence analysis may also be desirable for airplanes for which gust loads are anticipated to be a significant structural factor, especially if they have a low wing loading [84]. Despite these considerations, gust loads can be sizing for aircraft conducting high speed, low altitude flights [76].

Despite civil aviation being the primary focus of most publications, the NATO Advisory Group for Aerospace Research and Development (AGARD) and the NATO Research and Technology Organization (RTO) have recently published a large number of works on load requirements and gust load analysis [3,8,39,60,75]. These provide an insight into load analysis and preliminary design methodology in the defense sector. The publications are examined specifically for industry approaches in gust load simulation. Based on this, novel findings in the industry are discussed, gaps are identified and potential areas for investigation highlighted. The US Department of Defense (US DoD) also provides numerous of standards and reports [84,85,89,90] although few documents provide specific data and many specifications remain confidential [88]. Furthermore, many military aircraft certification requirements lag behind civil certification and are often outdated [15]. An example is the load certification requirements MIL-A-8861B used by the US Navy, where an old reference gust speed is still in use. As seen in Figure 2.4, the reference gust velocities in MIL-8861-A differ slightly from those provided in CS-23 and JSSG-2006. According to Tolefson [83], gust velocities remain essentially constant up to FL200, with only a 10% reduction occurring in the following 10,000 feet. Both military and civil certifications agree on this. However, the military specification differs in that it applies a density factor after FL200 to reduce gust velocities, instead of a linear reduction as described by CS23. This reduction method using a density factor can be attributed to the FAA's tentative airworthiness standards for supersonic transport aircraft from 1971 [28], which state that at the time of publication sufficient data was not available for supersonic flight to support a linear reduction of gust loads from 20,000 ft to 80,000 ft. As a result, it recommends the use of the density reduction factor instead of the straight-line reduction for supersonic flight. On the other hand, more contemporary certification standards like CS23, JSSG-2006 and MIL-STD-1797 allow for a linear reduction of reference gust velocities up until 50,000 feet, from where the same density reduction factor is employed due to a lack of data for supersonic flights. Although civilian certifications are more numerous and on par with latest research, they often do not meet the additional requirements necessary for military configurations' unique characteristics. This is especially true for supersonic aircraft which are mainly utilized by the military sector. In supersonic flight, limiting load factors need to be further reduced since high speeds decrease the available load margin [75]. In addition to gust loads alone, MIL-A-8861B 3.5.1.2 as well as JSSG-2006 3.4.1.6 require consideration of the superposition of various maneuver loads with a gust encounter for certain mission profiles, as design parameters may be reliant on such loads. For aircraft capable of low altitude attack missions, MIL-A-8861B requires the following consideration: The aircraft is assumed to encounter a 7.62 m/s vertical gust in addition to the highest load factor experienced while executing one of the following specified maneuvers:

I. The load factor for low altitude bombing systems (LABS), toss, or other programmed bombing systems.
II. 0.6 times the design maximum symmetrical flight limit load factor.
III. Maneuver with a load factor of 2.25.

The limit load factor for turbulent air of 0.6 times the limit load factor, also found in the US Navy's advisory commission handbook for fighter pilots [56], is derived by the assumption that moderate turbulent air can induce an incremental load factor that is cumulative with pilot induced loading. So, while the factor of 0.6 itself is rather arbitrary, this limitation thus averts exceedance of structural limits. Prior to 1980, dynamic load requirements depended more on problem-solving addressing known phenomena, than actual load prediction [15]. This is reflected in the military standards, which till this day only require quasi-steady simulation methods for deterministic gust load approaches. This underlines that military certification methods are often outdated [15], so it is common practice in the defense industry to use more recent civil certification methods such as dynamic simulation of gust loads. This trend stems from various reasons rooted in the derivation of the Pratt formula that adversely affect its accuracy. The alleviation factor K_g, which predicts the peak acceleration relative to the reference aircraft B-247, is estimated using empirical data from the 1940s. This prediction assumes that the pitching motion of the considered aircraft is influenced by accelerations in a similar way to the reference aircraft. Therefore, the method is most precise when restricted to aircraft with similar characteristics as those used in the derivation of the Pratt formula [12,39]. Furthermore, the EOM in the Pratt formula assumes subsonic flows and neglects compressibility effects and shock waves [65]. At supersonic speeds, aerodynamic characteristics, including the lag in lift buildup and flow fields, differ significantly [47]. For accurate results, nonlinearities associated with supersonic flight must be taken into consideration. Therefore, not all assumptions used in the derivation of the Pratt method can be transferred to modern supersonic fighter jets. As noted by Chapman [15], the assumed gust gradient length of 12.5 spatial chords in the Pratt may not always produce the highest loads on military configurations. Some argue that gusts are highly irregular events and that a physically consistent description, rather than sole empirical data, should form the basis of gust definition, necessitating the tuning of gust gradients [59]. In addition, Handojo and Klimmek [36] demonstrated that quasi-static analysis with the Pratt method may not accurately predict the root wing torsion moment when compared to dynamic simulations. It is still noteworthy that, although not suitable for precise load calculations, quasi-static methods require little computational power and time compared to other gust load methods, which makes them a cost-effective method used in the preliminary design to explore large design spaces as shown by Blair et. al. [9] and Rasmussen et. al. [69].

This trend of using dynamic simulation is visible in several publications for loads analysis on military configurations. As described by Luber et al. [51], dynamic load simulations on the Eurofighter are performed with MSC Nastran using panel methods such as the DLM with subsonic/supersonic correction codes. Chapman [15] used the DLM at Airbus DS to predict loads on the supersonic Eurofighter [8], and Pototzky [63] presented Nastran DLM models used by Lockheed to simulate gust loads on the F35. To the authors best knowledge, no publication demonstrates gust load simulations in the supersonic regime by means of supersonic panel methods such as ZONA51. However, despite the use of dynamic simulation techniques, accurately predicting gust loads remains a challenge, as panel methods such as the VLM/DLM often don't have the necessary fidelity to accurately determine gust loads [15]. Nevertheless, solution tools based on panel methods like the state-of-the-art MSC Nastran provide satisfactory results. Unsteady computational fluid dynamics (CFD) can enhance the accuracy of these methods, especially for trans- and supersonic effects, which cannot be accurately depicted by subsonic panel methods like the DLM. Here, the subsonic solutions can be corrected by supersonic codes based on linearized CFD solutions [49,68,82]. At the same time, CFD remains a mostly academic application as it is still computationally expensive and therefore unsuitable for industrial applications in a preliminary design phase.

Although simulation methods for civil aircraft certification are frequently used in the military industry, it should be noted that the civil requirements often include underlying assumptions not valid for the certification of military aircraft, for which they can inadvertently reduce gust loads on highly maneuverable supersonic aircraft [15] (AGARD-815, P.106). Luber et al. [51] highlighted that the maximum accelerations due to gust loads are highly dependent on the aircraft's geometry, and thus gust gradients should be tuned within the range of 5-25 chord lengths. As stated by Chapman [15], short gust gradients seem to align with the first wing bending mode of highly maneuverable, supersonic combat aircraft, resulting in high loads due to gust impact. In this case, high wing loading during gust encounters is not observed at the wing root, but rather at the wing outboard monitoring stations. This may lead to gust loads only sizing certain parts of the wing. This finding is congruent with the research of Rumpfkeil and Beran [76], which stated that gust loads can lead to sizing of outer wings, pylons, and other thin parts for fighter aircraft. Becker [8] validated this hypothesis further by stating that gusts tuned to short gradients beneath 18 m can lead to high excitations and accelerations of the wingtip for fighter aircraft. Therefore, he recommended that military aircraft with external storage on outboard wing stations should consider discrete gust analysis as an essential factor. On the other hand, as Williams and Page [101] point out, high wing loading alleviates gust response. Therefore, lower wing loading evokes a high gust response during gust encounters for low-altitude, high-speed flights and thus sets the lower limit for wing loading.

Particular attention should be paid to supersonic combat aircraft, as they have different operating points than civil aircraft. Pratt [64] conducted simulations on supersonic civil transport configurations, revealing that subsonic flight poses the highest gust loads, with supersonic aircraft being relatively less sensitive to gusts compared to subsonic aircraft. This could be attributed to supersonic transport aircraft cruising at higher altitudes with lower gust intensities, but the same may not be applicable for supersonic fighter aircraft that fly at supersonic speeds at lower altitudes with high gust intensities.

2.3. Deflection Rate Limits

Modern combat aircraft operate in dynamic environments and are required to perform high agility maneuvers throughout the envelope. To achieve this, many modern military aircraft are intentionally designed to be unstable. As a result, quick control surface deflections are required to maintain maneuverability, alleviate load, and station keeping [7,31].

Deflection rate limits can vary significantly across publications and real-life applications. Rate limits are frequently selected rather optimistically, therfore may not reflect actual limits in practice. Evaluating the impact of higher deflection rates on flight performance is crucial for appropriately sizing the actuator system and balancing related performance deficiencies. Achieving balance in size, weight, and output performance is important while ensuring compliance with the flight envelope and certification standards. The next section will explore the constraints that impact the control surface deflection rate, along with available publications on the topic.

When selecting a deflection rate limit, the following characteristics need to be considered:

I. The flight envelope.
II. Available installation space and weight found from the preliminary aircraft design.
III. The minimum required actuator output performance to satisfy certification.
IV. The possibility of pilot-induced oscillations (PIO).

Transport aircraft have a less demanding flight envelope that allows for lower deflection rates compared to combat aircraft, which require high deflection rates due to their mission profiles [31]. Combat aircraft, which often fly at supersonic speeds, require more powerful actuators to achieve necessary deflection angles as high airspeeds induce larger hinge moments. This phenomenon mainly affects the downward deflection limiting the actuator's movement, whereas the upward deflection experiences minimal hinge moment induced by higher airspeeds and is therefore not limited [27]. New control surfaces with differential deflection rate limits enable accurate trim of ailerons and flaperons regardless of airspeed [72].

During preliminary aircraft design, initial specifications limit the selection of control surface actuators according to their dimensions, weight, and deflection rates to ensure ideal weight and structural integrity. On the other hand, maneuver specifications establish a minimum level for both deflection and rate limits of the control, thus deriving basic functionality and design requirements [1]. Regulatory requirements, such as CS-25 [26], MIL-A-8661B [85] and MIL-STD-1797A [89], mandate certain maneuvers that set minimum deflection rate limits. As Kaminski [42] demonstrated for modern fighter aircraft, NATO best practices [55] specify a minimum deflection rate so that full elevator surface deflection from neutral is achieved in 0.2 seconds. The representative rate limit for this maneuver is approximately 125 degrees/s. Gern et al. [30] stated that deflection limits of 90 degrees/s are the State-of-the-art for high performance fighter aircraft, whereas transport aircraft already reach a satisfactory level of actuator rate at a limit of about 30-40 degrees/s [34]. Efforts to enhance actuator performance, while simultaneously maintaining compactness and light weight, have initiated a shift from hydraulic toward electric actuators. Electric systems offer compactness and weight reduction, with potential weight savings of up to 500 Kg on civil transport aircraft as Aigner et al. [1] demonstrated on an Airbus A320 configuration. Novel configurations started implementing these kinds of actuators, but they still lack the capabilities to fully replace hydraulic actuators, especially for military combat aircraft [13,16]. At the same time, electric actuators are tested on different configurations such as the C-141 star lifter, the F-18 [41] and the Airbus A380 [91].

Innovation in control systems and fly-by-wire technology facilitates the attainment of greater deflection rates. Albeit high deflection rates are desirable, limiting these high deflection rates, notably during vital stages like takeoff and landing, is critical for maintaining pilot control. This is because excessively high rates could result in unintended maneuvers that pilots are unable to stabilize. However, imposing-rate restrictions causes time lag effects, which necessitate careful calibration to prevent surface deflections from trailing behind the pilot's input. Otherwise, this could result in Pilot-Induced Oscillation (PIO). Limited deflection rates can cause corrective inputs in the opposing direction, resulting in a sinusoidal feedback loop that increases the risk of crashes through PIO. Pilots reported that problematic rate limiting occurs if deflection rates are limited to about $\dot{\eta} \approx 10 - 20\ °/s$ [32]. Duda [19] has outlined the requirements to avoid such PIO scenarios. For more information on PIO and accident analysis, the reports by the National Research Council of the United States [54] can be consulted.

A wider range of deflection rate limits for various control surfaces and aircraft configurations can be extracted from Table 2.4.

Table 2.4: Deflection rate limits for various control surfaces and aircraft configurations

Model Name	Configuration Type	Control Surface	Rate Limit	Actuator Type
Boeing C-17 [54]	Military Transporter	Aileron	37 degrees/s	Hydraulic
Airbus A320 [54]	Airliner	Aileron	35-40 degrees/s	Hydraulic
NASA SCAT-15F [33]	Supersonic Airliner	Aileron	70 degrees/s	Hydraulic
General Dynamics F-16 [58]	Fighter Jet	Aileron	80 degrees/s	Hydraulic
Grumman X-29 [7]	Experimental Aircraft	Canard	120 degrees/s	Hydraulic
General Dynamics F-16 [4]	Fighter Jet	Canard	100 degrees/s	Hydraulic
Boeing 777 [54]	Airliner	Elevator	40 degrees/s	Hydraulic
North American X-15 [80]	Experimental Aircraft	Elevator	26 degrees/s	Hydraulic
General Dynamics F-16 [4]	Fighter Jet	Elevator	60 degrees/s	Hydraulic
General Dynamics F-16 [78]	Fighter Jet	Flaperon	56 degrees/s	Hydraulic
General Dynamics F-111 [79]	Fighter Jet	Flaperon	40 degrees/s	Hydraulic
NASA SCAT-15F [33]	Supersonic Airliner	Flaperon	40 degrees/s	Hydraulic
Airbus A320 [103]	Airliner	Flaps	2 degrees/s	Hydraulic/Electric
Airbus A320(modified) [92]	Airliner	Flaps	1.4 degrees/s	Hydraulic/Electric
NASA SCAT-15F [33]	Supersonic Airliner	Flaps	10 degrees/s	Hydraulic
Grumman X-29 [7]	Experimental Aircraft	Flaps	35 degrees/s	Hydraulic
Lockheed Martin F-22 [54]	Fighter Jet	Horizontal Tale	60 degrees/s	Hydraulic
General Dynamics F-16 [4]	Fighter Jet	Rudder	120 degrees/s	Hydraulic
NASA SCAT-15F [33]	Supersonic Airliner	Rudder	50 degrees/s	Hydraulic
General Dynamics F-16 [24]	Fighter Jet	Speed Brakes	120 degrees/s	Hydraulic
Grumman X-29 [7]	Experimental Aircraft	Strake	35 degrees/s	Hydraulic
Lockheed Martin F-22 [54]	Fighter Jet	Thrust Nozzles	40 degrees/s	Hydraulic

2.4. Objectives and Scientific Contribution

Despite a significant number of literature available on gust loads for civil aircraft, the literature review yielded few studies on gust loads at supersonic speeds or specific to military fighter aircraft. To close this gap, the presented work has the following objectives.

To the author's best knowledge, no publication offers a comprehensive range of relevant parameters for the operating points of a combat aircraft. Due to the confidential nature of military projects, most results cannot be replicated due to undisclosed underlying assumptions and resulting quantities. At the same time, it is important to select the right assumption for the specific requirements of combat aircraft, as for example assumptions made in the civil certification requirements may unintentionally alleviate gust loads and should thus be used with care. Military certification often lags behind with respect to the applied methodology, causing the industry to adopt more rational approaches. Still, publications do not provide details about the precise methods or parameters used in these industry standards.

> **1.** Select the necessary gust load assumptions and operating envelope based on the literature review conducted in 2.2 and 2.3.

Most combat airplanes require high agility and are therefore designed to be intentionally unstable. The FFD follows a similar principle. In real-world applications, selecting the proper actuator for control surfaces often requires weighting in the advantages and disadvantages. Based on this, deflection rates in other publications are often selected optimistically high, which makes the results questionable regarding feasibility for real applications.

> **2.** Design a basic rate-limited longitudinal control system that will allow for feasible gust load computations.

The military certification only provides a coarse set of guidelines for the calculation of gust loads. To get a good overview of gust loads, a comprehensive gust load analysis that covers the whole flight envelope is necessary.

> **3.** Conduct a comprehensive gust load campaign covering the whole flight envelope and analyze the characteristics of the resulting loads.

Up to this point, all literature reviewed has utilized subsonic panel methods such as the DLM, correcting transonic and supersonic effects through solutions from linearized CFD computations or empirical data. The viability and application of supersonic panel methods, notably ZONA51, have not yet been published and it remains ambiguous whether these methods are adequate for simulating gust loads on aircraft configurations like the FFD.

> **4.** Conduct gust load simulation in the supersonic regime and compare the results to the subsonic load. Assess the plausibility of the resulting gust loads using supersonic panel methods.

Multiple publications have shown that utilizing quasi-static gust methods to estimate loads on combat aircraft is insufficient, especially for supersonic flight and the unique geometric features of these aircraft. In order to evaluate the feasibility of quasi-steady methods for gust calculations on supersonic combat aircraft, they must be compared with more rational approaches like the transient gust load methods to assess whether they are more conservative. Furthermore, both gust loads need to be compared to the maneuver load envelope to determine whether gust loads can be a sizing factor for the general structure.

5. Compare the dynamic gust loads to quasi-steady and maneuver loads.

The Literature review indicates that small gust gradients may cause high excitations on the wingtips of combat aircraft. This phenomenon is likely due to the alignment of these gusts with the wing bending mode. Thus, gusts could potentially affect outboard payload and payload attachments. However, publications on this topic did not provide specific ranges for the accelerations and gust gradients in question.

The US Navy limits pilot-induced maneuver loads to two-thirds of the maximum load factor in turbulent air. However, the rationale behind this limit appears arbitrary, lacking specific justification. As a result, it remains to be determined whether the reduction in the maximum attainable load factor is too conservative or needs an upward adjustment.

6. Investigate the accelerations on different parts of the aircraft.

3. Applied Methodology on the Future Fighter Demonstrator

In the following subsections, the theoretical background necessary for gust load analysis will be presented. The methodology and technical execution will be shown at the example of the DLR Future Fighter Demonstrator (FFD), presented in [96,97]. The following methods described are implemented in the LoadKernel Software [94,95], a DLR in-house tool which allows for the calculation of quasi-steady and unsteady loads.

3.1. Characteristics of the Configuration

The reference aircraft utilized in this work is based on an in-house DLR research project, developing a conceptual design for a future fighter aircraft. The DLR FFD is a highly agile, twin-engine two-seater double delta wing configuration with an approximate maximum takeoff mass at 30.0 to 36.0 tons. The conceptual configuration was designed to meet the top-level aircraft requirements (TLAR) set in the project specifications [96]. The configuration is designed to be deployed within various mission profiles, amongst others Combat Air Patrol (CAP), Supersonic Intercept (OCA), Close Air Support (CAS) and Suppression of Enemy Air Defense (SEAD). More detailed description of mission profiles can be extracted from MIL-STD-3013B [90]. An overview of the aircraft parameters is given in Table 3.1.

Table 3.1: Overview of the DLR Future Fighter Demonstrator (FFD) Key Design Parameters, reproduced from [97]

Property	**Number**
Maximum speed	VC = Ma 2.0 at 36,000 - 50,000 ft VD = Ma 2.3 at 36,000 - 50,000 ft
Maximum Altitude	50,000 ft (Combat ceiling)
Mission radius	550 - 700 NM
Mass	30.0 – 36.0 t maximum take-off mass (MTOM)
Payload	Air 2 air mission: 1820 kg (internal) Optional: 8000 kg (internal + external)
Agility	Load factor Nz = -3.0 … +9.0 with basic flight design mass (BFDM)
Longitudinal Stability	Subsonic: unstable; Supersonic: stable
Control surfaces	Ailerons along the main wing trailing edge (roll) All-movable horizontal tail planes (pitch) Vertical tail planes with rudder (yaw)

3.2. Steady and Unsteady Aerodynamics

As mentioned in the introduction, this work focuses on gust load analysis in the subsonic and supersonic regimes using aerodynamic panel methods. The Vortex-Lattice-Method (VLM) for steady flow, and the potential-theory based Doublet-Lattice-Method (DLM) for unsteady flow are commonly used for transient sub and transonic gust analysis. However, these methods are not suitable for non-linear aerodynamics in transonic and supersonic regimes [76], as the DLM does not encompass phenomena such as compression shocks. Hence, for gust load simulation in the supersonic regime, the supersonic panel method ZONA51 will be utilized. A brief overview of both the DLM and ZONA51 will be presented below.

A more comprehensive description of general panel methods and the derivation of the DLM is given by Katz and Plotkin [43], and a list of panel methods specifically for industry applications is presented by Erickson [25]. A quick overview of the VLM and the DLM, along with their implementation in the LoadsKernel is available from Voß [93]. For a more detailed breakdown of ZONA51, consult the MSC. Nastran aeroelastic user guide [52] or the ZAERO user guide [104]. The DLM is based on the linearized aerodynamic potential theory and belongs to the fast numerical methods of transient aerodynamics, first implemented by Albano and Rodden [2]. In the DLM, the lift surfaces are assumed to be flat plates divided into small, trapezoidal lifting elements whose lateral edges are parallel to the free incident flow. An illustration can be found in Figure 3.1. To model the unknown lifting pressure difference Δc_p, a doublet of constant distribution across the one-quarter chord line is assumed at each lift element. There is one control point per box, centered spanwise on the three-quarter chord line, satisfying the boundary condition of the surface normal downwash w at each of these points.

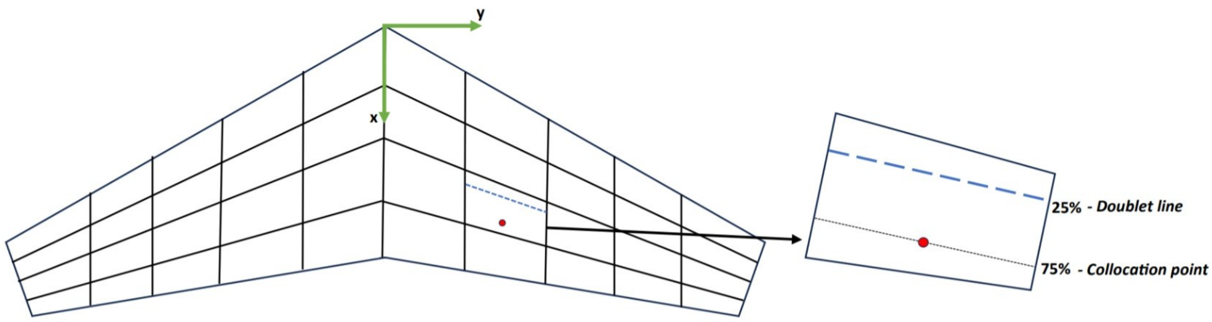

Figure 3.1: Discretization of a lifting surface using the DLM

The ZONA51 supersonic lifting theory is based on the Harmonic Gradient Method (HGM) of Chen and Liu [17,48], which, like the DLM, accounts for interference among lifting surfaces using an acceleration potential method. ZONA51 assumes uniform and either steady or harmonic oscillation. To model the unknown lifting pressure difference Δc_p, a potential vortex of constant distribution is assumed at each lift element. There is one control point per box, centered spanwise on the 95% chord line of the box, satisfying the boundary condition of the surface normal downwash w at each of these points. The ZONA51 method only allows for panels to induce influence on other panels within its Mach cone. The resulting aerodynamic mesh used in this work including camber and twist can be seen in Figure 3.2.

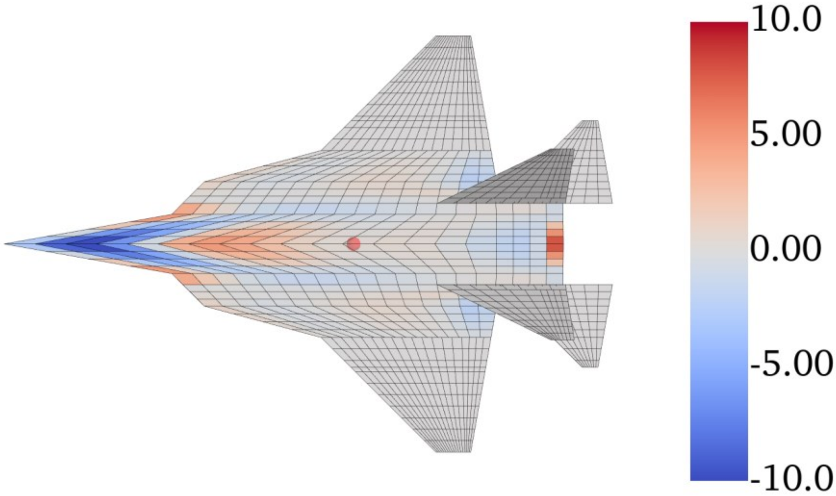

Figure 3.2: Aerodynamic mesh for DLM & ZONA51 including correction for camber and twist (indicated by color)

Both the DLM and ZONA51 are based on a matrix of Aerodynamic Influence Coefficients (AIC), which correlates the induced downwash velocity w to a complex pressure coefficient Δc_p. The AIC matrix is dependent on the Mach number and the reduced frequency k given as

$$k = \frac{2\pi f * c_{ref}}{2 * V_{TAS}} \tag{3.1}$$

The AIC matrix is then defined by

$$\Delta c_p = AIC\{Ma, k\} * w \tag{3.2}$$

With $k = 0$ for the quasi-static case, the solution of the DLM is equivalent to the VLM [73]. To consider the aerodynamic effects due to the twist and camber of the wing, a correction factor for the downwash is implemented through the W2GJ matrix. For further information on the characteristics of AIC matrices, consult the MSC Nastran aeroelastic user guide [52].

Since the aerodynamic forces can only be calculated for harmonic motions, they are known in the frequency domain. To conduct investigations in the time domain, either an inverse Fourier transform must be performed [73], or the aerodynamic forces must be obtained through a different approximation method. This work will incorporate the Rational Function Approximation (RFA) suggested by Roger [74] to obtain unsteady aerodynamic forces in the time domain and thus avoid the need for an inverse Fourier transform. Within the RFA, the AIC is approximated for each reduced frequency k by

$$AIC(k) = A_0 + A_1 * ik + A_2 * (ik)^2 + \sum_{n=1}^{n_{poles}} A_{n+2} * \frac{ik}{ik + \beta_n} \tag{3.3}$$

An implementation of the RFA for unsteady gust simulation is performed and further elaborated by Voß [94].

3.3. Structural and Mass Model

Calculation of the aerodynamic force acting on the aircraft during a gust encounter requires a Finite Element (FE) model, which is generated within the DLR-inhouse MONA process [45]. In the MONA process, a model is constructed through Modgen, another DLR-inhouse tool [46], with initial structural sizing of the FE model being performed using analytic-empirical methods. The structural model presented in Figure 3.3 aims to accurately represent the general structural dynamic features crucial for aeroelastic analyses. All main structural elements, such as spars, ribs, and upper and lower skins, are modeled using shell elements. Spar caps, stiffeners, and stringers are also installed by means of beam elements to prevent local buckling and provide greater structural realism. The wing includes three main spars and numerous flow-oriented ribs for a structural layout. Air intakes and the cockpit are not accounted for in the structural model. This detailed structural model will enable the calculations of frequencies and mode shapes necessary for accurate aeroelastic analysis. The MSC. Nastran FE model comprises 25,000 degrees of freedom (DoF), along with 4,292 grid points, 4,754 shell elements, and 4,096 beam elements.

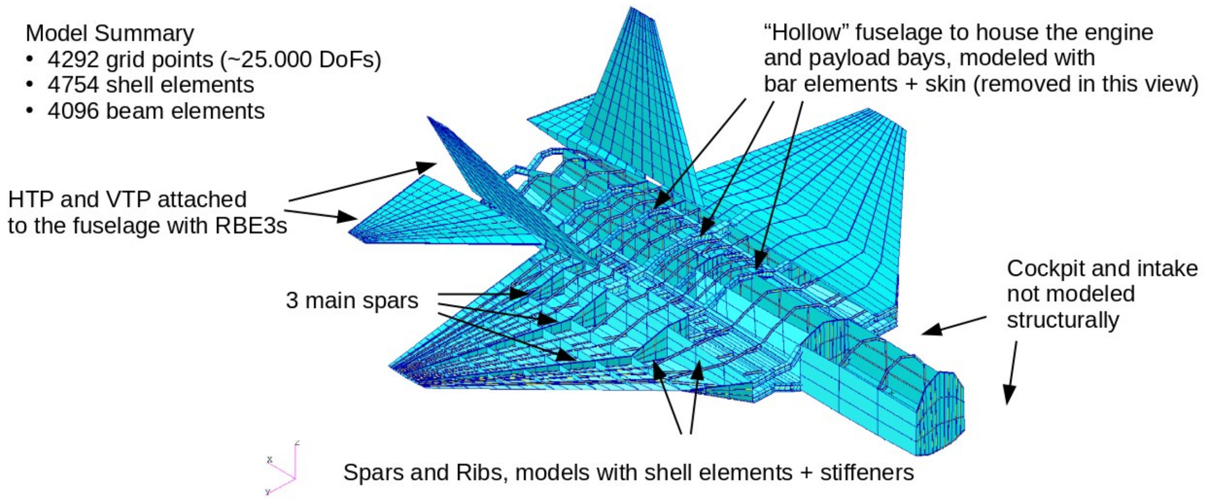

Figure 3.3: Structural model of the DLR Future Fighter Demonstrator, extracted from [76]

To accurately simulate the loads on an aircraft, it is essential to have comprehensive and accurately distributed mass cases, as both factors significantly affect the resulting loads. The masses comprise of structural masses, system masses, fuel masses, and payload masses. Different combinations of fuel and payload distributions are considered using four different mass configurations M1- M4. The fuel is modeled with volume elements, and then both mass and inertia properties are calculated by MSC. Nastran. The full FE and mass models are utilized for the loads analysis, however they are reduced onto subsection corner points by means of a Guyan reduction as described by Voß [94] to reduce computational effort. For a more complete listing of the mass cases and included characteristics, refer to Voss and Klimmek's description of the FFD [96]. The four mass cases as well as the underlying characteristics are summarized in Figure 3.4 and Table 3.2 respectively.

Table 3.2: Overview of mass configurations

Mass Case	Fuel	Payload	Mass	CG (x-direction)
M1 (MTOM)	100%	Yes	26.2 t	4.87 m
M2 (BFDM)	70%	Yes	23.2 t	4.83 m
M3 (BFDM)	70%	No	21.4 t	4.94 m
M4 (OEM)	0%	No	14.5 t	4.91 m

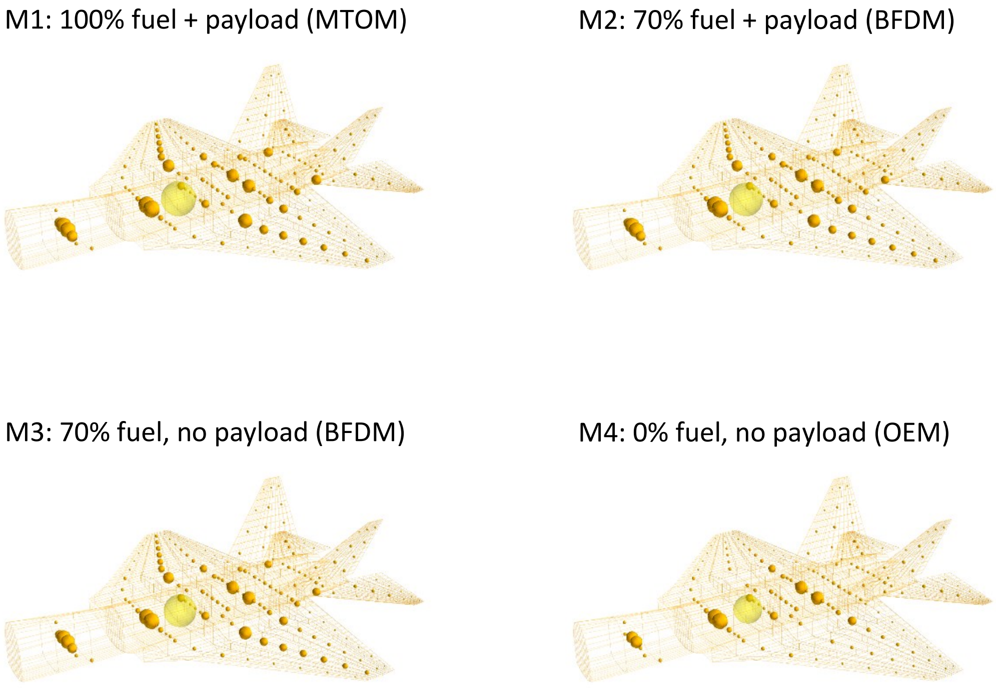

Figure 3.4: Mass configurations M1-M4 of the FFD

3.4. Modal Analysis and Equations of Motion

In a finite element (FE) model, each node comprises six degrees of freedom (DoF): translation in the x, y, and z directions, and rotation about the x, y, and z axes. For easier calculation procedures and management of the matrices, MSC Nastran divides these DoF into several distinct sets containing specific parts of this data. More details on the partitioning procedure for the sets can be found in [52].
A modal analysis of the structure is then performed based on aforementioned sets. The modal analysis extracts the eigenvalues and eigenvectors which describe the dynamic behavior of an elastic, oscillating system. These extracted parameters can then be interpreted within more physical aspects, such as the natural frequency of the system, its mode shapes and the modal damping. The undamped, unexcited structure is characterized through

$$M * \ddot{x} + K * x = 0 \tag{3.4}$$

with the mass M and the stiffness K. Rewriting the matrix in the frequency domain

$$\omega^2 * M * \hat{x} + K * \hat{x} = 0 \tag{3.5}$$

the formula can be rearranged into the general eigenvalue problem

$$-K * \hat{x} = \omega^2 * M * \hat{x} \rightarrow A * \Phi = \lambda * B * \Phi \tag{3.6}$$

With $\lambda = \omega^2$ characterizing the angular frequency of the modes. The corresponding eigenvector Φ projects the deflection in physical coordinates. When dealing with large matrices, as those commonly encountered in structural dynamics, one must solve the system iteratively for the first eigenvalues n_f utilizing the matrix of generalized eigenvectors Φ and generalized eigenvalues λ of A and B [94].
Omitting the rigid body modes, which are characterized by $\lambda = 0.0$, the first ten eigenmodes of the mass configuration M2 are presented in Figure 3.5 to Figure 3.14. The initial elastic eigenmode displays a frequency of $f \approx 7\ Hz$, indicating a stiff structure, while the tenth mode reaches a frequency of $f \approx 21\ Hz$. The 1st symmetrical wing bending mode depicted in Figure 3.8 appears at a frequency of $f \approx 9\ Hz$. Previous publications by Luber et. al. [51] show a comparable range for the eigenmodes of supersonic fighter aircraft, which supports the plausibility of this model.

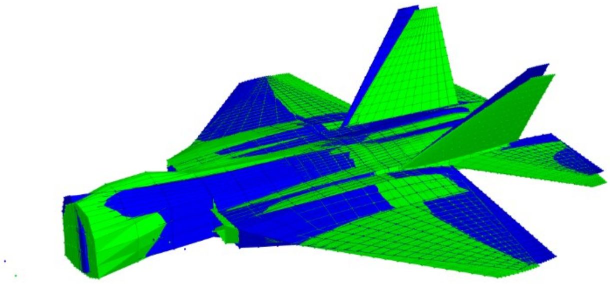

Lateral fuselage bending, 6.7 Hz

Figure 3.5: DLR FFD M2, Mode 1

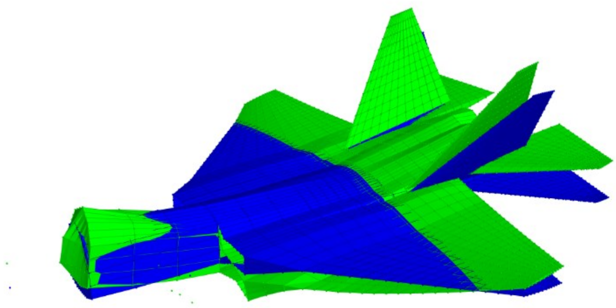

Longitudinal fuselage bending, 7.2 Hz

Figure 3.6: DLR FFD M2, Mode 2

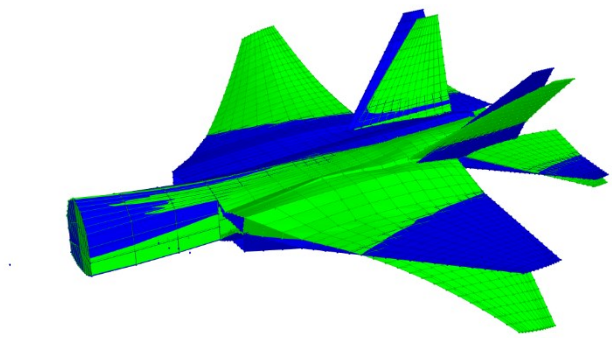

Asymmetric wing bending, 8.3 Hz

Figure 3.7: DLR FFD M2, Mode 3

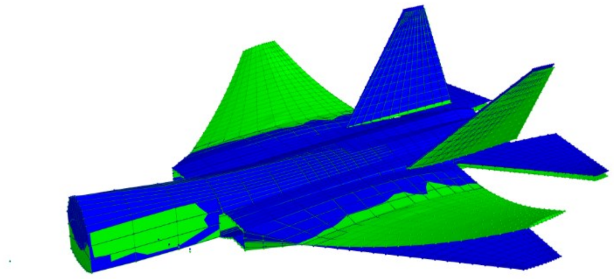

Symmetric wing bending, 9.0 Hz

Figure 3.8: DLR FFD M2, Mode 4

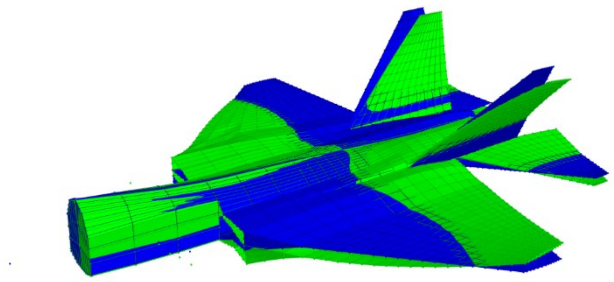

Assymetric wing torsion, 12.0 Hz

Figure 3.9: DLR FFD M2, Mode 5

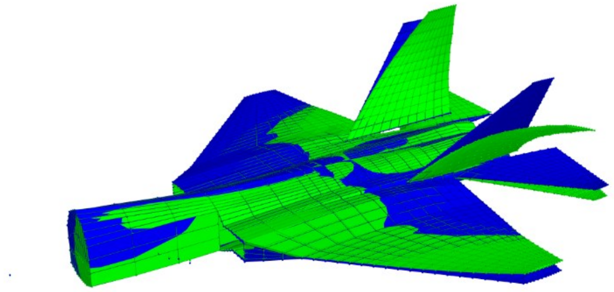

Tail rock + asymmetric wing bending, 14.5 Hz

Figure 3.10: DLR FFD M2, Mode 6

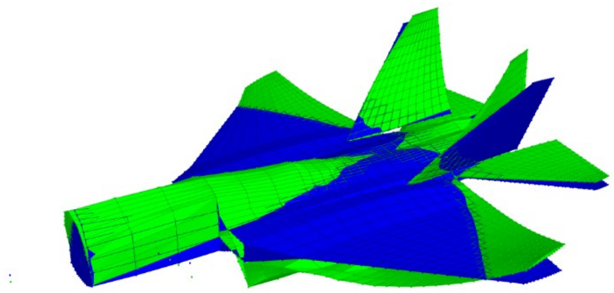

Symmetric wing torsion, 14.6 Hz

Figure 3.11: DLR FFD M2, Mode 7

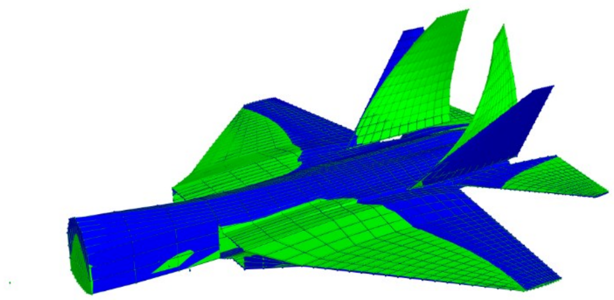

Vertical tail plane bending, 15.7 Hz

Figure 3.12: DLR FFD M2, Mode 8

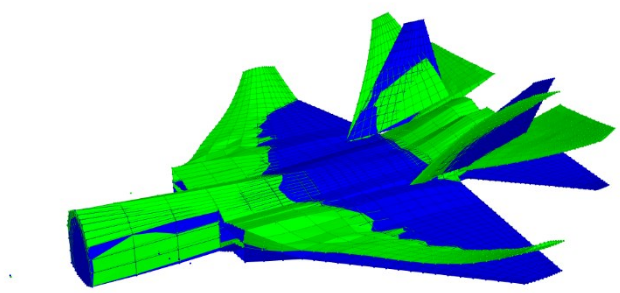

Rear fuselage bending, 19.9 Hz

Figure 3.13: DLR FFD M2, Mode 9

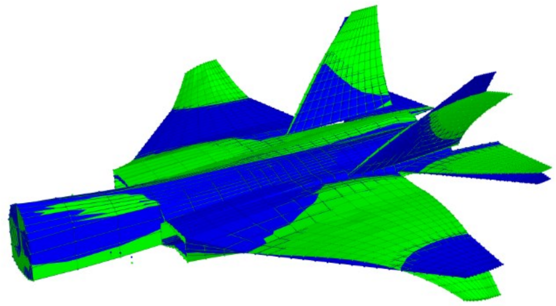

Assymetric wing bending + fuselage bending, 20.9 Hz

Figure 3.14: DLR FFD M2, Mode 10

The underlying Equations of Motion (EOM) can be categorized into rigid body motions and flexible body motions. The reference model assumes a rigid body with a constant mass M_b and a constant moment of inertia I_b placed at the CG of the model. These nonlinear EOMs are provided by

$$\dot{v}_b = M_b^{-1} * p_b^{ext,forces} + v_b \times \omega_b + \dot{v}_b^{grav} \tag{3.7}$$

and

$$\dot{\omega}_b = I_b^{-1} * (p_b^{ext,forces} - \omega_b \times (I_b + \omega_b)) \tag{3.8}$$

The terms denoted by the subscript b are the translational and angular velocities of the model with respect to the body frame of reference. The external loads $p_b^{ext,forces}$ acting on the aircraft are imposed on the mass and inertial matrices. Several terms included in the EOM are derived from the publications by Waszak, Buttrill, and Schmidt [11,99,100] and incorporated into the LoadsKernel software [94]. The effect of the external loads on linear flexible dynamics are considered through

$$M_{ff} * \ddot{u}_f + D_{ff}\dot{u}_f + K_{ff}u_f = p_f^{ext} \tag{3.9}$$

The matrices M_{ff}, D_{ff} and K_{ff} refer to the generalized mass, damping and stiffness matrices derived from the modal analysis, which is further explained by Voß [94].

3.5. Dynamic Gust Simulation and Trim Conditions

To perform the dynamic gust simulation, the aircraft is initially trimmed to a predefined state to set the aerodynamic forces on the control surfaces and maintain the desired attitude before the gust impact. For example, this state could be a horizontal level flight. The trim condition is to be defined in a way that the airplane is neither over nor under determined as otherwise, no unique solution can be calculated. Once the aircraft has been trimmed, a time simulation is initiated with the trimmed aircraft serving as the initial condition. During the simulation, the equations of motion (EOM) described in Section 3.4 are integrated over the specified time period. The gust impact is introduced as a set of acting loads, and the resulting deflection of control surfaces is modeled as enforced motions also treated as applied loads. This simulation method incorporates both the structural dynamics as well as the unsteady aerodynamic response. As rapid state changes result in the need for small time steps to accurately capture imposed loads, a large amount of data is generated. Consequently, only snapshots of the peak loads at specified larger time steps are taken into account, as a full output would contain an excessive amount of data. The snapshots are selected by identifying the minimum and maximum values of the 1-cos gust at each monitoring station for the respective quantity of interest [35]. The resulting loads on the structure are calculated using the Force Summation Method (FSM), which involves the addition of the physical coordinates with inertia and external forces. This method is only viable if the RFA, as elaborated in Section 3.2, is executed using physical coordinates [94]. Analyzing the forces acting on each individual node would be impractical. Therefore, the aircraft is subdivided into larger segments, which provide section loads. Each of these sections is selected based on the specified target of this work, including the investigation of loads acting on the wing root and wing tip. These section loads are extracted by integration of the nodal loads over the relevant area. Figure 3.15 visualizes the location of and the section under consideration for the monitoring stations.

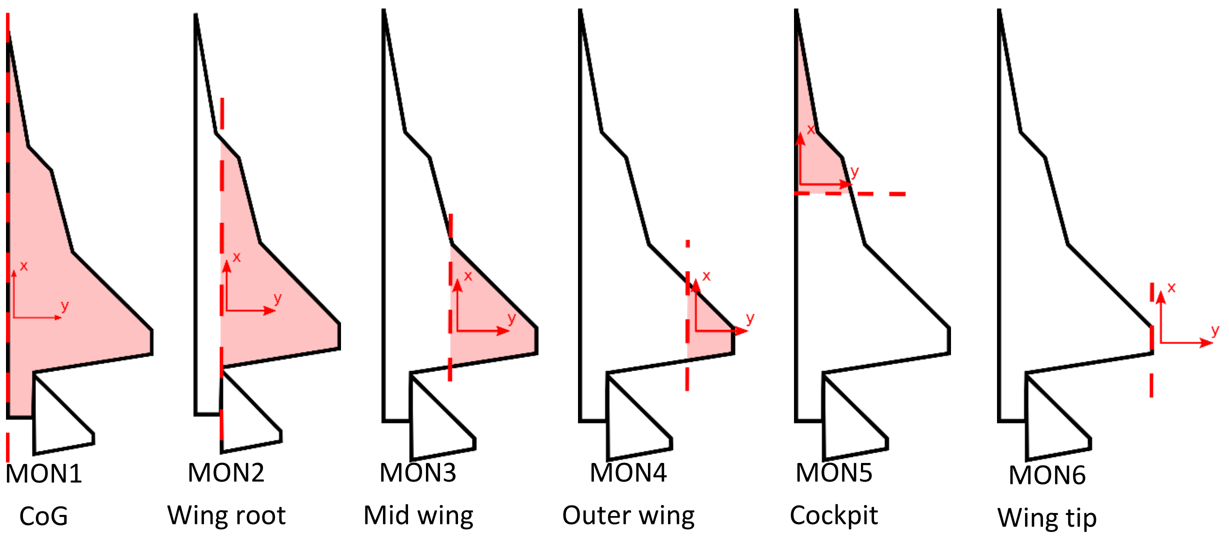

Figure 3.15: Monitoring stations used for the loads analysis on the FFD

3.6. Operating Points

CS25.321(b) mandates the consideration of all relevant parameters within the design envelope for loads analysis, such as airplane configuration, mass configuration, payload, fuel load, thrust, flight speed, and altitude. For gust load analysis, these parameters are extended by a set of gust gradients in the range of $H = 9 - 107\ m$ per operating point [26]. Consequently, these requirements lead to a significant number of load cases for which structural integrity must be demonstrated. To conduct a comprehensive load analysis campaign that identifies the appropriate loads acting on the aircraft, it's crucial to select relevant operating points by considering all critical factors of the configuration and the flight envelope. Since most reports do not provide the operating points used in their investigation, it is often difficult to replicate the results accurately. As already described in Section 2.4, to the author's best knowledge, no publication offers a comprehensive range of relevant parameters for the operating points of a combat aircraft. Most investigations typically concentrate solely on the corner points of the envelope to reduce computing power. Still, as Neubauer and Günther [57] have pointed out, not only the corner cases of the flight envelope, but also the operational points within the envelope should be analyzed as occasionally peak loads occur within the envelope.

In the following section, a comprehensive range of operational points and the underlying assumptions will be presented and discussed. Parameters for the reference model will then be selected according to these considerations, the relevant certification requirements and the literature review presented in Section 2.2.

Mass Configuration

The FAA requires the consideration of specific parameters - weight, center of gravity, payload, and fuel load [20] - in selection of mass configurations. Thus, mass cases should be formed to satisfy a combination of these parameters, depicting feasible configurations. According to CS25.321(b), the flight loads must be calculated at all mass configurations between the minimum and maximum aircraft mass in the respective flight conditions, making consideration of specific mass cases only necessary at their designated flight points and thus providing possibilities to save computational power.

Given that this thesis will present a comprehensive investigation on gust loads, all four mass configurations will be evaluated in combination with each operational point in the flight envelope. Detailed information on different mass configurations is provided in Table 3.2.

Altitude

Combat aircraft typically fly at varying altitudes based on the mission's requirements and tactical situation. They do not have to adhere to flight levels (FL) like civil aircraft, so altitudes are chosen dynamically. As the FFD operates within the mission profiles outlined in Section 3.1 following MIL-STD-3013B, subsequent altitude profiles will be taken into consideration:

I. Low level terrain masking: Altitudes between 0m – 1524m
II. Combat, interception, suppression, and (supersonic) cruise:
Designated design altitudes for optimal performance (OP) between 10973m – 15240m

Additionally, all altitudes with changing reference gust velocities according to MIL-A-8861B and CS25 will be considered, as these changes have a significant impact on the aircraft loads. The changes take place at following altitudes:

I. FL000 (MIL-A-8861; CS25)
II. FL150 (CS25)
III. FL200 (MIL-A-8861)
IV. FL500 (MIL-A-8861; CS25)

To cover the entire height envelope - corner points and points in between the envelope – Table 3.3 presents the utilized altitudes for this work.

Table 3.3: Considered altitudes during the gust load campaign

Flight Level	Altitude in Meters	Consideration
FL000	0 m	Corner point: Highest reference gust velocity
FL100	3048 m	Intermediate point
FL150	4572 m	Corner point: Reference gust velocity change in CS25
FL200	6096 m	Corner point: Reference gust velocity change in CS23/MIL-A-8861
FL300	9144 m	Intermediate point
FL360	10973 m	Corner point: Start of design altitude for OP of the FFD
FL400	12192 m	Intermediate point
FL500	15240 m	Corner Point: Combat ceiling of the FFD

Aircraft Velocities

According to the V-n diagram in Figure 3.16 a), the highest maneuver loads are attained between VA and VD. Given that the most significant load to consider is possibly the combination of maneuver and gust loads, it is necessary to examine the gust loads within this velocity range to capture the peak of the combined loads.

Studies conducted by Handojo and Klimmek [36] indicate that for conventional transport aircraft, the highest gust loads are attained at the design cruise velocity VC situated between VA and VD. As this study aims to examine the instability of the subsonic configuration and compare the characteristics of gust loads in the subsonic and supersonic regimes, it is essential to consider the maximum maneuvering speed VA. This velocity range is predominantly within the subsonic regime and will aid in achieving the objective of the study, which is to analyze not only sole gust loads but also their broader implications. The design dive speed VD, despite reaching higher aircraft speeds, is expected to have less of an impact on gust loads. Because of its lower occurrence probability, gust speeds are halved at VD compared to VC [26], resulting in smaller gust loads. Nevertheless, to encompass the full velocity regime, VD will be considered in the gust load analysis. As the stall speed VS is neither known to produce the highest gust loads, nor to produce the highest maneuver loads, it is omitted in this work. The design velocities will be considered according to their height as seen in Figure 3.16 b).

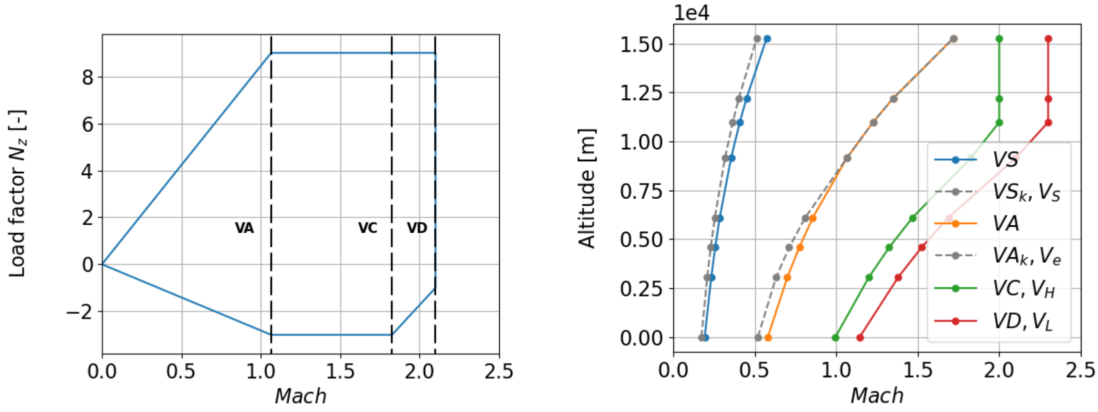

a) Example maneuver envelope b) Design velocities

Figure 3.16: Design velocities and example maneuver envelope for the FFD; civil and military notation

Reference Gust Velocities

The reference gust velocity is vital in the simulation of gust load, serving as the foundation of the loads exerted on the considered aircraft. The following paragraph identifies the appropriate reference velocities for each simulation method and discusses whether uniform reference velocities would be suitable for both the Quasi-Steady Pratt and the dynamic 1-cos gust method.
Chapter 2 discussed how the applicable certification requirements, despite using similar simulation methods, frequently differ when it comes to the reference gust velocity they are based on. This raises the question: why isn't there a universally applicable reference gust velocity for all simulation methods and regulatory bodies? To facilitate comparison between methods, Handojo and Klimmek [36] proposed using the same reference gust velocities for both the Pratt and dynamic gust load methods. However, it is worth noting that the reference gust velocity for both the quasi-steady and dynamic methods do not strictly stem from VGH measurements but is rather a combination of empirical data and historical considerations. As aircraft certified by the step gust method have provided safe flight records, the reference gust velocities in the certification methods were selected so that the newly applied method produces comparable loads to the step gust when applied to the same reference aircraft. Albeit a conservative approach [29], it proved to be efficient and easy way to provide safe flight conditions utilizing the newly introduced certification methods [37]. Therefore, the reference velocities are specifically adapted for the simulation method in question, and selecting alternative reference gust velocities would yield inaccurate outcomes for the methods applied. The corresponding values for each method as stated in the certification requirements JSSG-2006 and CS25 will be selected to maintain comparability with other investigations. For the dynamic 1-cos gust analysis, only civil aviation certification standards such as CS25 are applicable, as no military certification standard currently employs dynamic gust analysis.

Design Gust Velocity

As described in Section 2.1.1, the military standard MIL-A-8861 provides a knock-down factor for reference gust velocities in both subsonic and supersonic regimes. Since the FFD operates within both regimes, Table 3.4 presents the knock-down factor K_g for both regimes according to Equations (2.4) and (2.5).

Table 3.4: Mass ratio μg and knock-down factor Kg for both subsonic and supersonic regimes

	μ_g	${K_g}_{subsonic}$	${K_g}_{supersonic}$
Value	34.5	0.76	0.85

It is apparent that the knockdown factor rises by about 11% in the supersonic regime compared to the subsonic regime. Since the knockdown factor directly affects the load factor, as seen in Equation (2.6), loads in the supersonic regime will scale by 11% if certification standards MIL-A-8861 instead of CS23 are employed.

As described in Section 2.1.2, the dynamic gust load analysis in accordance with CS25 involves various factors that decrease the reference gust velocities based on following assumptions: The reference gust velocity defined in CS25.341 (a)(5)(i) refer to the velocity of a reference gust with a gradient of 107 meters. In order to account for the actual gust velocity, the reference gust velocity must be reduced. This reduction is achieved by normalizing the gust gradient by the reference gust gradient and the sixth root of this value as shown in Equation (2.11). This is done because the maximum velocities for the design gust are proportional to the sixth root of its gust gradient [20]. This also implies that if the gust gradient exceeds the assumed reference gradient length of 107 m in Equation (2.11), the design gust velocities must increase above the peak value of 17.07 m/s as stated in CS25.341 (a)(5)(i). Although not provided for by the certification authorities, this study will use Equation (2.11) without making any further adjustments when inserting gust gradients larger than 107 meters. The elevated gust velocities are demonstrated in Figure 3.17, where the gust with a gradient of 177 meters surpasses the gust velocity of the largest specified gust gradient in CS25.

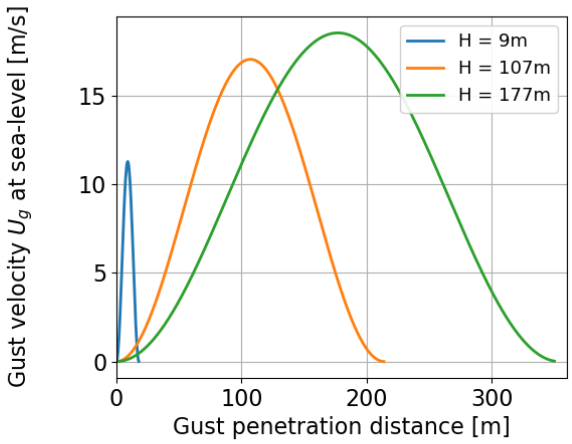

Figure 3.17: Comparison of gust velocities for large gust gradients

Additionally, Equation (2.11) incorporates a flight profile alleviation (FPA) factor F_g, which decreases the reference gust velocities by accounting for the particular mission profile of the considered aircraft configuration. It is minimal at sea level and increases linearly to 1.0 at the service ceiling. The reference gust velocity referred to in Equation (2.11) represents the velocity at each altitude assuming the aircraft flies 100 percent of its service time at that altitude. To account for the probability of the airplane flying at any given altitude during its service lifetime, the factor F_g is then applied. This is primarily employed to reduce anticipated gust velocities for commercial transport aircraft, as these configurations operate at higher cruising altitudes where turbulent encounters are less severe. Figure 3.18 depicts the altitude-dependent variation of F_g, comparing the DLR FFD, and the DLR XRF1, a long range transport configuration.

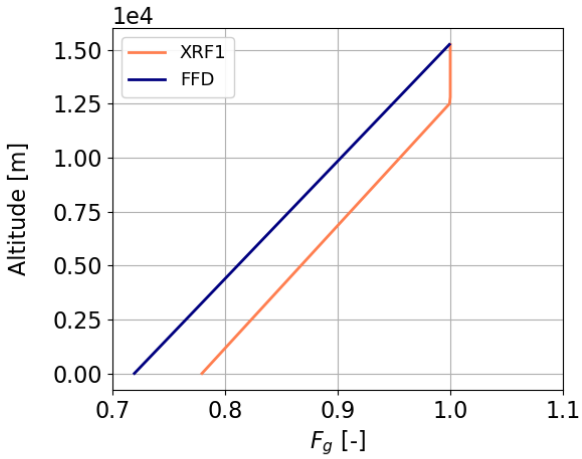

Figure 3.18: Flight profile alleviation factor Fg of the DLR FFD and the DLR XRF1

It is evident that the reference gust velocities for the FFD would be significantly reduced at low heights, especially when compared to the civil transport aircraft. Combat aircraft are expected to operate on a range of mission profiles at dynamic altitudes and speeds, making a high alleviation of reference gust velocities as seen in Figure 3.18 rather implausible. Therefore, in absence of a more rational approach, the FPA factor F_g is selected to 1.0 for this investigation, which means that the aircraft flies equally at all altitudes and unintended alleviation of gust loads is avoided.

Another factor to consider is the estimated service life of the aircraft. According to the FAR25 Advisory Circular [20], reference gust velocities are peak impacts assumed to occur once during the aircraft's service life approximately every 70,000 flight hours. Advanced combat aircraft have a significantly lower service life of around 6,000 - 8,000 hours [71,77], so the likelihood of the most severe gust impact is significantly lowered. Thus, the gust intensities could be decreased by a knockdown factor including the service life for non-conventional configurations. At the same time, as seen in Figure 3.19, the reference gust velocities cannot simply be decreased by the same factor as the proportional service life. A new probability of exceedance would need to be selected based on various factors. The concept of applying a service life alleviation factor may be of interest in future studies. However, it falls beyond the scope of this thesis. Therefore, a conservative approach is adopted, and no knockdown factor will be considered for the aircraft's service life.

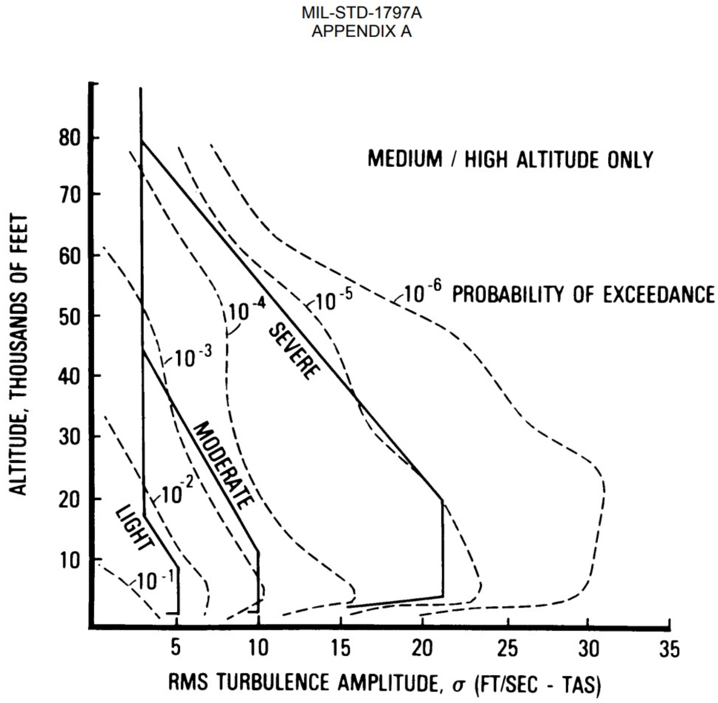

Figure 3.19: Turbulence severity and exceedance probability, extracted from [23]

Gust Gradients

The dynamic gust analysis is, in contrast to the quasi-steady analysis, sensitive to a change in gust gradient length. Hence, variation of gust gradients can significantly impact resulting loads, particularly in supersonic combat aircraft. According to certification requirements CS25 and MIL-STD-1797 [89], it is necessary to determine the suitable tuning of gust gradients based on the aircraft's natural frequencies and control system. A range of 10-20 distinct gust gradients is recommended to precisely capture the system's response to different gradients [20]. Due to the unique aerodynamic characteristics and operating conditions of supersonic fighter jets, the recommended gust gradient distance may potentially differ from that of subsonic civil aircraft as suggested in CS25. This consideration aligns with the publications of Lube et al. [51], Chapman [15] and Fuller [29], which were presented in Chapter 2.2.

Based on these considerations, Table 3.5 denotes the four selected gust gradient sets for this investigation and presents the rationale behind the selection:

Table 3.5: Selected gust gradient sets for the dynamic analysis

Designation	Rational
CS25	Gust gradient set required by CS25 in the range of 9-107 meters [21]
Long	Long gradient set incorporating recommendation of Lube et al. [51] and Chapman [15] to consider gust gradients up to a length of 25 spatial chord lengths; Investigate if influence of large gust gradients is increased during supersonic flight [29]
Short	Short gradient set to test the influence of short gust gradients on the resulting accelerations at the wingtip [15]
Pratt	Gradient set implementing the gust gradient of 12.5 spatial chords used in the Pratt method [65]

Due to the short gust gradients used in the short gradient set it is necessary to adjust the reduced frequencies of the AICs. The reduced frequency of the gust is calculated by

$$k_{gust} = \frac{\pi * c}{2 * H} \tag{3.10}$$

with the reduced frequency

$$k = \frac{\omega * c}{2 * V} = 2\pi f * \frac{c}{2 * V} \tag{3.11}$$

and the gust base frequency

$$f_{gust} = \frac{V_{TAS}}{2 * H} \tag{3.12}$$

Inserting the smallest gust gradient into this formula results in a maximum reduced frequency of $k = 5.3$. Therefore, AICs up to a reduced frequency of $k = 5.3$ are required for the short gradient set. Table 3.6 shows the final resulting operating points of the gust load envelope.

Table 3.6: Overview of gust load cases

	Number	Description
Mass configuration	4	M1 (MTOM), M2 (BFDM P/L), M3 (BFDM no P/L), M4 (OEM)
Altitudes	8	FL000, FL100, FL150, FL200, FL300, FL360, FL400, FL500
Velocities	3	VA/MA, VC/MC, VD/MD
Gust gradient sets		
CS25 set	*11*	H = {9, 18, 27, 37, 47, 57, 67, 77, 87, 97, 107}
Long set	*7*	H = {117, 127, 137, 147, 157, 167, 177}
Short set	*4*	H = {2, 4, 6, 8}
Pratt set	*1*	H = {84.125}
Total gust gradients	23	
Gust directions	2	0° (From bottom), 180° (From top)
Total	4416	

Gust Direction

CS25 mandates the consideration of vertical gust from both directions, once from the bottom with an inclination of 0° and a gust from the top with an inclination of 180°. Therefore, vertical gusts both in positive and negative z direction as depicted in Figure 3.20 will be considered in this work.

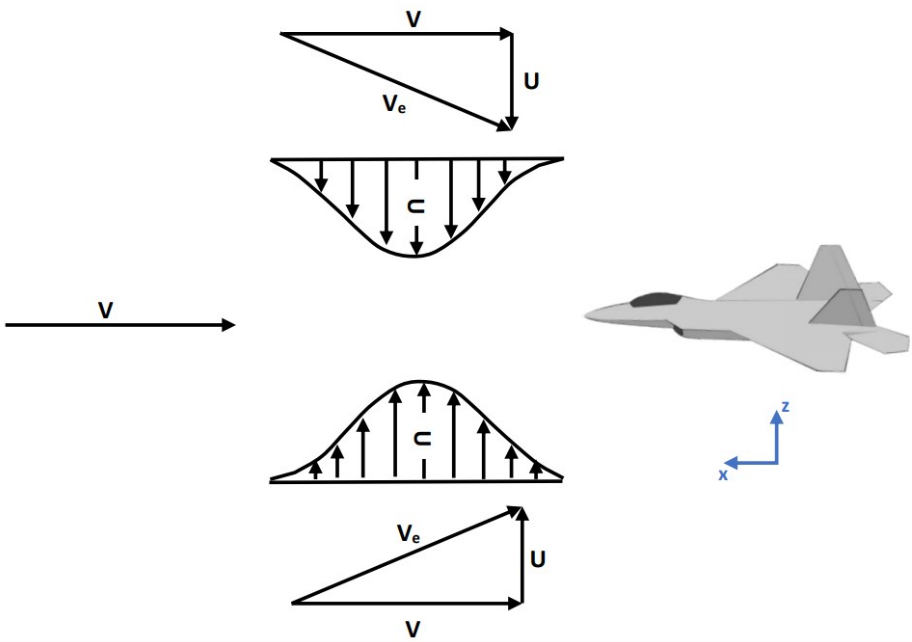

Figure 3.20: Vertical 1-cos gust

Superposition of Maneuver Loads

During combat operations, it may be necessary to perform maneuvers with high vertical acceleration despite turbulent air conditions. As gust loading is cumulative with pilot induced loading, certification requirements for combat aircraft require consideration of the superposition of maneuver and gust loads. Especially during low altitude terrain following operations, the aircraft structure can be subjected to simultaneous gust and maneuver loads [84]. For this reason, the resulting acceleration on the aircraft due to turbulent air and their superposition with maneuver loads in accordance with MIL-A-8661B 3.5.1.2 will be discussed to determine whether turbulent air can be a potential factor for exceeding the structural limits of the aircraft.

3.7. Deflection Rate Limits

As discussed in Section 2.3, overoptimistic deflection rates that do not reflect the current capabilities of combat aircraft can produce misleading results. Therefore, to resemble the actual behavior of modern combat aircraft, this work adopts the deflection rate limits of the actuators integrated in the Lockheed Martin F-22 Raptor [5], shown in Table 3.7, which is a current-generation combat aircraft with comparable capabilities to the DLR Future Fighter Demonstrator.

Table 3.7: Control surface deflection limits of the F-22 Raptor, extracted from [99]

Control surface	Deflection limit	Rate limit
Aileron	±25 degrees	70 degrees/s
Horizontal tail	-25 to +30 degrees	60 degrees/s
Rudder	±30 degrees	80 degrees/s

4. Control System Development

As the flight dynamics of an aircraft vary significantly throughout the flight envelope and different operational points, it is important to implement measures ensuring that the aircraft's handling qualities remain satisfactory at all times. These measures are particularly relevant for military combat configurations, which typically shift from open-loop instability in the subsonic regime to open-loop stability in the supersonic regime. An electronic flight control system (EFCS) is therefore a critical requirement for meeting the military design criteria of a combat aircraft, establishing a feasible design envelope and constraining the operational range. Simultaneously, design of an effective flight controller poses a challenging task as the requirements of stability performance, flight attitude control, and disturbance rejection for phenomena like turbulences and pilot-induced oscillation (PIO) can be in contrast with accomplishing the desired agility criteria.

The subsequent chapter presents the design and implementation of a simplified longitudinal control system for the DLR Future Fighter Demonstrator. This control system is intended to stabilize and reduce pitch instability in the longitudinal axis to enable feasible gust computations. Other sections of the EFCS are disregarded due to the scope of this work. The controller design will be based on the certification requirements for control systems of military combat aircraft MIL-DTL-9490E [86] and take into account the best practices for flight control design of combat aircraft compiled by NATO [55].

4.1. The Necessity for a Flight Control System

Similar to other fighter aircraft such as the Eurofighter [10], the DLR FFD is designed to be unstable in the subsonic regime, providing for enhanced agility during combat action. This instability results from the location of the aerodynamic center's (AC), positioned slightly in front of the CG, making the aircraft marginally unstable. In the supersonic regime, the AC is located behind the CG, resulting in a stable configuration. The relationship between the location of the aerodynamic center and stability is visualized in Figure 4.1. The CG is represented by a large yellow sphere, while the smaller red sphere indicates the aerodynamic center. The longitudinal instability is determined geometrically by the static margin

$$SM = \frac{X_{AC} - X_{CoG}}{c} \tag{4.1}$$

And in terms of aerodynamic derivatives determined by

$$C_{m\alpha} = \frac{\partial C_m}{\partial \alpha} \tag{4.2}$$

The static margin (SM) is compared for both flight conditions in Table 4.1.

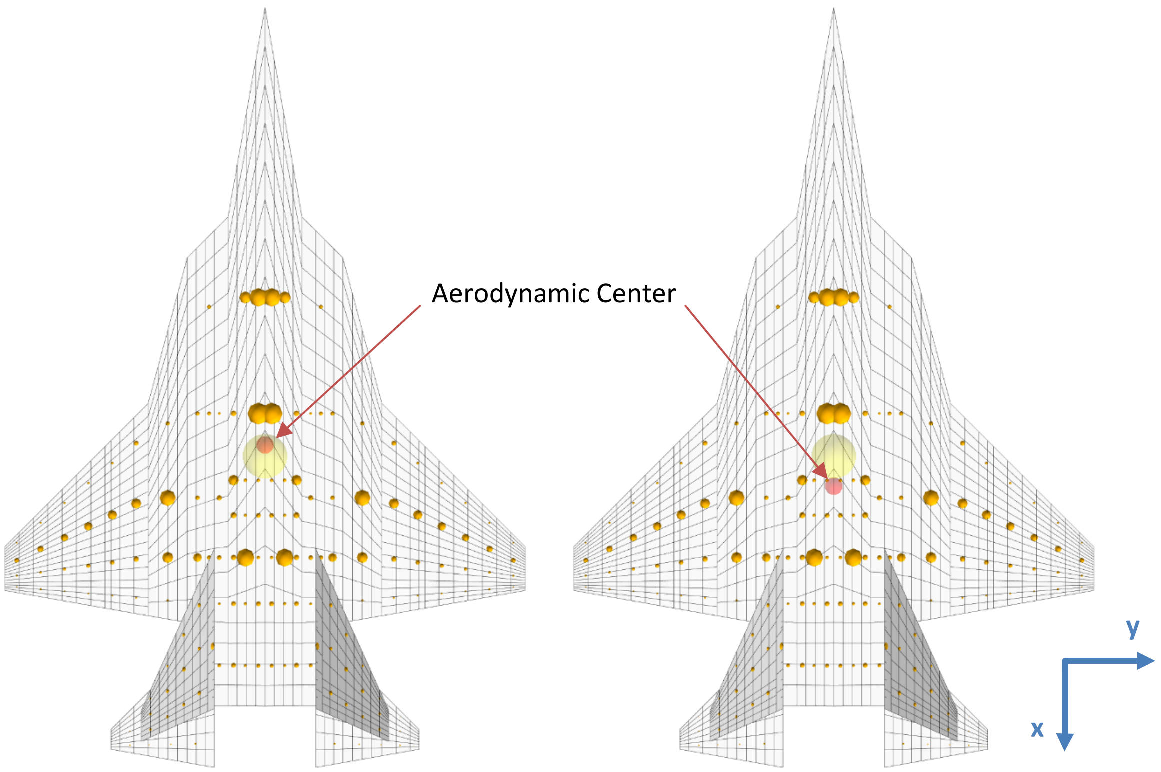

a) Subsonic regime b) Supersonic regime

Figure 4.1: Location of the aerodynamic center for the subsonic and supersonic flight state

Table 4.1: Comparison of static margin for subsonic and supersonic flight states

	Mass Case	Velocity	Static Margin
Subsonic regime	M2	Mach 0.5	-4.8 %MAC
Supersonic regime	M2	Mach 2.0	12.6 %MAC

Aircraft that exhibit a negative static margin (SM) or negative stability derivative $C_{m\alpha}$ are considered unstable and experience greater turbulence reactions than stable configurations, making them correspondingly more challenging to control. When a stable aircraft encounters a turbulent field, the resulting increase in angle of attack creates a counteracting pitching moment that reduces the pitch angle and the load factor. On the contrary, gust disturbances on an unstable configuration result in a positive pitching moment, leading to divergence of the aircraft. Figure 4.2 demonstrates the open-loop instability for gust impacts, presenting the response of the pitch angle Θ, load factor N_z, and pitch rate q to various gusts with gradients between 9 and 107 meters. The responses for the subsonic unstable (a) and the supersonic stable configuration (b) are shown.

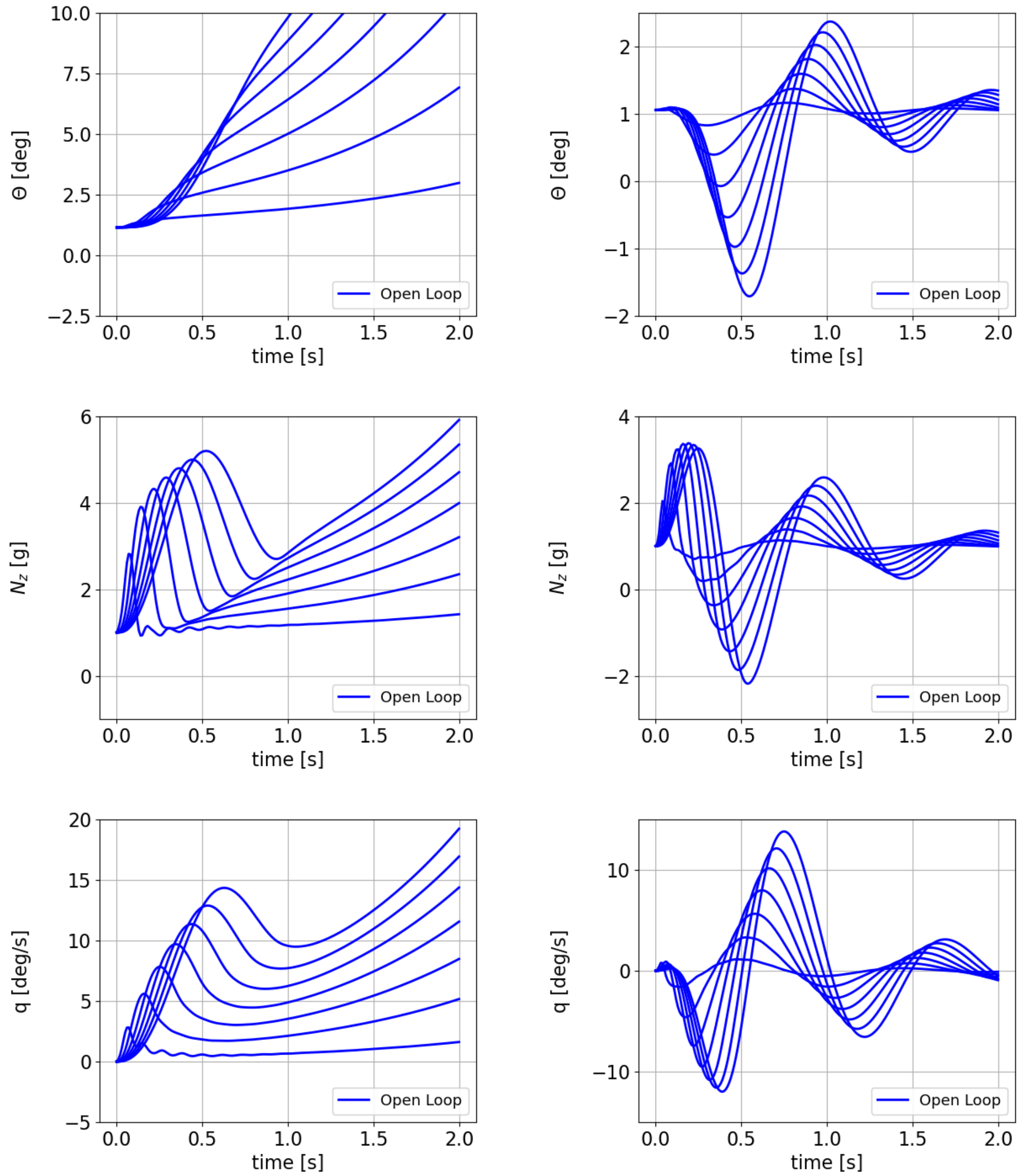

a) Subsonic regime

b) Supersonic regime

Figure 4.2: Response of pitch angle Θ, load factor Nz and pitch rate q to a range of gusts in both stability configurations

As shown in Figure 4.2 a), the gust encounter leads to an initial increase in angle of attack, which in turn induces an initial rapid pitch rate requiring swift corrective action. However, passive aerodynamic forces are unable to counteract this increase in AoA and as a result, the aircraft diverges, making gust calculations in this unstable configuration unfeasible. Although the stable configuration shown in Figure 4.2 b) does not diverge and seems to return to its initial state, the oscillation decreases at a slow rate.

As a result, the observed behavior makes it impractical to perform gust computations of the current configuration and thus, a control system is required to stabilize this divergence.
As a preliminary measure in implementing a control law, the analytical evaluation of instabilities may be attained through the system's poles. These are derived from the state space matrix A by

$$poles_{sys} = eig(A_{sys}) \tag{4.3}$$

Figure 4.3 illustrates the poles and the according mode contribution for the full system at a speed of $V_{EAS} = 170\ m/s$. The dashed lines in the upper plot shows the pole movement with respect to increasing velocity up to $V_{EAS} = 240\ m/s$. The lower plot shown in Figure 4.3 illustrates the modal participation factors, with the x-axis displaying the modes and the y-axis demonstrating the respective states influencing the mode under consideration. The modal participations have been normalized between 0.0 and 1.0, as indicated by the color bar. States designated as Uf indicate elastic displacements, while the superscript ' denotes states within the FEM coordinate system. The states u and x are omitted due to numerical reasons (as discussed in Section 3.2, no drag is considered in the DLM nor ZONA51), resulting in the absence of the phugoid mode. In this subsonic regime, pole 0 is situated on the positive real axis, indicating the longitudinal instability originates from this *flight mechanical heave mode*. Analysis of the modal participation of the pole 0 reveals that the largest contributions stem from the integrator z and rigid body velocity w. As for pole 2, it shows modal participation not just from the integrator z and rigid body velocity w, but also a slight participation indicated by light yellow coloring from the pitch rate q and the first symmetrical wing bending mode Uf4. Therefore, pole 0 and pole 2 most likely jointly form the short period mode but have separated and shifted to the real axis. As Mach numbers increase, pole 0 shifts towards the negative real axis while pole 2 shifts towards the positive real axis. If depicted over a set of increasing velocities, they converge on the negative real axis in the supersonic regime, forming a conjugated complex pole pair. Pole 1 is a *rolling mode* while the poles 3 and 4 depict a *coupled antisymmetric fuselage bending and torsion mode*, as they are impacted by the roll rate p and yaw rate r, along with a substantial influence from the first fuselage torsion mode Uf1 and the asymmetrically combined wing and vertical stabilizer bending mode Uf6.

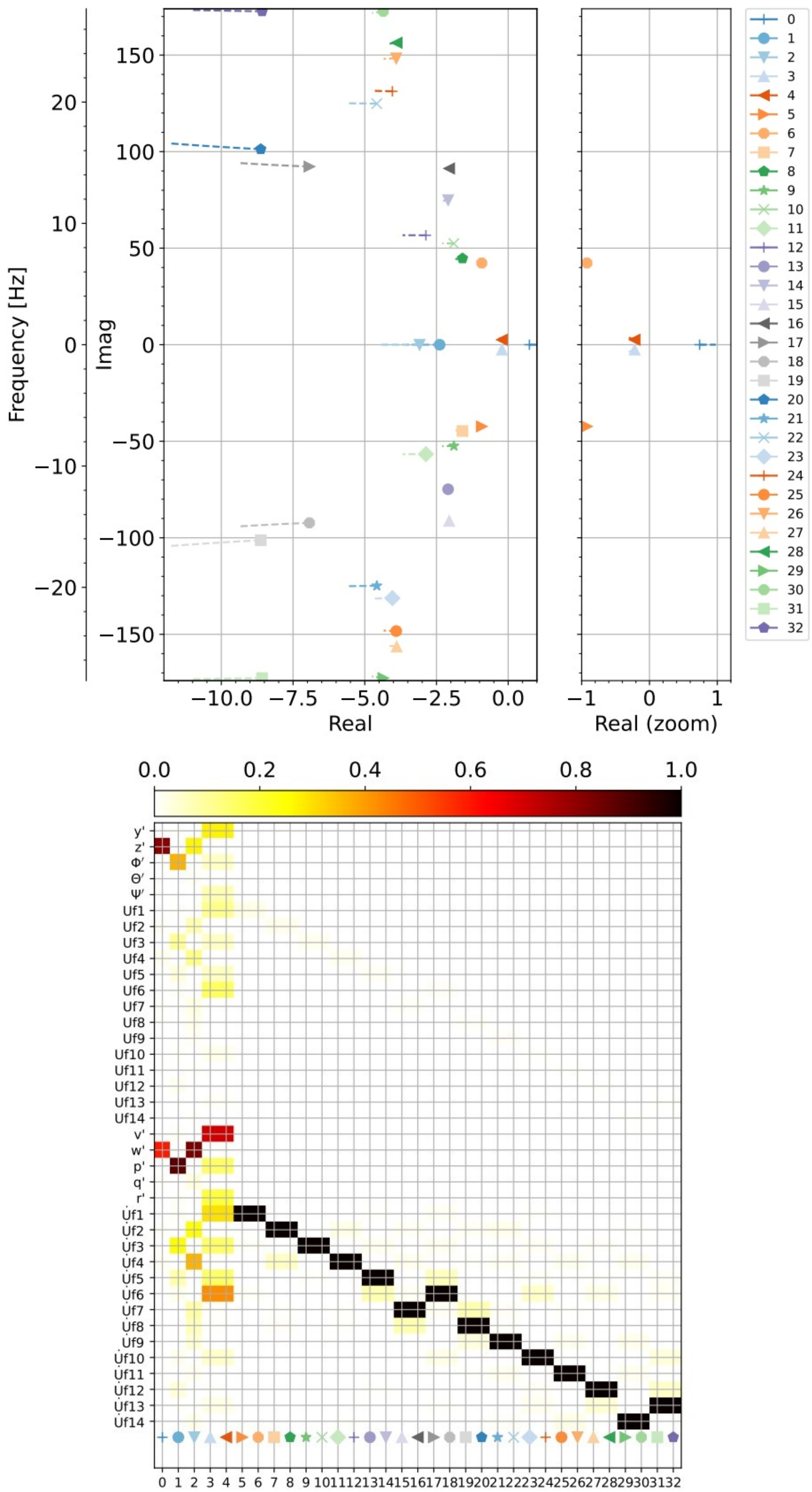

Figure 4.3: Eigenvalues and modal participation, M2, FL000, Ma04-Ma06

4.2. Analysis Methodology and Derivation of Gains

To stabilize the configuration, it is necessary to shift the *flight mechanical heave mode* from the positive real axis to the negative real plane. To achieve this, a stability augmentation system (SAS) will be implemented to address the longitudinal instability in the DLR FFD configuration. The following chapter will discuss the parameters necessary to achieve optimal behavior of the control system and present methods to derive appropriate gains for the introduced SAS control system.

Table 4.2: Aircraft categories and characteristics as specified by MIL-F-8785C

Airplane Classes	
Class I:	Small, light airplanes
Class II:	Medium weight, low-to-medium-maneuverability airplanes
Class III:	Large, heavy, low-to-medium-maneuverability airplanes
Class IV:	High-maneuverability airplanes
Flight Phases	
Category A:	Nonterminal flight phases generally requiring rapid maneuvers
Category B:	Nonterminal flight phases generally requiring gradual maneuvers
Category C:	Terminal flight phases generally requiring gradual maneuvers
Flying Quality Levels	
Level 1:	Flying qualities adequate for the mission flight phase
Level 2:	Flying qualities adequate to accomplish the mission flight phase, but increased workload on the pilot
Level 3:	Flying qualities adequate to control the airplane safely, but excessive workload on the pilot or inadequate qualities for the mission

Table 4.3: Relative damping requirements ζ_required according to Flight phase and level of Flying qualities as specified by MIL-F-8785C

Level	Flight Phase A and B		Flight Phase B	
	Minimum	Maximum	Minimum	Maximum
1	0.35	1.30	0.3	2.00
2	0.25	2.00	0.2	2.00
3	0.15	-	0.15	-

The optimal gains for the SAS will be derived according to certification requirements outlined in MIL-F-8785C. Table 4.2 displays various aircraft characteristics that determine the required parameter ranges. Based on the aircraft characteristics of the FFD, the necessary relative damping range can be obtained in MIL-F-8785C, which is provided in Table 4.3. The required relative damping value for Flight Phase A and Level 1 flying qualities ranges between $\zeta_{required} = 0.35 - 1.3$. According to Holzapfel [38], the nominal optimal value is $\zeta_{opt} = \frac{\sqrt{2}}{2}$.

The desired frequency is not directly specified in the requirements; however, it can be indirectly determined through the Control Anticipation Parameter. Through this parameter, Kaminski [42] identified an acceptable range of $\omega_{required} = 2 - 4\ {rad}/_{s}$. To obtain a more precise value, the intervals for $\zeta_{required}$ and $\omega_{required}$ are compared to the results of a fighter pilot survey during target tracking missions conducted by Chalk [14], shown in Figure 4.4. To attain optimal pilot satisfaction for flying qualities, appropriate longitudinal control system design values are chosen to

$$\zeta_{opt} = \frac{\sqrt{2}}{2}\ and\ \omega_{opt} = 3\ {rad}/_{s} \tag{4.4}$$

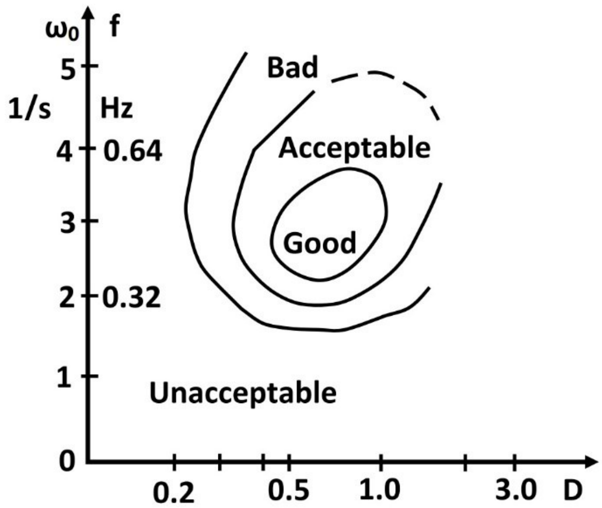

Figure 4.4: Pilot assessment of handling qualities for different characteristics of the short period mode, derived from [7]

The basic transfer function for a liner 2nd order system

$$TF(s) = \frac{\alpha(s)}{\eta(s)} = \frac{{\omega_0}^2}{s^2 + 2\zeta\omega_0 s + {\omega_0}^2} \tag{4.5}$$

therefore yields following equation when the optimal values ζ_{opt} and ω_{opt} are inserted

$$TF(s) = \frac{\alpha(s)}{\eta(s)} = \frac{9}{s^2 + 3\sqrt{2}s + 9} \tag{4.6}$$

The resulting transfer function is depicted in Subfigure Figure 4.5 a), with Subfigure b) depicting the comparison of the optimal behavior with the upper and lower limits for the relative damping provided in Table 4.3.

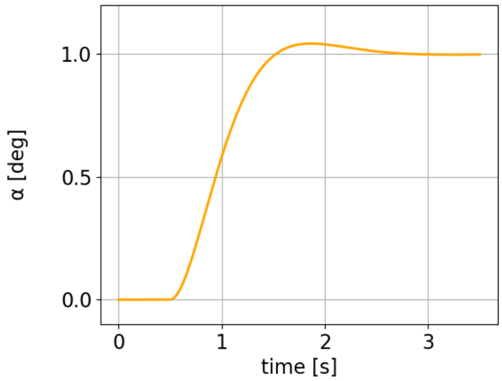

a) Desired transfer function

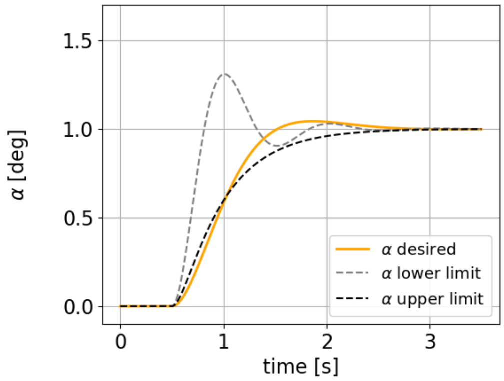

b) Comparison to ζ_required

Figure 4.5: Transfer function for a step input of one, using the optimal values ζ_opt and ω_opt in comparison with the upper and lower limits for ζ_required of flight phase 1

Derivation of gains through a reduced short period model

To stabilize the short period of an aircraft, literature on control design [10,81] suggests reducing the system of equations to the angle of attack α and pitch rate q, as these states exhibit the most significant influence on the short period mode. This approach is often used as a demonstration case, displaying numerous simplifications, including the assumption of a stable configuration. A second-order reduced system is then derived from the full system of equations based on the two states:

$$\begin{bmatrix}\dot{\alpha}\\ \dot{q}\end{bmatrix} = \begin{bmatrix}Z_\alpha & Z_q + 1\\ M_\alpha & M_q\end{bmatrix}\begin{bmatrix}\alpha\\ q\end{bmatrix} + \begin{bmatrix}Z_\eta\\ M_\eta\end{bmatrix}\eta \tag{4.7}$$

Cramer's rule and a root locus analysis aid in deriving the transfer functions $TF_{\eta\rightarrow\alpha}$ and $TF_{\eta\rightarrow q}$, enabling analytical derivation of the proportional gains for the control system loops. To maintain an analytically linearized solution, integral control is omitted due to its non-linear characteristics. The proportional gain of the actuator will be set to a high value to linearize the dynamics and allow for unrestricted deflection rates. For the derivation of these formulas, refer to Stevens and Lewis [81].

The resulting equations to derive the proportional gains are

$$K_{P_{pitch}} = \frac{2\zeta\omega_0 + Z_\alpha + M_q}{M_\eta} \tag{4.8}$$

$$K_{P_\alpha} = \frac{2\zeta\omega_0 + Z_\alpha + M_q}{Z_\eta} \tag{4.9}$$

$$K_{P_{attitude}} = K_{P\alpha} * \frac{1}{-\frac{V_0}{g} * Z_\alpha} = \frac{2\zeta\omega_0 + Z_\alpha + M_q}{-\frac{V_0}{g} * Z_\alpha Z_\eta} \tag{4.10}$$

The gains obtained from Equations (4.8) to (4.10) are then evaluated for each operational point and integrated into the control system structure. Despite closed-loop gust simulations with these gains, the gust response remains unstable, and the control system is unable to stabilize the longitudinal divergence from the trim point. To identify the source of the ongoing instability, the poles of the reduced system are reevaluated. In Figure 4.6, the poles of the complete system are compared with those of the reduced second-order system (displayed in black). It is apparent that the pole that causes the longitudinal instability is not present in the second-order system. Therefore, this reduced order model is insufficient to stabilize or decrease the instability of the system unless the unstable heave dynamics are explicitly encapsulated in the system. As this method cannot supply the necessary gains to stabilize the configuration, this work will adopt an alternative approach.

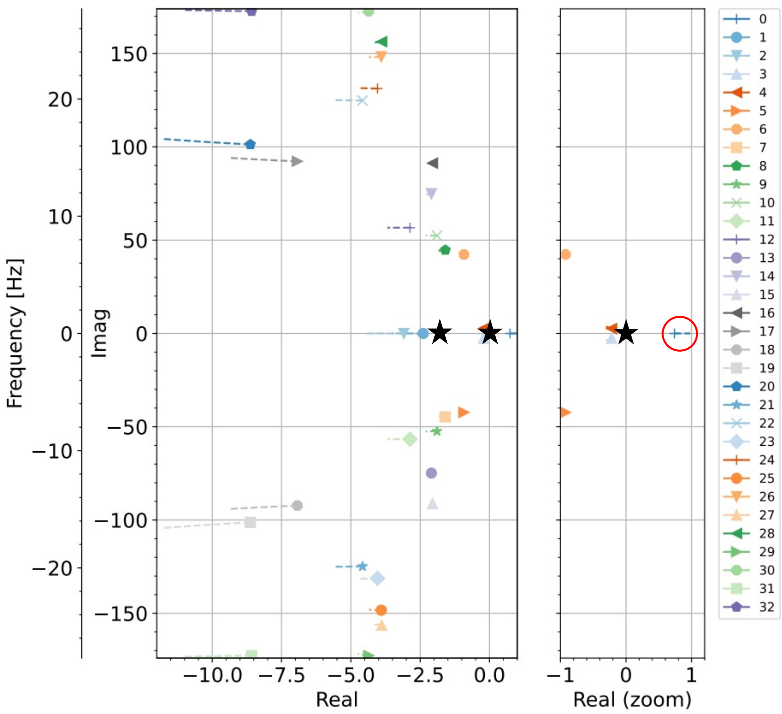

Figure 4.6: Pole comparison of the reduced 2DoF system to the full system

Derivation of gains through an optimization approach using a Genetic Algorithm

The control gains of the complete control architecture will be obtained using an iterative optimization approach employing a genetic algorithm. This procedure involves simulating the behavior of the entire system, including all its states, in the state space model to determine the gains which achieve the maximum fitness for the imposed cost function. The algorithm will be applied independently to each operational point following its linearization. The genetic algorithm assigns different values for the gains of the control system. Depending on the velocity, the system uses different reference inputs to track the desired transfer function. The system is then subjected to a step-input of defined magnitude. Figure 4.7 shows the resulting step response plotted against the step response of the desired behavior derived from Equation (4.6). The genetic algorithm performs iterations on different gains to determine the optimal values such that the two curves satisfy

$$\min(A) = min\left(\int \left|Y_{desired} - Y_{current\ gains}\right|\right) \qquad \textbf{(4.11)}$$

with additional penalties enforced onto the function fitness for oscillating behavior and slow rise time in addition to the minimization of the area between the curves.

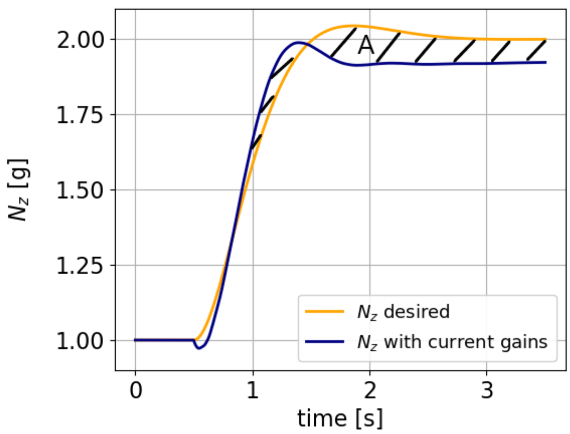

Figure 4.7: Comparison of aircraft behavior to a step input with current gains compared to the ideal behavior

4.3. Proposed Architecture for a Simplified Stability Augmentation System

In the preliminary design of flight controllers, the focus is on obtaining estimations of the most favorable controller structure rather than exact results. As the induced aircraft dynamics still vary significantly across the flight envelope, the operating points will be linearized in the state space system, and the control law is tuned to various configurations based on mass case, flight level, and velocity regime. The SAS control architecture displayed in Figure 4.3 will be implemented to address the longitudinal instability for the full closed-loop system of the DLR FFD configuration. Deflection rate limit filters are implemented as described in Section 3.7, which maintain the aircraft dynamics within reasonable limits and possibly remove Pilot Induced Oscillation (PIO) tendencies as a side effect. Employing three cascaded loops, the SAS is designed with the following structure:

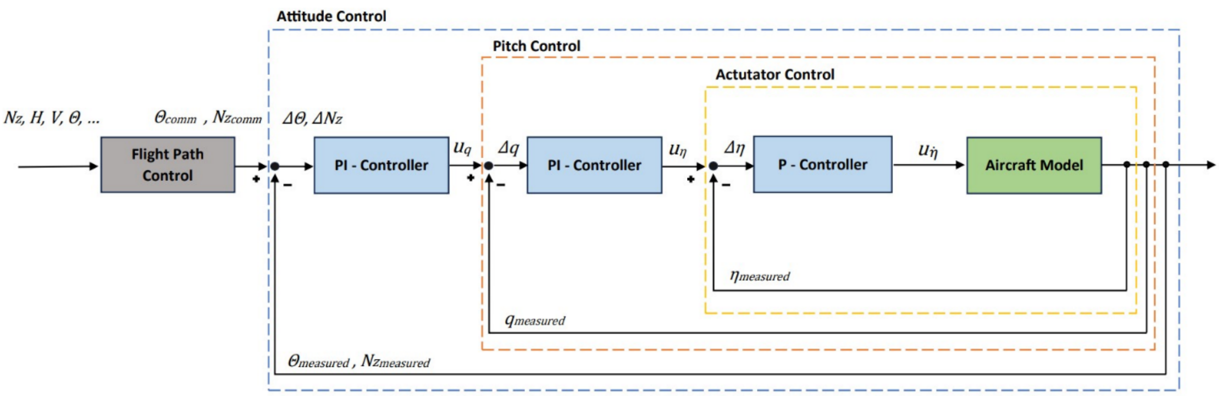

Figure 4.8: SAS to control longitudinal instability of the DLR FFD configuration allowing for feasible gust analysis calculations

According to Stevens and Lewis [81], either the angle of attack α or load factor N_z are the most suitable reference inputs to adjust longitudinal stability in agile combat aircraft. When flying at low speeds, the maximum angle of attack places limitations on the achievable vertical load factor since the aircraft would stall before reaching its limit. Meanwhile, at high speeds, the airframe would first reach the structural load limit before the airplane stalls. The intersection of the AoA limit and the vertical load factor limit is commonly referred to as the corner point of the V-n diagram, which coincides with the maximum maneuver speed VA. Figure 4.9 illustrates the position of the corner point on the V-n diagram.

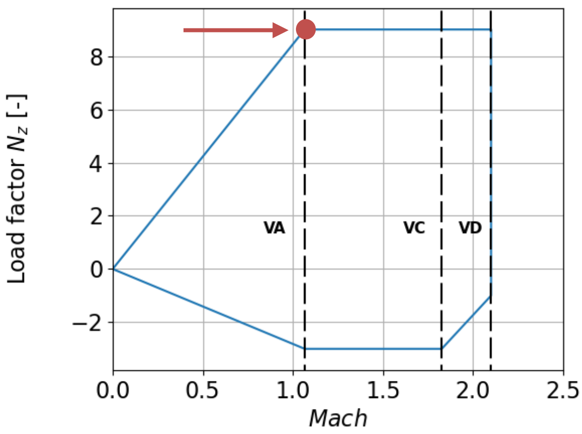

Figure 4.9: Example V-n diagram depicting the location of the corner point

To satisfy these characteristics, it is best to utilize a blend of angle-of-attack reference input below the corner point and vertical load factor as reference input for speeds above the corner point. This velocity-based reference input is referred to as corner point control and is also applied in the Eurofighter Typhoon [10] (Brockhaus, Chapter 19.3.1). Since high bandwidth measurement of the angle of attack α is often not possible, the pitch angle θ substitutes for the reference input.

The section below provides a thorough analysis of each control loop and the corresponding gains. Final gains $K_{P\_attitude}, K_{I\_attitude}, K_{P\_pitch}, K_{I\_pitch}, K_{P\_actuator}$ for all flight states of mass case M1, determined by the optimization algorithm, are illustrated in Figure 4.10, Figure 4.12 and Figure 4.14. As this control design employs the corner point control, the study will solely focus on the gains of the pitch angle Θ for velocity regime VA and velocity regimes VC and VD for the load factor N_z.

Attitude Control

The attitude control's control architecture is presented in Figure 4.10. It incorporates a PI controller, where the proportional component increases the aircraft's stability, and the integral component provides stationary accuracy by compensating for gain scheduling errors. The PI controller receives the error between the desired and measured attitudes to provide a command for the pitch rate u_q necessary to achieve the desired attitude.

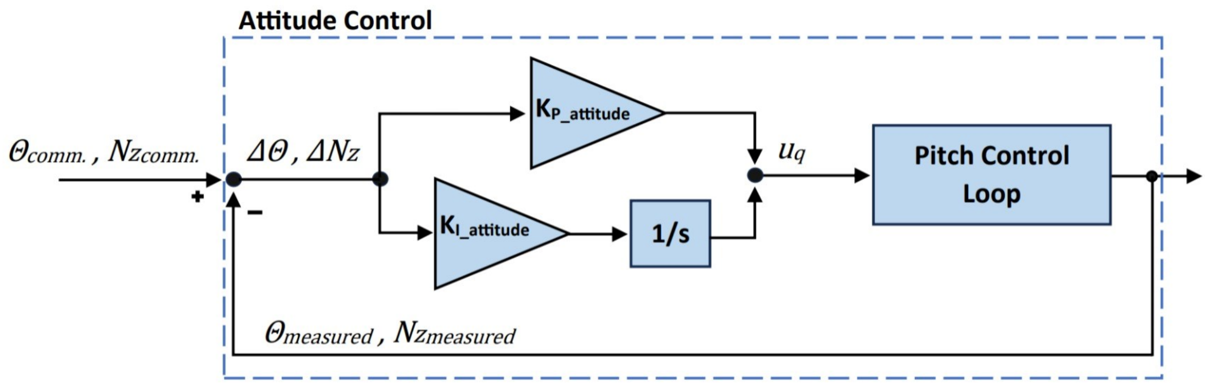

Figure 4.10: Control architecture for the outer attitude control loop

The gains obtained for the attitude loop are illustrated in Figure 4.11. Subfigure a) displays the velocity VA and reference input of theta. It is noticeable that, in the subsonic range, the proportional gains are greater than in the supersonic range and gradually decrease to nearly zero with rising altitude, whereas the integral gain appears to increase in the same interval. When the proportional gain decreases, it appears that a higher integral gain is used to ensure steady state accuracy. With the load factor as the reference input in Subfigures b) and c), there appears to be less consistency in the gains compared to Subfigure a). Specifically, Subfigure b) demonstrates that within the subsonic regime, both the proportional and integral gains are initially high but decrease with altitude. However, the gains do not conform to a stable pattern such as in Subfigure a) and instead oscillate around a mean value. Same characteristics can be observed for Subfigure c). The optimization algorithm aims to identify the numerically optimal gains, which can lead to considerable fluctuations. This behavior could possibly be averted by penalizing gains that divert too far from the medium in the same flight regime, provided there is no significant improvement in function fitness.

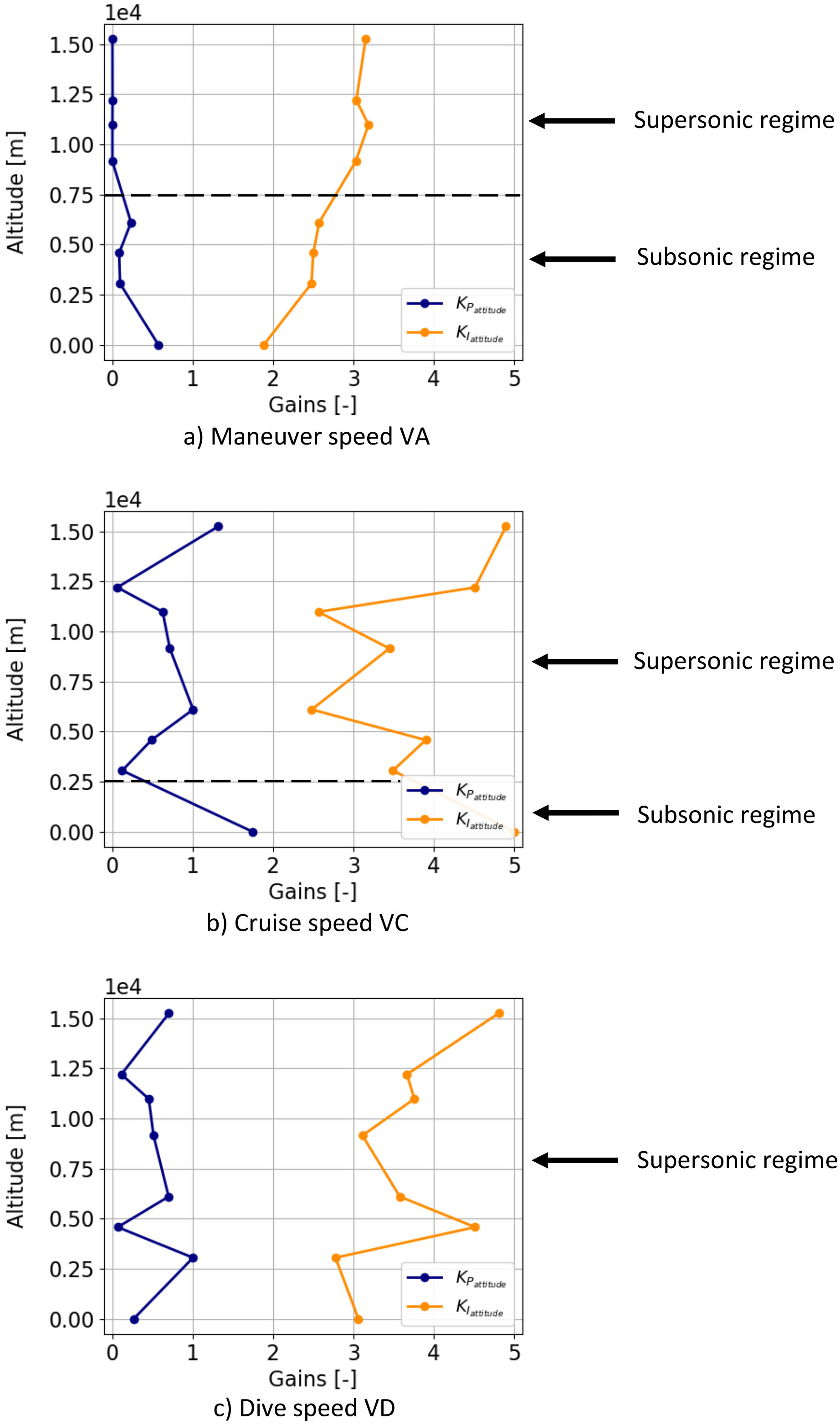

Figure 4.11: Derived gains for the attitude control

Pitch Control

The relative damping of the longitudinal instability is adjusted through control of the pitch rate q. Figure 4.12 depicts the pitch rate control loop including a PI controller, receiving the error between the commanded and measured pitch rates u_q and $q_{measured}$. The resulting command provides the required elevator deflection u_η to obtain the desired pitch rate u_q.

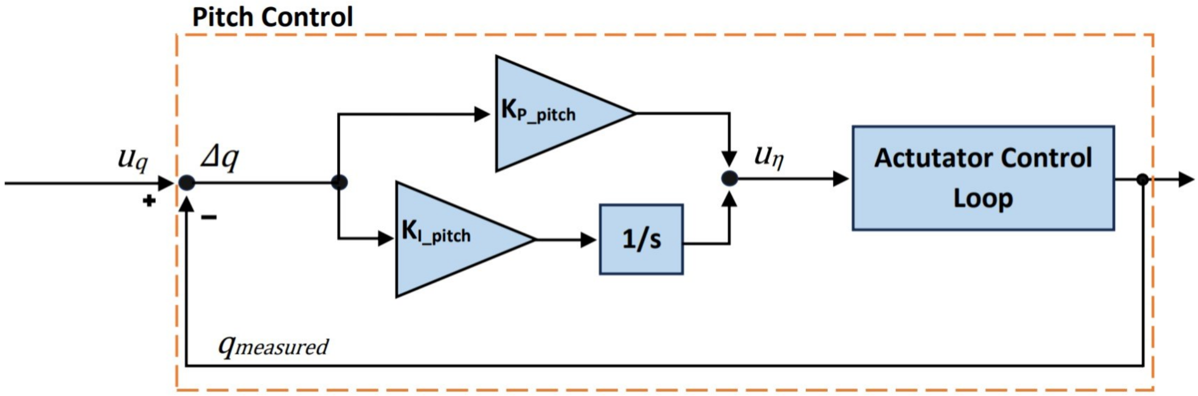

Figure 4.12: Control architecture for the outer pitch control loop

The resulting gains for the pitch control displayed in Figure 4.13 a) through c) indicate that smaller gains are required in the unstable case, whereas higher gains are necessary in the stable case. Notably, for reference input of load factor, there is a relatively clear trend observed in the gains. This non-oscillatory behavior is also observed for reference input theta in the subsonic regime of Figure 4.13 a). In contrast to Figure 4.12, in the supersonic stable regime the proportional gains appear to oscillate, with the integral gains reach the imposed maximum limit set to 5.0. It seems that the majority of control action is already initiated by the attitude control, except for the supersonic range of VA, where a noteworthy amount of damping is required from the pitch controller. This leads to the large gains required at these flight points.

Based on Figure 4.13 b) and c), as well as Figure 4.13 a), it appears that there are similar gains for comparable flight regimes within the envelope. To reduce computational effort, it may be possible to derive gains only for corner cases and then extend the results to similar flight regimes within the flight envelope. Nonetheless, it is necessary to conduct a sensitivity margin analysis to determine the impact of tuning the gains on the dynamic behavior of the closed-loop system. However, this study did not investigate sensitivity margins or similar approaches as a detailed analysis within control theory is beyond the scope. As a result, this work will utilize the exact gains obtained from the algorithm without any further modifications.

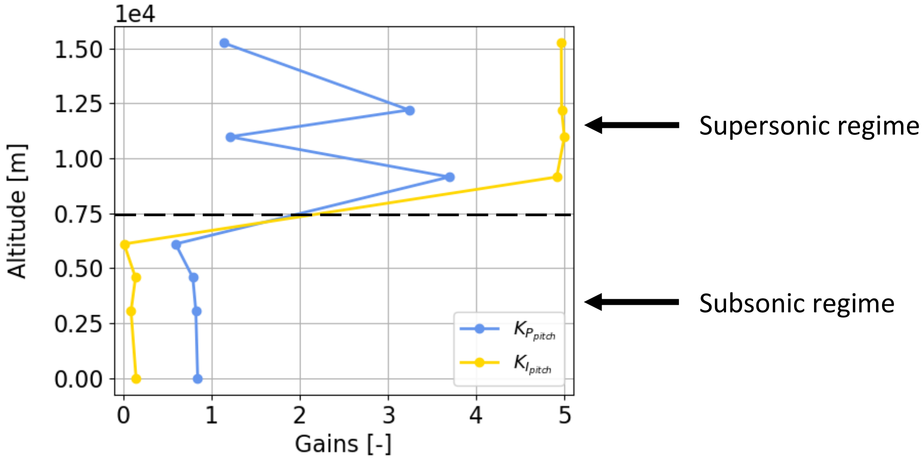

a) Manuever speed VA

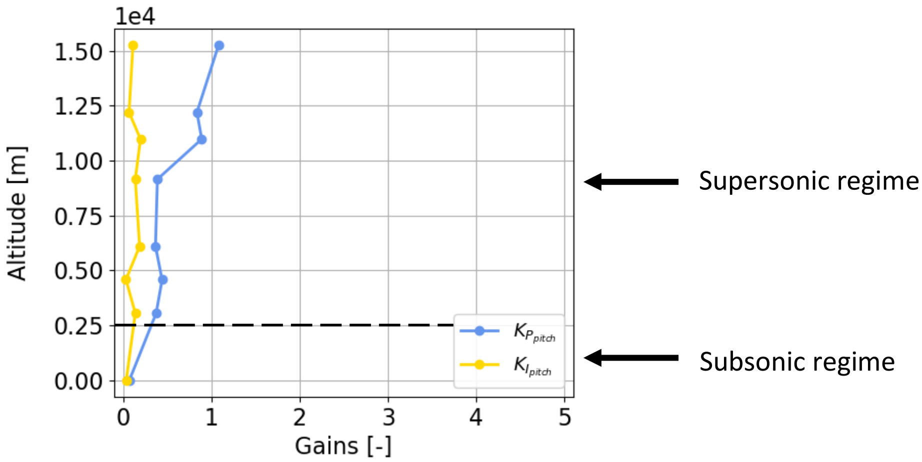

b) Cruise speed VC

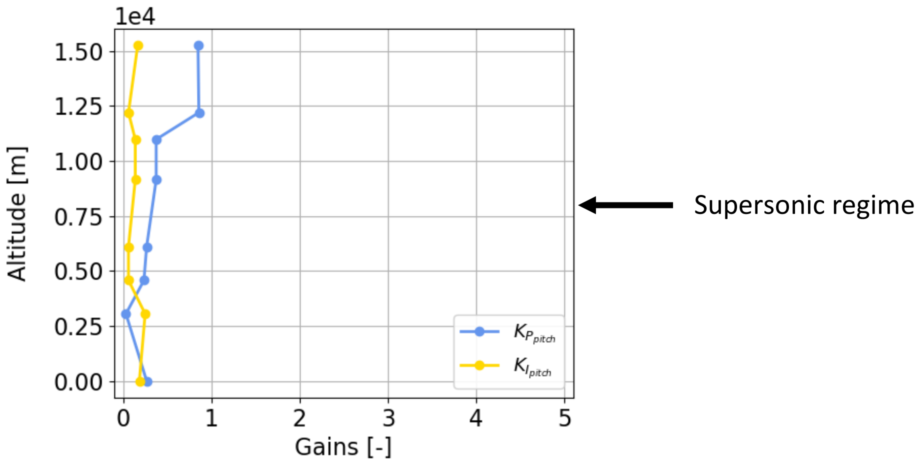

c) Dive speed VD

Figure 4.13: Derived gains for the pitch control

Actuator Control

To adjust the deflection rate $\dot{\eta}$ of the aircrafts' control surfaces, the commanded deflection u_η from the pitch controller is compared to the current elevator deflection $\eta_{measured}$, and the error is amplified by a gain in the proportional controller as presented in Figure 4.14. The resulting deflection rate $u_{\dot{\eta}}$ is subsequently mapped onto the horizontal tail plane.

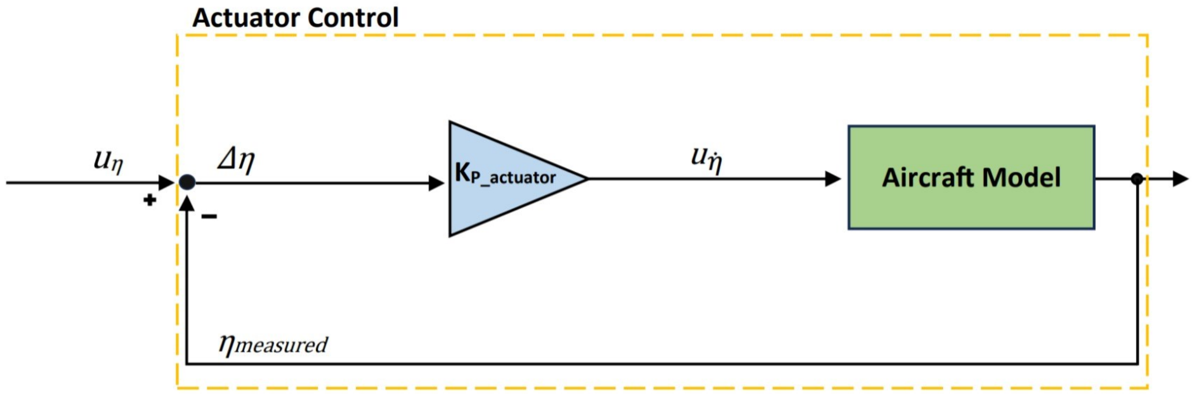

Figure 4.14: Control architecture for the outer actuator control loop

Figure 4.15 a) through c) displays the derived gains of the actuator control. This controller acts as a gain increasing the rate mapped onto the control surface proportionally with the magnitude of the required deflection by the pitch control. The proportional gains for velocity VA vary between 20-30, whereas the gains for velocities VC and VD remain more stable, moving between 10-20. There appears to be no apparent pattern between the unstable and stable states. It seems that the gain is adjusted in response to preceding gains from the outer loops, leading to inherited similar oscillatory behavior in the actuator gains.

On a side note: To evaluate the stability of the gains in relation to oscillatory behavior across the flight envelope, a gust impact using one gust gradient of 12.5 spatial chords is simulated to identify possible divergence of the closed-loop system. No divergence or instabilities were observed, and the controller delivers satisfying results.

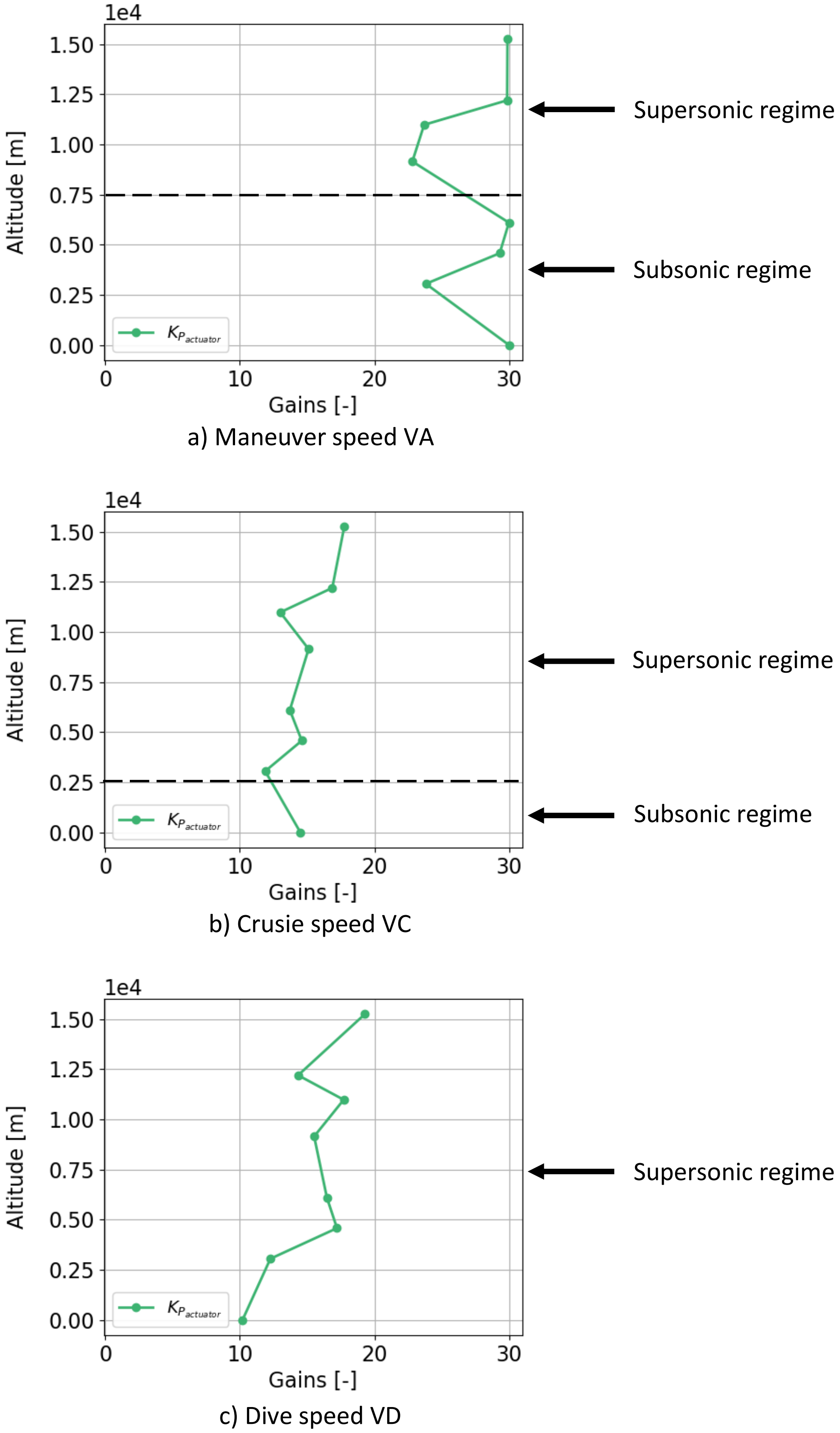

Figure 4.15: Derived gains for the actuator control

4.4. Intermediate Results of the Stability Augmentation System

To evaluate the function fitness of the genetic algorithm's derived gains, Figure 4.16 demonstrates the response of the closed-loop system's transfer function after 750 generations, subjected to a step input of either $N_z = 1.0g$ or $\theta = 5°$ after $t = 0.5s$ depending on the velocity (revert to Section 4.3 for the introduction of the corner point control). The resulting curve is then compared to the desired behavior. The figures illustrate the reference input for the subsonic unstable and supersonic stable configurations in terms of either the load factor N_z or pitch angle Θ.

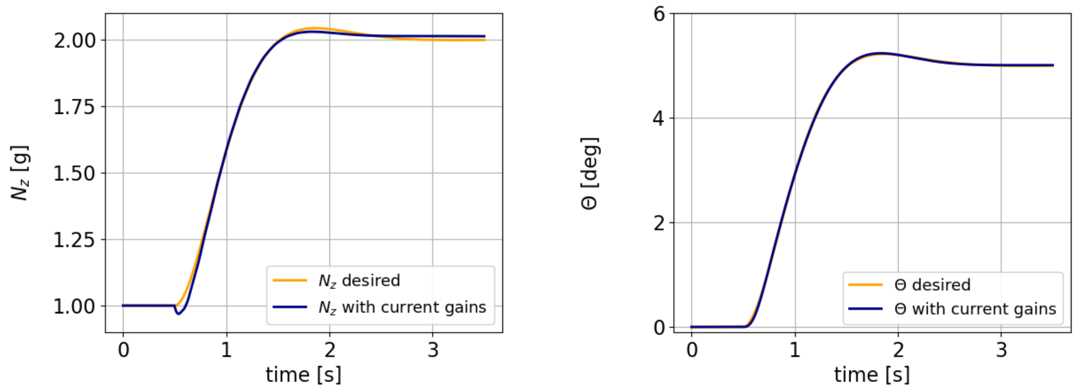

a) Transfer function of load factor N_z

b) Transfer function of pitch angle Θ

Figure 4.16: Transfer function of closed-loop system in the unstable subsonic regime after 750 generations

After 750 generations, comparing the desired and resulting curves of the transfer functions shows that neither of the two curves attain a saturation limit. The transfer function for the step input of the pitch angle, shown on the right-hand side, precisely follows the desired function. However, on the left-hand side the transfer function for the step input of the load factor fails to track the desired function in a similar manner. The load factor initially reverses in direction, temporarily dropping below the trim value before eventually increasing. When the elevator is deflected up to increase the pitch angle of the aircraft, there is a temporary loss of lift on the horizontal tailplane, resulting in a brief decrease in load factor before the aircraft attains the intended flight trajectory. Incorporating canards could possibly mitigate this issue, since they do not suffer the same loss of lift when executing a pitch up maneuver. Figure 4.17 shows the transfer functions of the closed loop system for the naturally stable flight state after 750 generations, exhibiting a significantly different behavior when tracking the target curve.

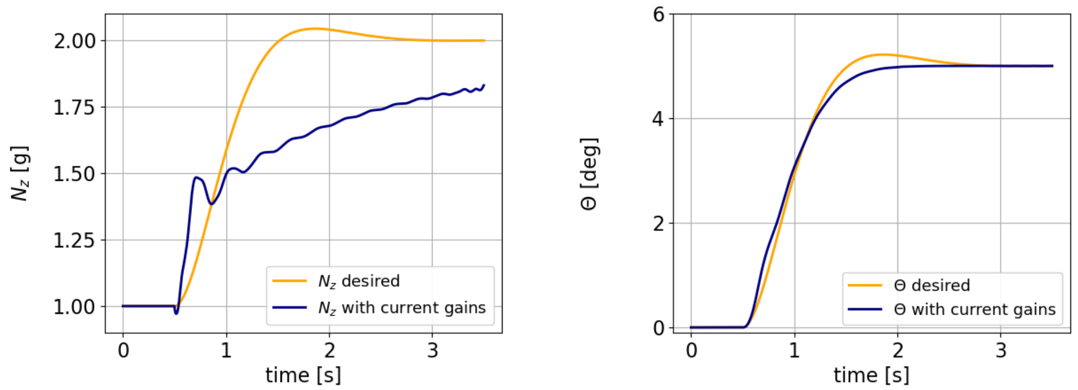

a) Transfer function of load factor N_z

b) Transfer function of pitch angle Θ

Figure 4.17: Transfer function of closed-loop system in the stable supersonic regime after 750 generations

In the supersonic stable regime, the algorithm has difficulty attaining matching characteristics for rise time and overshoot in comparison to the subsonic unstable configuration. Figure 4.17 b) demonstrates that when theta is used as the tracking variable, the algorithm struggles to produce the desired behavior, resulting in an overly damped curve. Figure 4.17 a) on the left-hand side depicts the resulting behavior when the load factor is utilized as the tracking variable. The actuators appear to reach a saturation limit around $N_z = 1.5$, followed by a gradual approach towards steady state accuracy after initial saturation. Subfigures a) and b) exhibit behavior resulting from the rate limit $\dot{\eta}_{max}$ imposed on the elevator, described in Chapter 3.7. The controller must counteract the increased stability and inertia in supersonic flight, requiring partial destabilization of the configuration. Increased control action is required to achieve greater deflection of the elevator; however, this leads the controller to reach a saturation limit, resulting in a strongly damped oscillation on the control surface until it reaches the steady state accuracy. Lower step inputs were evaluated, but the resulting model did not yield a higher fitness value for the cost function. As this rate saturation only appeared in the state space system simulation utilized for the control design and did not negatively affect the time simulations for the gust analysis, the initial step input was deemed adequate for this works gust load campaign and no further derivations to the control system were taken.

Figure 4.18 compares the closed-loop behavior to the open-loop behavior using the same operational points depicted in Figure 4.2. The simulation covers two flight states with seven bottom gust gradients between 9 to 107 meters and an inclination of 0°. Subfigures on the left-hand side show response for the unstable configuration at M4, MA05, FL000 while the Subfigures on the right-hand side show the stable configuration at M4, Ma12, FL360.

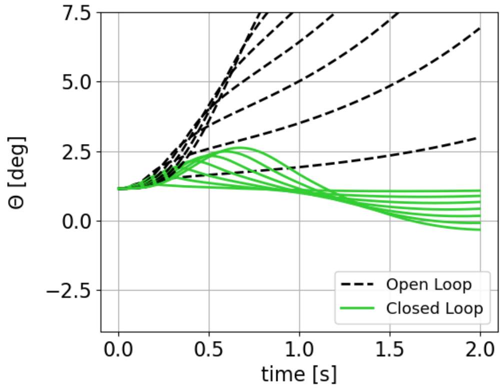

a) Pitch angle Θ, unstable configuration

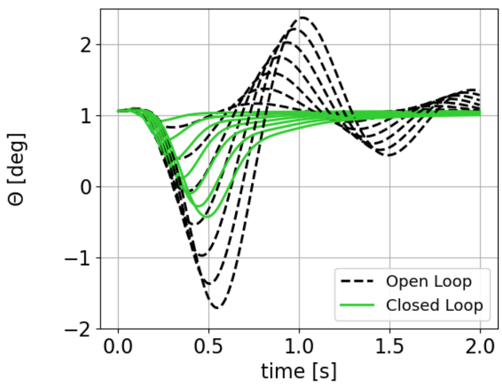

b) Pitch angle Θ, stable configuration

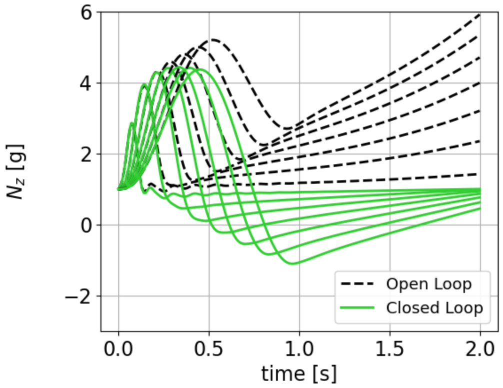

c) Load factor N_z, unstable configuration

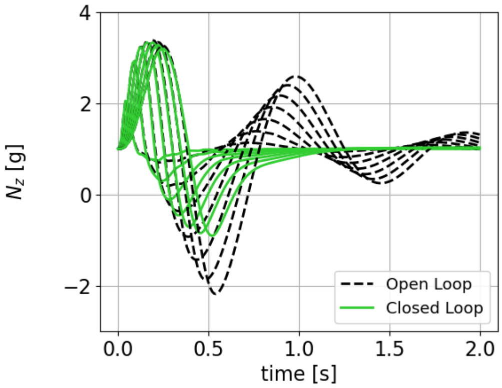

d) Load factor N_z, stable configuration

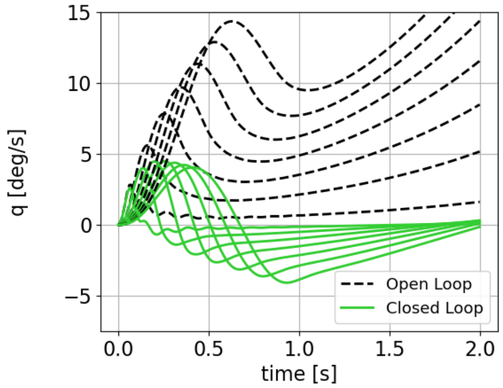

e) Pitch rate q, unstable configuration

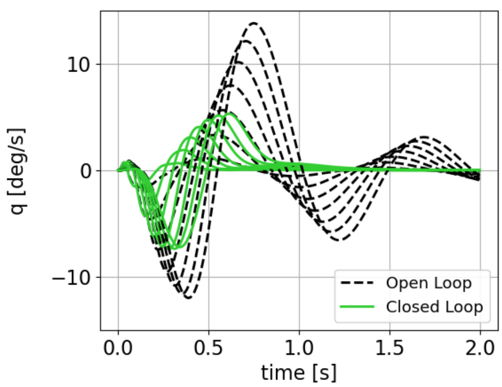

f) Pitch rate q, stable configuration

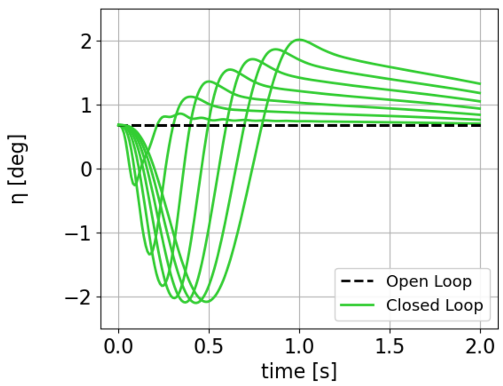

g) Elevator deflection η, unstable configuration

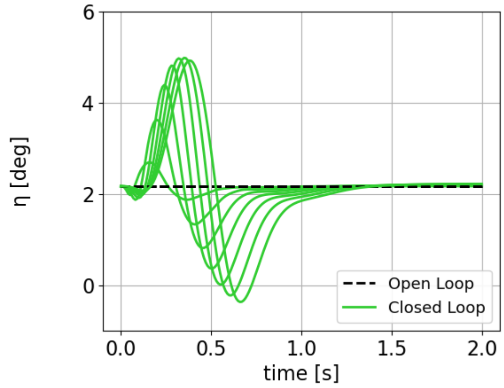

h) Elevator deflection η, stable configuration

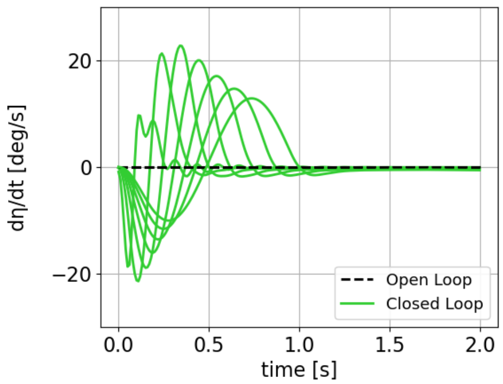

i) Elevator deflection rate $\dot{\eta}$, unstable configuration

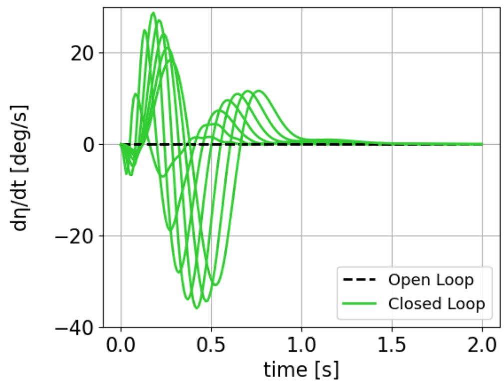

j) Elevator deflection rate $\dot{\eta}$, stable configuration

Figure 4.18: Comparison of the open loop and close loop responses for different gust impacts

Figure 4.18 a) through f) show that the unstable aircraft no longer diverges when in the closed-loop, and the reference states gradually return to their trim values. The stable configuration indicates that the impact of gusts and resulting oscillations are more efficiently damped in the closed-loop, and the states return to the initial trim condition in about one second after the onset of the gust impact. Figure 4.18 g) and h) show that only moderate deflection of the horizontal tail plane is needed to stabilize the aircraft. However, Figure 4.18 h) indicates the need for stronger control action in the stable configuration for reasons discussed in Section 4.3. Despite nearly three times higher maximum deflection in the stable configuration compared to unstable configuration, the deflections remain well below the limit of $\eta_{limit} = 20°$. Figure 4.18 i) and j) show the deflection rate mapped onto the elevator. Safety margins are essential during normal turbulence to maintain aircraft maneuverability in large turbulence and prevent frequent rate limit exceedance. The maximum deflection rate is approximately 40°/s, leaving a 50% margin of the rate limit $\dot{\eta}_{limit} = 80°/s$ for higher turbulence. During the gust load simulations, the actuator stayed below the imposed rate limits (see Section 3.7) at all times. This contrast to the rate limit exceedance visible in Figure 4.17 a) stems from the way incremental load factors (or pitch angles) are imposed on to the model in the gust load simulation. In the gust simulation, the increment of pitch angle due to the gust impact is imposed in small increments throughout the gust impact instead of an instantaneous change of the full resulting increment, which allows for the control system to react in appropriate time. While neither the control system nor the algorithm to the derive the gains exhibits optimal behavior, the resulting aircraft behavior is considered satisfactory for the objective of this work. Therefore, the control system is not further developed. In Figure 4.19, a comparison is presented between the load envelopes of the wing root bending moment and the wing root torsion moment for both operational points. Because of divergence, the open loop gust computations result in nonphysical loads that lead to scaling stress imposed on structure leading to structural failure after some point. As a result, peak loads always emerge at the end of the simulation period. Therefore, open-loop loads of the unstable configuration are omitted. Figure 4.19 a) illustrates the gust load envelope for the unstable configuration with a closed-loop system. The maximum positive wing root torsion loads in the closed-loop system occur at case 30245 and $t = 0.21s$, and the negative wing root torsion moments occur at case 30641 and $t = 0.21s$. This observation indicates that the aircraft is no longer diverging and allows for accurate gust load calculations, unlike the open-loop gust loads, which were not physical meaningful. When comparing the loads in Figure 4.19 b) for the open and closed-loop systems of the stable supersonic configuration, it is evident that the closed-loop system partially alleviates the loads on the wing. This results in a reduction of the wing root bending moments by approximately 10%. Although the decrease in loads is significant, it is important to note that the implemented control system is not intended to act as a Gust Load Alleviation (GLA) system, but rather to develop a SAS to enable physically meaningful gust computations. Consequently, the reduction in loads is a mere beneficial byproduct of the control system.

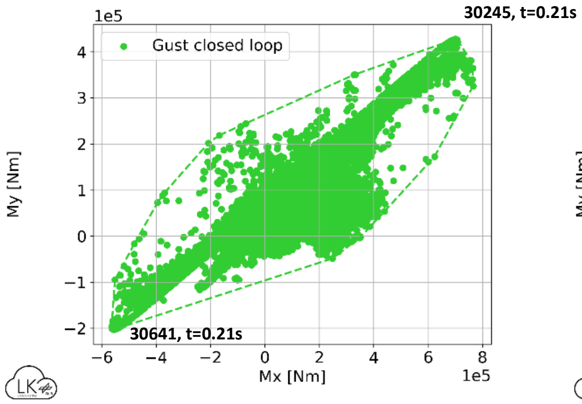

a) Subsonic regime

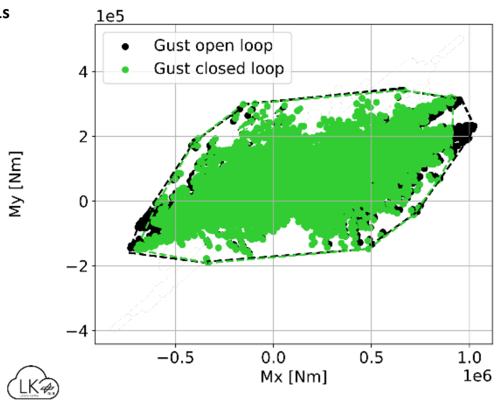

b) Supersonic regime

Figure 4.19: Loads acting on the wing root of the FFD, comparing open loop and closed loop loads

Figure 4.20 compares the attachment loads acting on the horizontal tail plane in open-loop and closed-loop configurations. The shear forces in the z direction on the elevator tripled due to the actuator action and larger control surface deflection, resulting in higher observed loads.

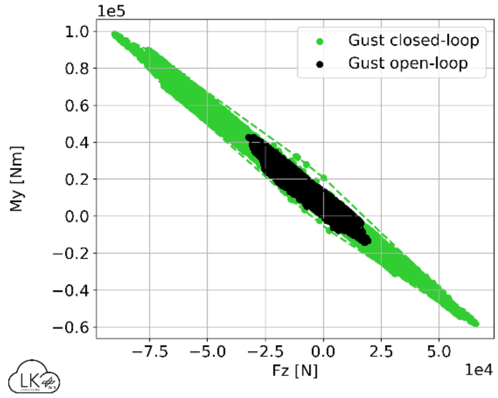

Figure 4.20: Loads acting on the horizontal tale plane of the FFD, comparing open-loop and closed-loop loads

5. Gust Load Analysis on the DLR-FFD Configuration

Based on the data gathered in the preceding chapters, a comprehensive gust load campaign will be carried out, evaluating the effects of the selected parameter range and discussing the resulting gust loads acting on the considered configuration. The gust loads, in particular bending moment M_x, torsion moment M_y and shear force F_z, are reviewed at the monitoring stations presented in Section 3.4, as they represent the main dimensioning quantities [44]. Often, dimensioning loads result from a combination of two quantities, so the typical approach to analyzing loads is to compare two-dimensional envelopes that represent for example a combination of the bending moment M_x and torsion moment M_y within shear-moment-torque (SMT) plots. The last part discusses the observed local accelerations at the monitoring stations. Although the load factor does not size the aircraft structure itself, it can offer helpful indications for peak loads and operational limitations.

5.1. Quasi-steady Gust Load Analysis

First, the Quasi-steady Pratt gust loads in accordance with Section 2.1.1 are simulated. As described in Section 3.6, the method provided in MIL-A-8861 will be selected to calculate the loads, incorporating the reference gust velocities given in CS23. Figure 5.1 depicts the resulting quasi-steady Pratt loads at three different sections on the right wing. Figure 5.1 a) illustrates the bending moment M_x against the torsion moment M_y at the wing root. The subsonic gust cases (blue) lead to peak loads of the wing torsion in the upper right corner, while the supersonic gust cases (green) result in peak loads of the wing bending in the center right. This shift in envelope between the two velocity regimes can be attributed to the movement of the aerodynamic center at higher speeds, as discussed in Section 4.1 and shown in Figure 1.1. Comparable characteristics can be observed for the mid and outer wing, albeit the loads are generally smaller compared to those at the wing root.

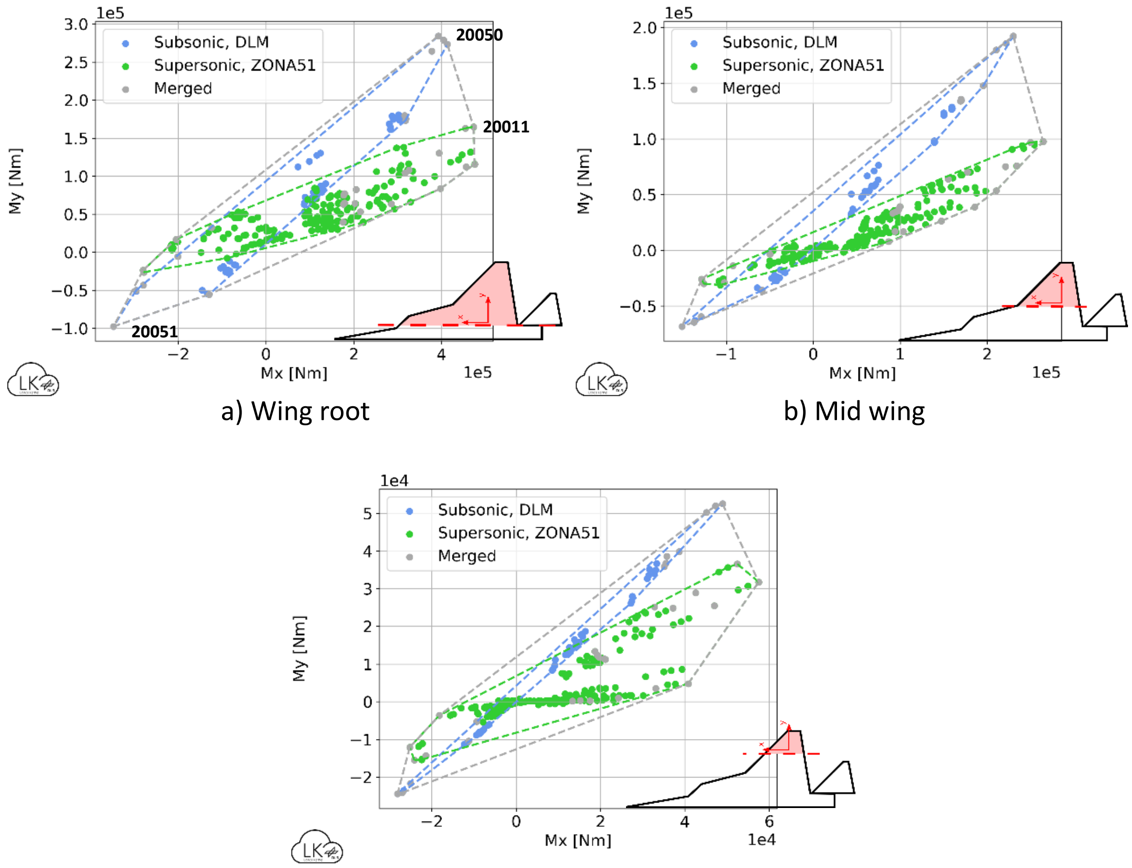

a) Wing root

b) Mid wing

c) Outer wing

Figure 5.1: Quasi-steady Pratt gust loads

Figure 5.1 a) also displays the cases generating the peak moments. The maximum bending moments occur at case 20011, mass case M1, and amount to $M_x \approx 4.8 \cdot 10^5\ Nm$, while the maximum torsion moments occur at case 20050, mass case M4, and amount to $M_y \approx 2.9 \cdot 10^5\ Nm$. Case 20051, a negative gust coming from the bottom and mass case M4, exhibits the peak negative loads for both bending and torsion moments on the wing. For the wing root, this load case provides a maximum negative bending moment of approximately $M_x \approx -3.5 \cdot 10^5\ Nm$ and a maximum negative torsion moment of approximately $M_y \approx -9.8 \cdot 10^4\ Nm$.

A more precise examination of the load cases reveals that all peak loads occur at velocity VC at sea level, except for the maximum peak bending moment which occurs at VC at flight level 150. This is due to the fact that the reference gust velocities for the Pratt method stay constant up until flight level 150, so this altitude represent a high velocity combined with the highest reference gust velocity. Concerning the load factor, these gust calculations demonstrate that the maximum acceleration does not necessarily correspond to the cases of highest moments. The peak wing root torsion moments correlate with the highest acceleration of $N_z \approx 4.7\ g$ arising at case 20050. In comparison, load case 20011 which is responsible for the peak wing root bending moments, only produces accelerations in the CG of around $N_z \approx 3.5\ g$.

5.2. Transient 1-cos Gust Load Analysis

As explained in 3.6, four different gust gradient sets, namely the “CS25 set”, the “Pratt set”, the “Long set” and the “Short set” are evaluated to determine which range of gradients produce the most significant loads for a combat aircraft such as the FFD. For a more detailed breakdown of the gust sets, refer to Table 3.5. The resulting loads of all four sets are visualized together in Figure 5.2. It is apparent that the gradients collected in the CS25 set result in the highest loads on the aircraft, the loads of the remaining gust gradient sets are within this load envelope. The “Pratt set”, which comprises a sole gust gradient of 12.5 spatial chords like the one used in the quasi-steady Pratt method, closely approximates the peak loads of the CS25 set. Pratt's reasoning for using a gust gradient of 12.5 spatial chords, discussed in Section 2.1.1, appears to hold true for this configuration. Similarly, the “Long set” of gust gradients approximates peak loads but does not exceed those of the CS25 nor the Pratt set. The set's peak loads occur around 0.5 seconds, indicating that the 2-second simulation time is adequate, even for the longest gust gradients. In contrast to the other sets, the “Short set” appears to generate lower loads, with a rather round-shaped envelope.

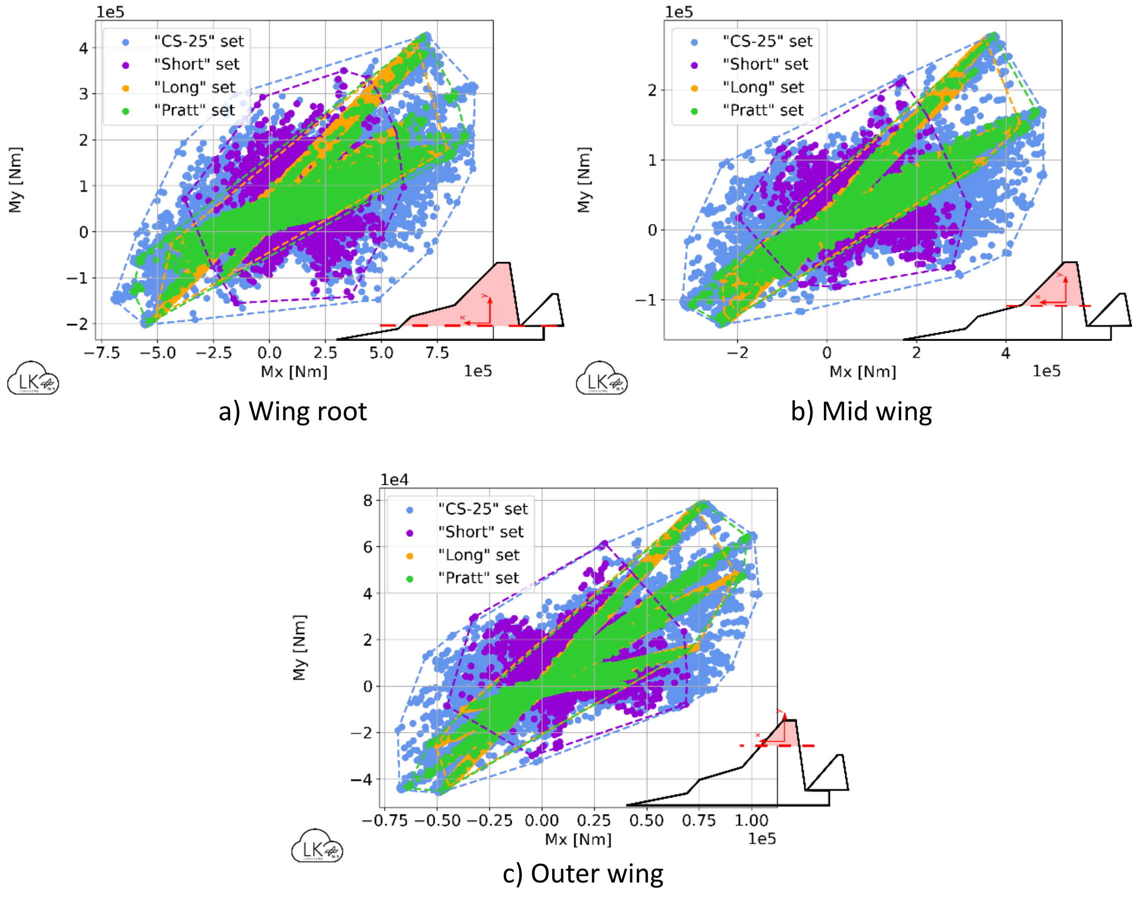

Figure 5.2: Comparison of different gust gradient sets for the transient 1-cos gust analysis

It is concluded that the gust gradients necessary for the CS25 type certification can be deemed adequate for supersonic combat configurations similar to the FFD. Gusts outside the range of $H = 9 - 107\ m$, both shorter and longer, do not appear to cause higher loads. The CS-25 set displays positive peak loads of $M_x \approx 9.18 \cdot 10^5\ Nm$ and $M_y \approx 4.27 \cdot 10^5\ Nm$, while the Pratt set exhibits positive peak loads of $M_x \approx 8.78 \cdot 10^5\ Nm$ and $M_y \approx 4.24 \cdot 10^5\ Nm$. When computational power is limited, a first estimate of peak loads could be obtained by sole simulation of the Pratt gradient of 12.5 spatial chords. Although this will not provide the exact loads, it results in an error of only 4.4% for the wing root bending moment and an even smaller error of 0.7% for the wing root torsion moment.
Figure 5.3 displays the complete envelope of gust loads acquired from all four gust gradient sets, for both the subsonic regime (blue) and the supersonic regime (green). The resulting envelope for both velocity regimes is indicated in black, with the sparse number of black dots denoting only the peak load snapshots of each monitoring station. It is apparent that, albeit they have different orders of magnitude, the transient 1-cos gust exhibits the same general characteristics regarding the shape of the envelope and the correlation of peak torsion loads with the peak acceleration as the gust loads of the quasi-steady Pratt method.

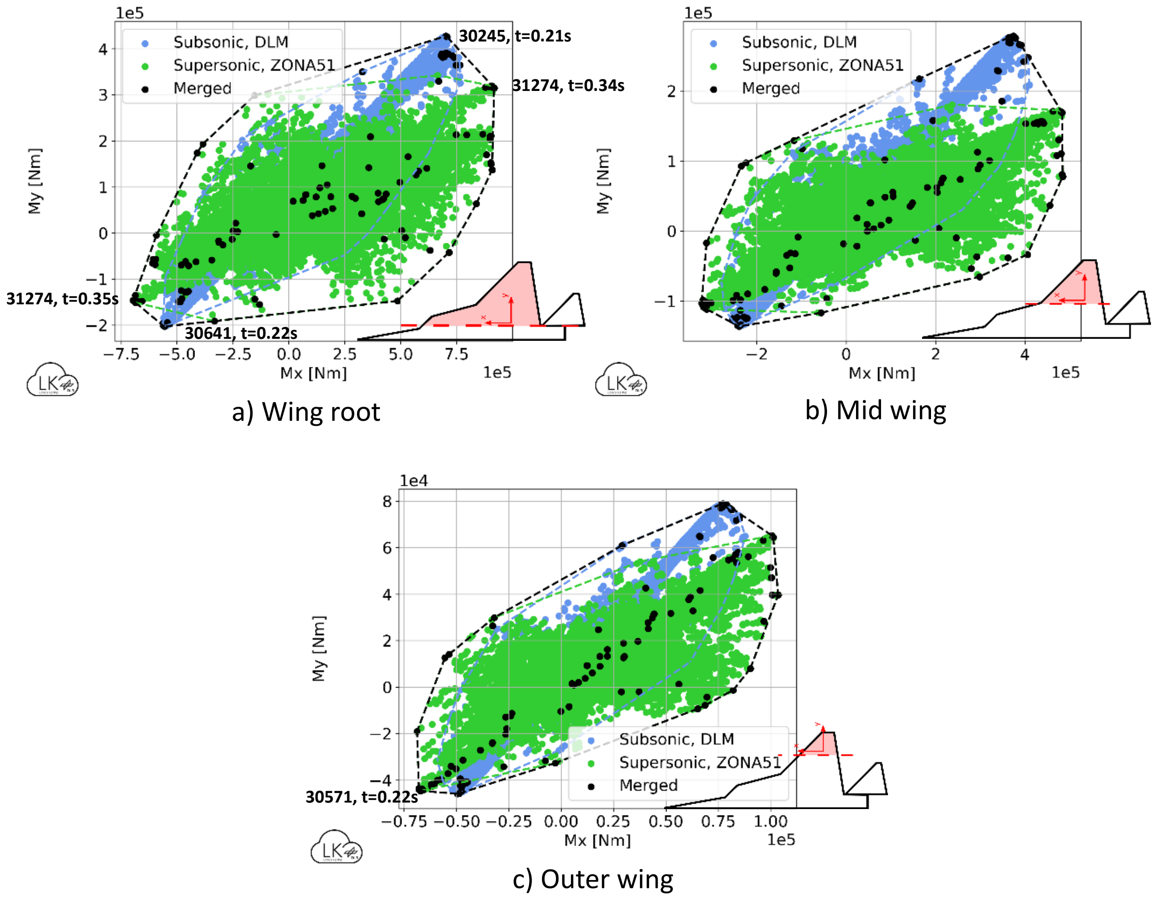

a) Wing root

b) Mid wing

c) Outer wing

Figure 5.3: Transient 1-cos gust loads

At the wing root, the maximum torsion moments occur at the subsonic cases 30245 and 30641, both at mass case M4 at sea level, with a gust gradient of $H = 67\ m$, and velocity VC, with $M_y \approx 4.3 \cdot 10^5\ Nm$ and $M_y \approx -2.0 \cdot 10^5\ Nm$ respectively. The peak bending moments appear at the supersonic cases 31274 and 30438, both at mass case M4 at sea level, gust gradient of $H = 57\ m$ and velocity VD, with values of $M_x \approx 9.2 \cdot 10^5\ Nm$ and $M_x \approx -7.0 \cdot 10^5\ Nm$ respectively. The gust base frequency for cases 30245 and 31274 can be calculated with Equation (2.12) accordingly to $f_{gust_{30245}} \approx 4.9\ Hz$ and $f_{gust_{31274}} \approx 6.6\ Hz$. These frequencies closely align with the first eigenmodes of the FFD, which can be viewed in Section 3.4. Since the frequencies are nearly identical, they excite the eigenmodes and cause peak loads for both wing bending and torsion. Case 30571 in Figure 5.3 c) is the only case wherein a gust gradient $H > 67\ m$ results in the highest loads. This larger gust gradient appears to result in greater negative loads closer to the wingtips compared to the other gust gradients. Looking at the timestamps, it can be observed that the subsonic peak loads occur around 0.2 seconds after the initial gust impact, while the supersonic loads peak after roughly 0.35 seconds.

Figure 5.4 compares the quasi-steady Pratt loads (in green) with the transient 1-cos gust loads (in blue) and the 1g level flight loads (in yellow).

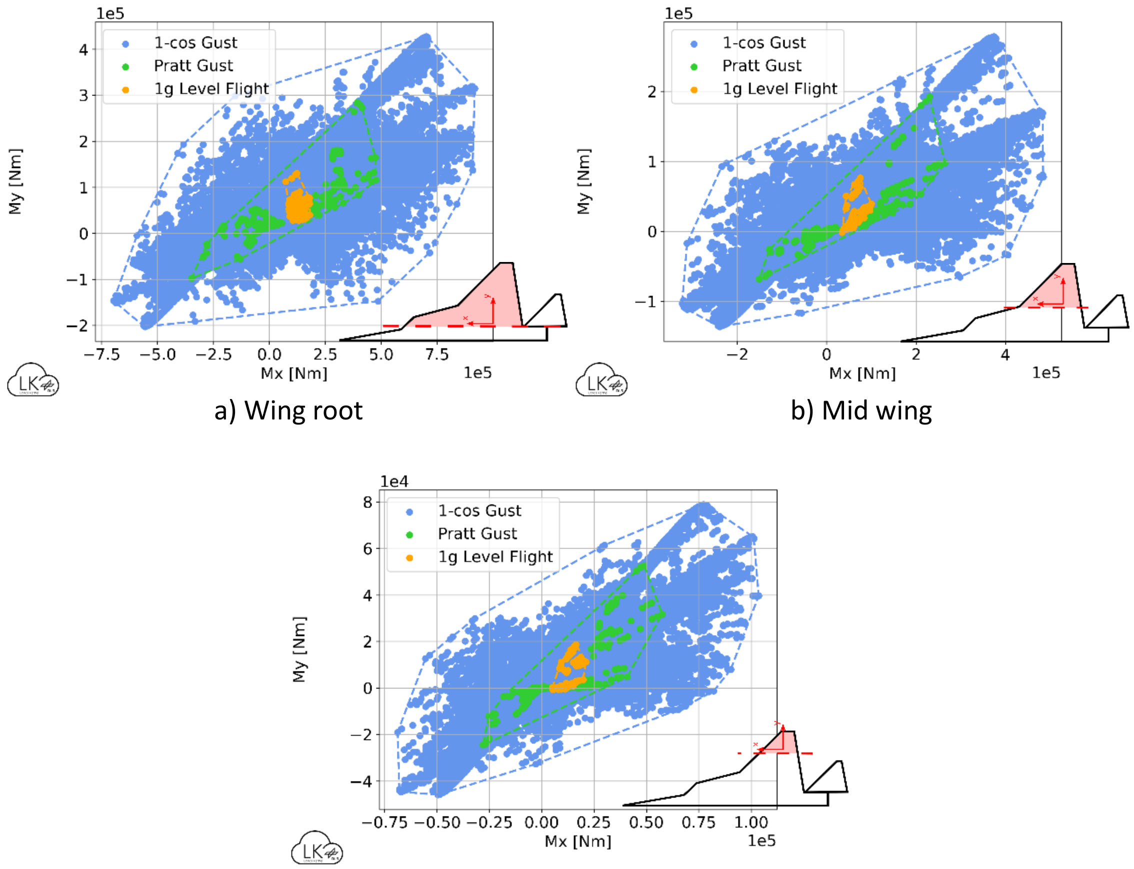

a) Wing root

b) Mid wing

c) Outer wing

Figure 5.4: Comparison of quasi-steady Pratt gust loads and transient 1-cos gust loads

It is evident that the Pratt loads do not correspond with the 1-cos loads, neither with respect to the bending nor the torsional moment. More precisely, the Pratt loads are approximately half in magnitude at all monitoring stations compared to the 1-cos gust loads. Additionally, the cases that produce peak loads do not share the same flight states. For instance, case 20011 with flight state VC, M1, FL150 generates the positive peak bending moment at the wing root according to the Pratt method, whereas case 31274 with flight state VD, M4, FL000 generates the peak load for the 1-cos gust.

This discrepancy can be traced to several observations. On one hand, this could include the combination of transient aerodynamic behavior and penetration effects during the time simulation in the transient method. Additionally, the accuracy may be impacted by different assumptions made in both methods. The Pratt method assumes a rigid aircraft performing only heave motion, whereas the FFD shows a strong pitch motion. Therefore, the 1-cos gust method, which considers an elastic aircraft in combination with flight mechanical motion, better represents the configuration and thus better depicts the acting loads. On the other hand, several aspects discussed in Section 3.6 suggest that the transient analysis in this investigation may be rather conservative.

For instance, the FPA factor discussed in Section 3.6 was selected to $F_g = 1.0$, resulting in significantly higher reference gust velocities compared to those observed on civil configurations for which this formula was originally formulated. By selecting the FPA factor according to CS25, higher altitudes would consequently carry even greater significance in the load analysis. At the same time, it must be noted that the factor was deliberately chosen to $F_g = 1.0$ in consideration of the aircraft's characteristics and mission profile (refer to the discussion in Section 3.6). Even with a 20% reduction in gust velocities (refer to Figure 3.18 for the reduction resulting from the flight profile alleviation factor according to CS25), the Pratt gust loads would still remain less conservative than the transient 1-cos gust loads.

Additionally, the reference gust velocities may be overly cautious for military combat aircraft. As outlined in Section 3.6, they are probabilistic values selected for a service life that is ten times greater than that of a combat aircraft. Therefore, the possibility of encountering the utmost gust impact on the considered configuration is rather unlikely.

5.3. Comparison to Maneuver Loads

Comparing gust loads to the Maneuver loads, Figure 5.5 illustrates that gust loads, including transient gust loads, are significantly smaller than the maneuver loads, approximately half in size.

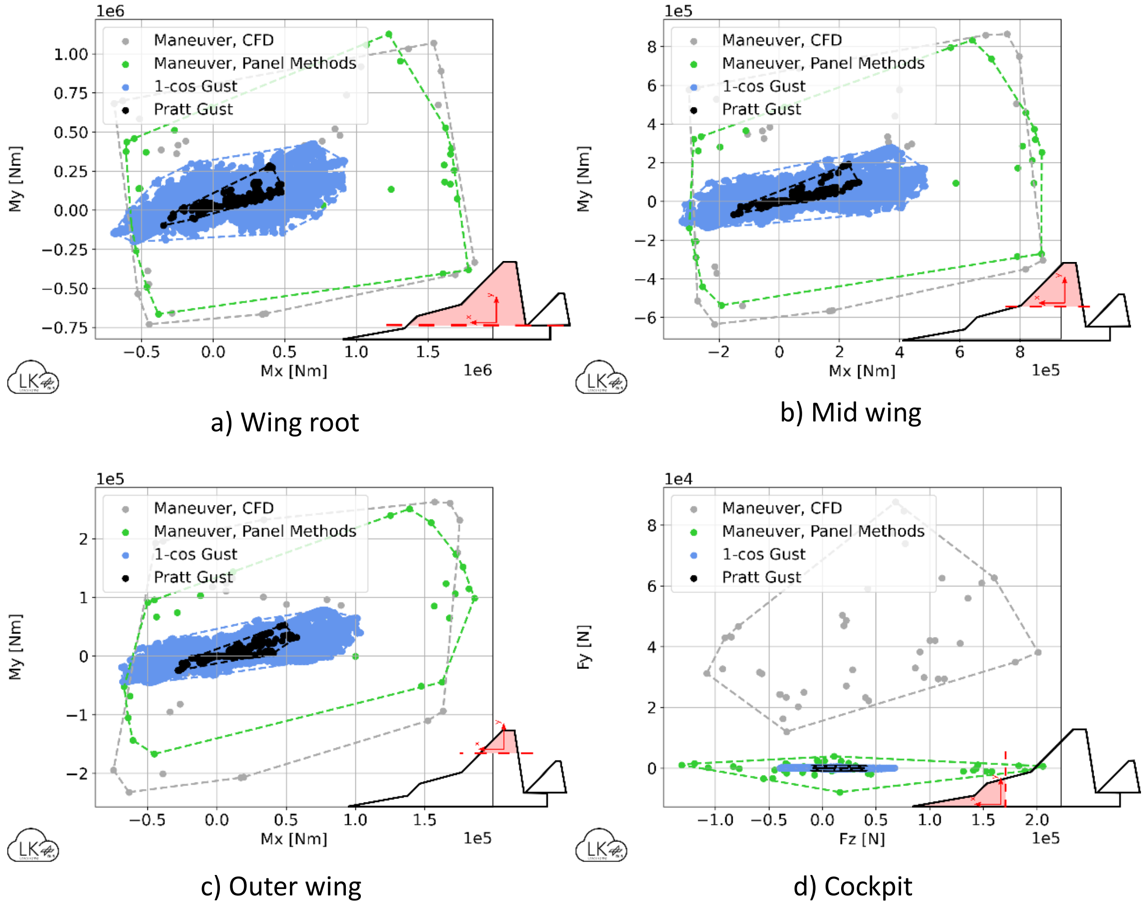

Figure 5.5: Comparison of maneuver loads and gust loads

The significantly higher maneuver loads can be observed at all four monitoring stations presented in SubFigure 5.5 a) to d). At the same time, Subfigures a) to c) demonstrate on the left-hand side that transient 1-cos gusts do indeed produce higher negative wing bending loads than maneuvers, as the excitation of the wing bending modes by the gust impact leads to some degree of oscillatory behavior on the wing. Gusts exhibit symmetry around the 1g level flight. However, maneuvers lack this symmetry as they can range from $N_z = -3 \ldots + 9\ g$. The loads envelope shifts to the right due to the asymmetry in load factors, resulting in greater loads from gusts in the negative plane as the load factor reaches up to $N_z = -5.36$. Although the loads are only a third of the observed positive wing bending loads, their effect on aircraft structure must be taken into account for design and material selection, for example when the lower skin of an aircraft wing is made of alloys with lower tensile strength. If this is not the case, only a rough estimate of the gust loads appears sufficient for sizing of the combat aircraft. These findings support the outcomes of the literature review in Chapter 2, which indicate that gust loads generally have a relatively minor impact on the sizing of the structure for supersonic combat aircraft.

5.4. Accelerations due to Gust Impact

As stated in the previous section, evaluations of different gradient sets indicate that small gust gradients do not result in the high loads on the aircraft structure. However, several publications have reported that short gust gradients may induce high acceleration on certain parts of the aircraft. Therefore, the following section will assess the accelerations at various locations within the aircraft. Figure 5.6 through Figure 5.9 depict the calculated acceleration at five distinct monitoring points throughout the aircraft. For each monitoring point, all gust simulations for the considered gust gradient and gust direction are evaluated and the load case with the maximum/minimum acceleration is extracted and plotted in blue/red. Note that this means that the two curves may belong to completely different load cases within the load envelope. To serve as reference, each acceleration is compared to the acceleration at the center of gravity in gray color.

Figure 5.6 presents the accelerations observed at a bottom gust impact with a gradient of $H = 9\ m$. It can be observed that the cockpit accelerations in the first panel match with those at the center of gravity and peak at around $N_z = 3.3\ g$. Looking at the wing root, the curve starts to oscillate, and accelerations rise to $N_z = 7.9\ g$. For the wing center, a decline in accelerations prior to a rapid increase at the outer wing can be noticed, where the accelerations peaks to about $N_z = -100\ g$ on the wingtip, with the negative values surpassing the positive peak. This high acceleration on the wing tip could stem from the short gust gradients exciting the aircraft structure as the frequency of the gust coincides with an eigenmode of the configuration. The first symmetric wing bending mode of the fourth mass configuration M4 occurs at the frequency of $f \approx 17.53\ Hz$, while the primary frequency of the wing tip acceleration is identified as approximately $f \approx 17.24\ Hz$. This indicates that the short gust gradient is exciting the FFD's first symmetrical wing bending mode, causing the wingtips to oscillate with high acceleration.

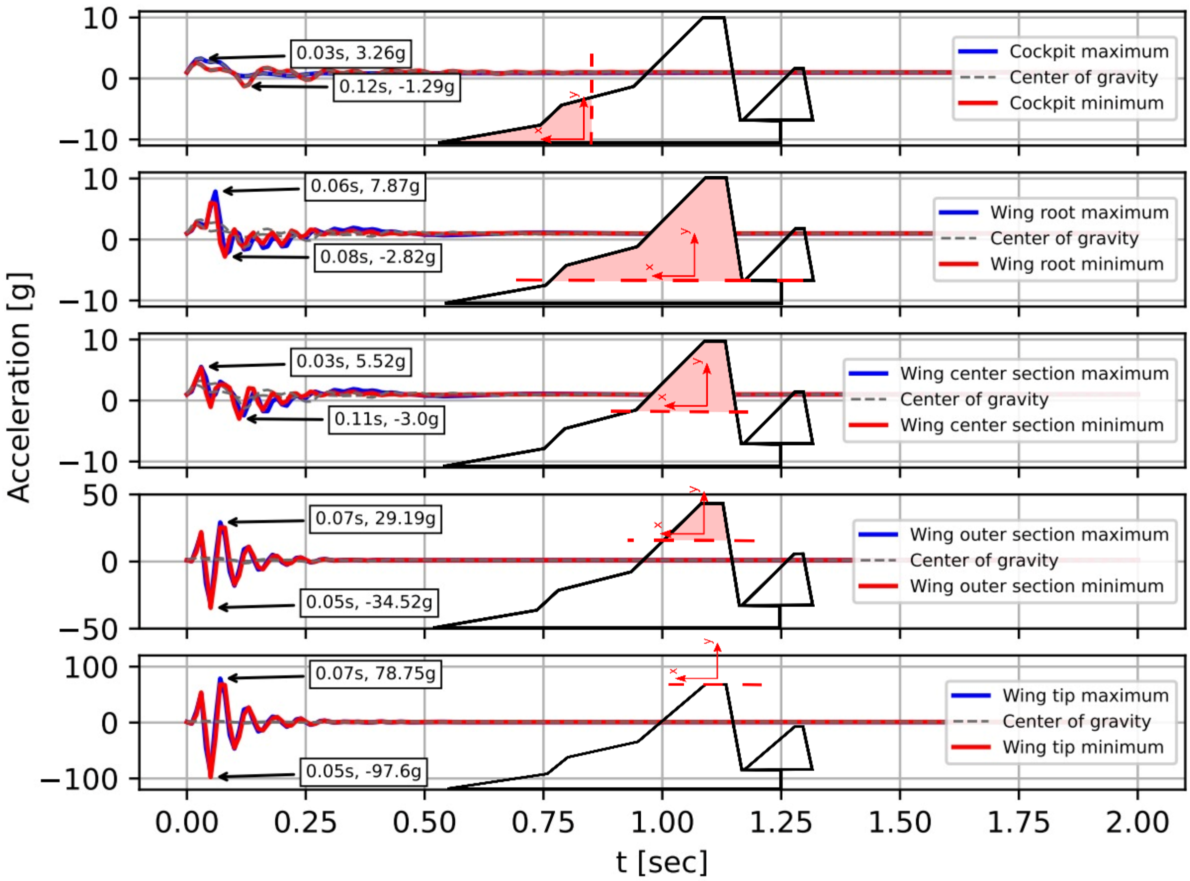

Figure 5.6: Accelerations at various sections of the aircraft, gust with $H = 9\ m$ and 0° inclination

Figure 5.7 displays the accelerations at a vertical gust with a gradient of $H = 56\ m$, which is inducing the peak wing root bending moments at the 1-cos gust load simulation. For this gust, the acceleration at the center of gravity appears to be higher, reaching about $N_z = 7.3\ g$. The accelerations differ marginally throughout the wing but remain roughly at the same magnitude. Additionally, only the wing tip displays fast oscillations induced by the gust.

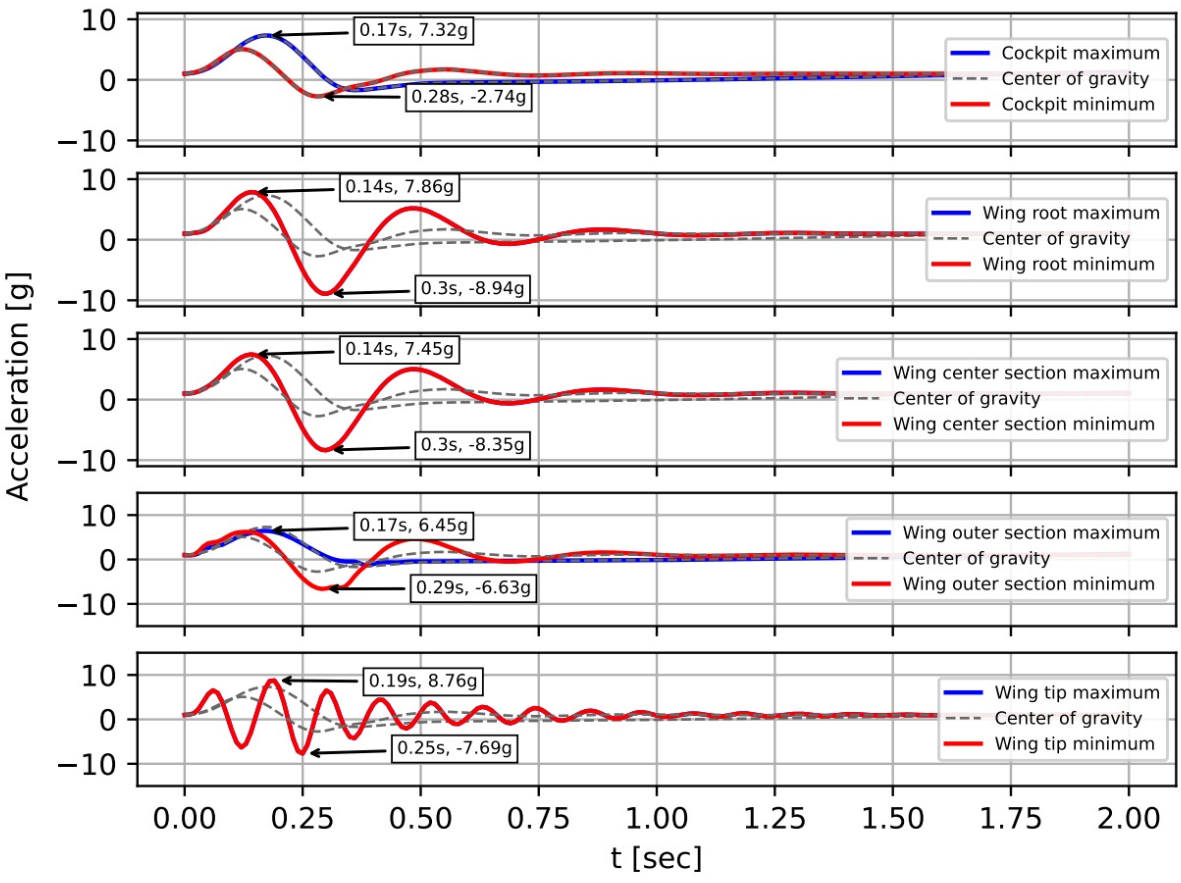

Figure 5.7: Accelerations at various sections of the aircraft, gust with $H = 56\ m$ and $0°$ inclination

Figure 5.8 displays the accelerations at a gust gradient of $H = 56\ m$ at an inclination of 180°. Panel one, exhibiting the acceleration at the cockpit, shows a negative peak acceleration of $N_z = -5.3\ g$, thus effectively surpassing the designated design load factor range of $N_z = -3 \ldots +9\ g$. Consequently, this model would not be tenable to fulfill the required certification factors and would impose challenges for the pilot and payload attachments. Additionally, if the acceleration at panel five is considered, it is visible that the top gust of inclination 180° in Figure 5.8 generates a higher positive acceleration than the bottom gust impact with an inclination of 0° in Figure 5.7, which can be attributed to the oscillations and the resulting overshoot.

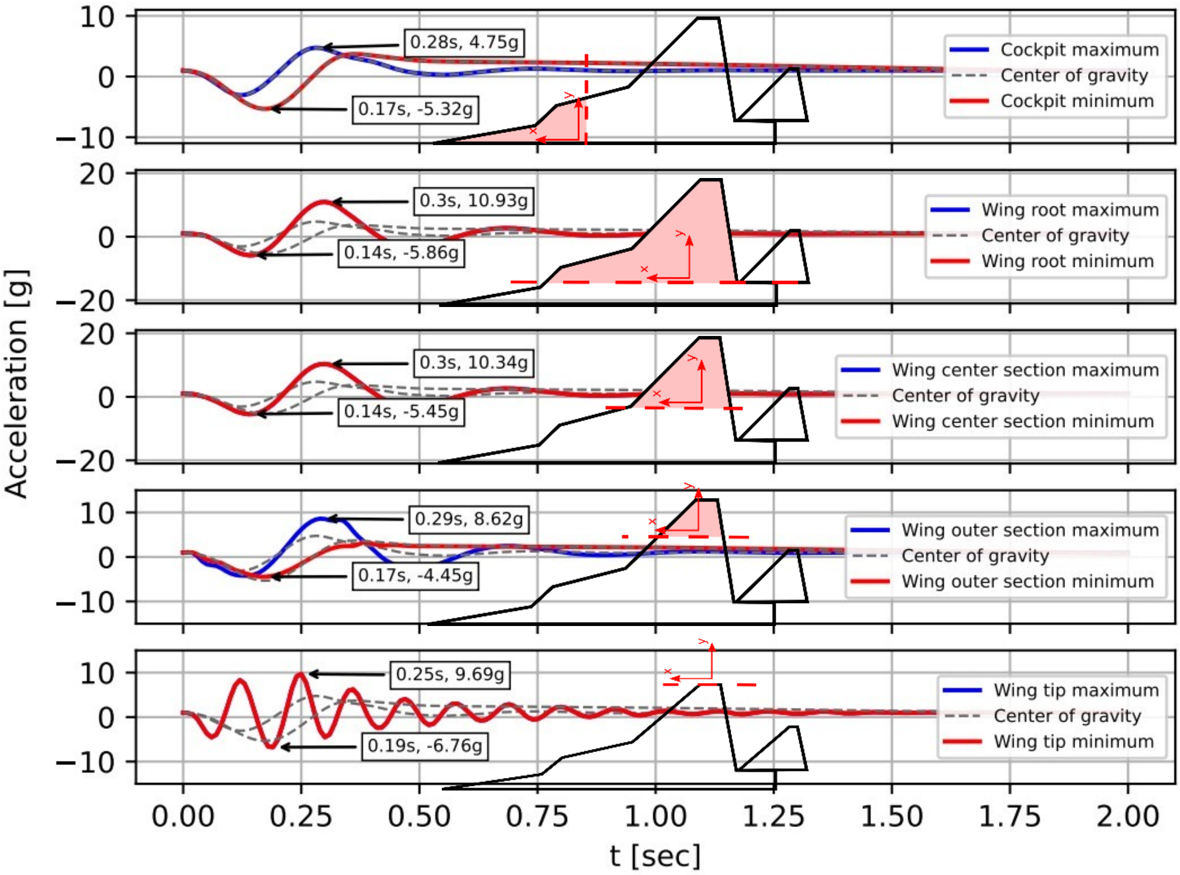

Figure 5.8: Accelerations at various sections of the aircraft, gust with $H = 56\ m$ and 180° inclination

Figure 5.9 presents the accelerations at a gust gradient of $H = 107\ m$ with an inclination of 0°. Panel one shows that both positive and negative peak accelerations curves align. The gust impact at the center of gravity appears highly damped, with only the impact imposed by the gust apparent before the acceleration returns to the 1g level flight after a short period. The highest acceleration at this gust impact is observed at the center of gravity, reaching approximately $N_z = 7\ g$ and therefore staying beneath the acceleration experienced during the 56 m gust. Although the gust has a gradient twice as large, the accelerations stay approximately the same as the shorter gust. Furthermore, the acceleration steadily decreases with greater distance from the center of gravity until they reach a minimum at the wing tips, with no rapid oscillations visible at either point of the wing.
The large gradients appear to excite different modes than the shorter gradients, for which the oscillations cease to appear. In the case of long gust gradients, the gust impact occurs gradually, and the aircraft's flight dynamics behave quasi-rigid, resulting in the center of gravity experiencing the highest accelerations instead of the wings.

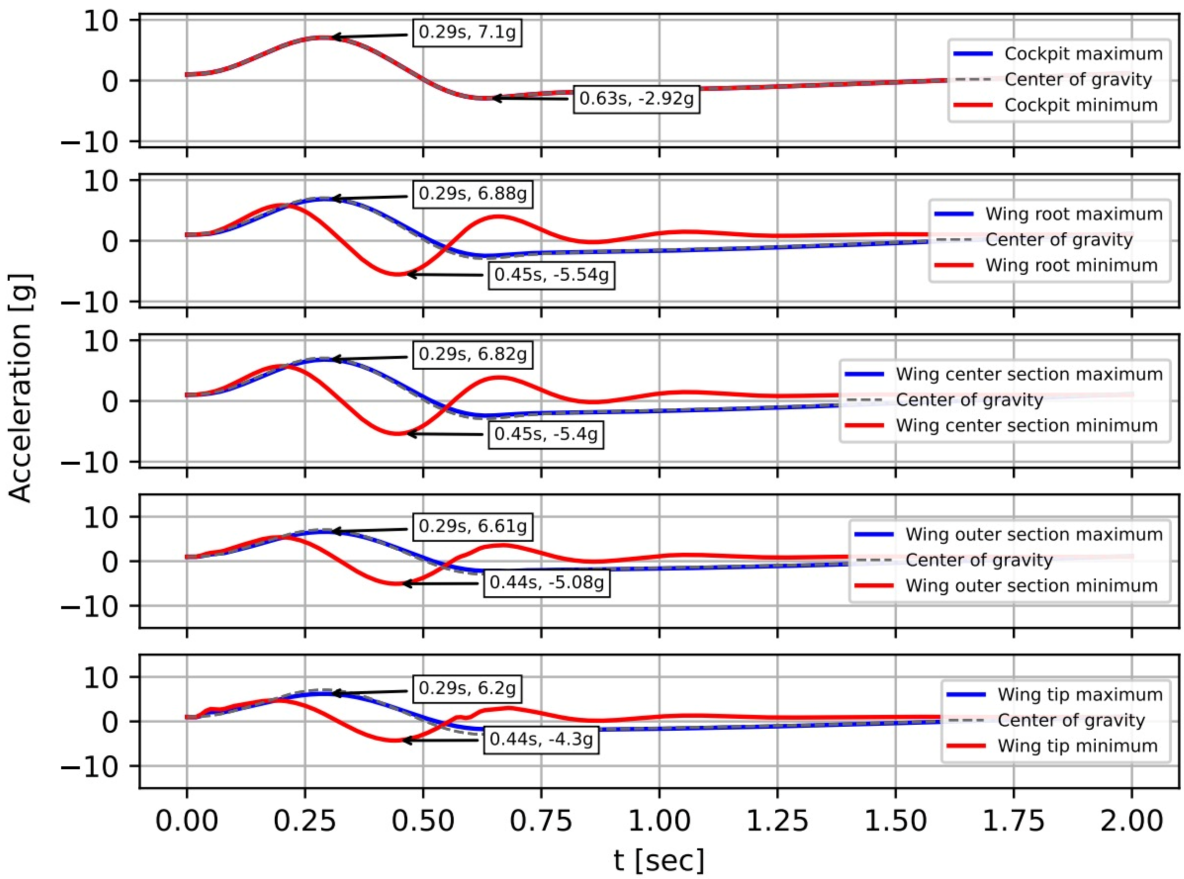

Figure 5.9: Accelerations at various sections of the aircraft, gust with $H = 107\ m$ and 0° inclination

Contrary to common misconception, not the acceleration but the section loads on the aircraft are sizing factors for the structure. As discussed in Section 5.2, the maximum of these two quantities do not always correlate. Still, the large accelerations lead to implications for two properties concerning the operational deployment of the aircraft:

Payload and Pilot limits.

The high positive and negative accelerations observed at the wingtips mean that mounting payloads at these points would be unfeasible. Hence, both the bearing and payload would need to be sized accordingly to withstand these high accelerations. Although attaching payloads to the wings would have a load alleviation effect and the acceleration would decrease, the resulting acceleration would still be of significant magnitude. This could be an explanation for why supersonic delta configurations similar to the FFD, such as the F-22 Raptor or the F-35 Lightning II, do not display hardpoints around the wingtips to mount payloads in these areas, neither in stealth nor in non-stealth combat configurations [62]. Although the acceleration may not directly impact the structural sizing, it does affect an essential component of the aircraft system: the pilot. As humans can bear a maximum acceleration of $N_{z_{pilot\ limit}} = 9\ g$ before losing consciousness, the accelerations experienced in the cockpit could thus bear restrictions for the operating range in turbulent air. As the vertical load factor attained by turbulent air and pilot maneuvers are cumulative, the allowed limit maneuver load factor needs to be constrained for each altitude depending on the possible gust loads. Equation (5.1) visualizes the limit load factor scheme.

$$N_{z_{pilot\ limit}} - \Delta N_{z_{gust}} = N_{z_{maneuver\ margin}} \tag{5.1}$$

For example, as observed in Figure 5.7 Panel 1, the peak horizontal acceleration at sea level can be extracted to $\Delta N_{z_{gust}} = 6.3\ g$. Therefore, the pilot would be restricted to attain a maximum maneuver load factor of only $N_{z\ maneuver\ margin} = 2.7\ g$ when flying through turbulent air to assure acceptable boundaries on the load factor. These limits may be adjusted based on factors such as the likelihood of the gust impact, flight patterns and other variables.

6. Conclusion and Outlook

This work featured a comprehensive investigation into the assumptions made during gust load analysis and provided a large-scale gust load campaign to investigate the effects of selected assumptions and methods on the resulting gust loads.

6.1. Conclusion

The investigation concludes that a comprehensive gust load campaign requires diligent selection of factors according to aircraft type, mission profile, and operational requirements. Only by selecting the right assumptions, a realistic gust load simulation can be obtained.

A stability augmentation system was developed for the FFD. Investigating various methods for deriving the gains of the control system showed that classic two degree of freedom models are inadequate to capture the unstable heave behavior of modern combat aircraft. Consequently, an optimization approach employing a genetic algorithm was chosen which yielded satisfactory outcomes for this study's objective. The control system demonstrated the ability to effectively handle the worst-case gust encounter within the control surface rate limit of current generation fighter jets.

A diverse range of gust gradients was tested for the transient 1-cos gust simulation. The range of gust gradients required for gust analysis in CS-25 was deemed satisfactory in capturing the peak cutting forces for supersonic combat configurations. Furthermore, it was observed that a gust gradient of 12.5 spatial chord lengths resulted in loads near maximum peak forces. As a result, it can be concluded that peak loads can be estimated with less than a 5% margin of error by using this gust gradient when minimal computation power is required. Although short gust gradients of $H < 10\ m$ may not result in large cutting forces, they result in considerable accelerations on the wing tips. The investigation found that, during gust impact with short gradients, the wingtips experienced a vertical load factor of up to $N_z \approx 100\ g$. Although payload mounted on the wings might decrease some of the accelerations, the local loads could still be significant, thus necessitating suitable sizing of both the payload and attachment points. Interestingly, cases demonstrating the peak load factor also exhibit the peak torsion moment, whereas the peak bending moment arises at lower load factors.

Characterized by the motion of the aerodynamic center as Mach numbers increase, subsonic gust cases result in peak torsion moments, while supersonic gust cases result in peak bending moments. The use of supersonic panel methods, including ZONA51, produces gust envelopes with similar properties to maneuver load envelopes obtained by supersonic CFD solutions. Only when the shear forces are monitored, the panel methods and CFD solutions show large discrepancies as shear forces are, contrary to the CFD solution, not considered. In addition, the order of magnitude and characteristics of supersonic loads appear to be plausible when compared to subsonic panel methods, given the underlying assumptions are defined accurately. Therefore, simulations conducted with supersonic panel methods can effectively depict the characteristics of gust loads in the supersonic regime.

Comparing different methods for gust load computations, it can be concluded for a supersonic combat configuration like the FFD that transient gust analysis should be preferred for simulating gust loads as the quasi-steady Pratt gust loads do not provide conservative results. The Pratt loads miss the positive

peak bending moment by approximately 90%. Upon comparing gust loads to maneuver loads, it is evident that the envelope of the positive gust loads is significantly smaller throughout every monitoring station of the aircraft. At the same time, the negative bending moments at all monitoring stations are greater than those of the maneuver loads. This could be due to the asymmetry of the maneuver loads between -3g and 9g, which is in contrast to the gust loads that are symmetrical to the 1g straight level flight. While the magnitude of negative loads is smaller than that of positive loads, they can still affect the sizing of the lower wing skin if different materials with lower tensile strengths are employed.
If the accelerations resulting from gust impact are monitored throughout the aircraft, it becomes clear that the acceleration at the center of gravity for a gust impact of $H = 56\ m$ exceeds the initial estimate, reaching about $N_z \approx 7\ g$ for the peak gust impact. Additionally, the negative vertical load exceeds the limit of $N_z \approx -3\ g$ for a peak gust impact, suggesting a reevaluation of the limits a human pilot can endure. Therefore, it may be necessary to limit the acceptable maneuver load factor for each flight condition to avoid exceeding the structural or pilot limit when flying through turbulent air.

6.2. Outlook

Future work may specifically focus on deriving precise assumptions and therein alleviation factors for combat aircraft based on their mission profile and service life, to incorporate into the current gust load formulas. However, military specifications do not currently support considerations such as a flight profile alleviation factor for military aircraft or a service life alleviation factor for gust velocities due to gust loads not being previously recognized as a dimensioning factor. Contrary to this, the results of this study indicate that gusts can generate significant loads on military combat aircraft.
Further investigation should also include the payload on the wings to estimate whether the acceleration experienced at the wingtip are still of significant magnitude. An additional mass configuration with payload masses located on the wingtips would allow to study the influence of the mass on the acceleration levels. Data collection from real aircraft and analysis can provide better insight into the load relief impacts and potential solutions.
As for the control system, the expansion of the control system to incorporate additional features such as lateral control and more sophisticated architecture of a true control system could increase its effectiveness for the gust load calculations. Optimizing the gain selection algorithm could possibly also improve results, and simplifying the selection procedure could deem it more user-friendly. However, more thorough investigation of the sensitivity margins for the gains would be necessary to assess their impact on aircraft performance.
Gust load computations using CFD can enhance the understanding of gust loads obtained through panel methods, providing new insights, and enabling further investigations on the limitations of panel methods, particularly for supersonic configurations.

Bibliography

[1] Aigner, B., Peter, F., and Stumpf, E., “Assessment of Electromechanical Flight Control Actuators with Regard to direct Operating Costs,” presented at the Deutscher Luft- und Raumfahrtkongress, 2016.

[2] Albano, E., and Rodden, W., “A Doublet Lattice Method for Calculating Lift Distributions on Oscillating Surfaces in Subsonic Flows,” presented at the AIAA Journal, 1968, vol. 7.

[3] Austin, W. H., “Development of Improved Gust Load Criteria for United States Air Force Aircraft,” US Air Force Systems Command, Ohio, Technical Report SEG-TR-67-28, Sep. 1967.

[4] Barfield, A. F., “Multivariable Control Laws for the AFTVF-16,” presented at the AlAA 22nd Aerospace Sciences Meeting, Ohio, 1984.

[5] Barham, R. W., “Thrust Vector Aided Maneuvering of the YF-22 Advanced Tactical Fighter Prototype,” presented at the AIAA, 1994, vol. 2105–454.

[6] Barry, Frank. W., “Development of Atmospheric Gust Criteria for Supersonic Inlet Design,” NASA, Conneticut, Final Contract Report NAS 2-4515, Dec. 1968.

[7] Bauer, J. E., Clarke, R., and Burken, J. J., “Flight Test of the X-29A at High Angle of Attack: Flight Dynamics and Controls,” Dryden Flight Research Center, NASA, Edwards, California, Technical Paper 3537, 1995.

[8] Becker, J., “Gust Load Prediction and Alleviation on a Fighter Aircraft,” NATO AGARD, France, Report 728, Jun. 1986.

[9] Blair, M., Canfield, R., and Roberts, R., “A joined-wing aeroelastic design with geometric non-linearity,” *JoA*, 2005.

[10] Brockhaus, R., *Flugregelung*, 3. Edition., vol. 1. Heidelberg: Springer, 2011.

[11] Buttrill, C., Zeiler, T., and Arbuckle, P., “Nonlinear simulation of a flexible aircraft in maneuvering flight,” presented at the Flight Simulation Technologies Conference, Guidance, Navigation, and Control, 1987.

[12] Card, V., and Barnes, T. J., “Trends in Certification Procedures and Design Analysis,” NATO AGARD, France, Manual 317, 1991.

[13] Chakraborty, I., Mavris, D. N., Emeneth, M., and Schneegans, A., “A Methodology for Vehicle and Mission Level Comparison of More Electric Aircraft Subsystem Solutions - Application to the Flight Control Actuation System,” presented at the SAGE journal, United States, 2014, vol. 229, pp. 1088–1102, https://doi.org/10.1177/0954410014544303.

[14] Chalk, C., “Fixed-Base Simulator Investigation of the Effects of L and True Speed on Pilot Opinion of Longitudinal Flying Qualities,” Wright-Patterson AFB, Ohio, Technical Report 63–399, 1963.

[15] Chapman, R., “Dynamic Loading Considerations in Design of Modern Combat Aircraft,” presented at the AGARD Structures and Materials Panel, Florence, Italy, 1996.

[16] Charrier, J., and Kulshreshtha, “Electric Actuation for Flight and Engine Control System: Evolution, Current Trends and Future Challenges,” in *No. AIAA 2007-1391*, Nevada, 2007.

[17] Chen, P.-C., and Liu, D. D., “A harmonic gradient method for unsteady supersonic flow calculations,” *Journal of Aircraft*, vol. 22, no. 5, pp. 371–379, 1985.

[18] Donley, P., “Summary of Information Relating to Gust Loads on Airplanes,” Langley Research Center, NACA, Hampton, Virginia, 1950.

[19] Duda, H., “Effects of Rate Limiting Elements in Flight Control Systems - A New PIO-Criterion,” presented at the American Institute of Aeronautics and Astronautics, Braunschweig, Germany, 1995, vol. 95.
[20] Duven, J. E., “Advisory Cicular: Dynamic Gust Loads,” FAA, Advisory Circular 25.341–1, Dec. 2014.
[21] EASA, “CS23 - Easy Access Rules for Normal, Utility, Aerobatic and Commuter Category Aeroplanes.” Jun-2018.
[22] EASA, “CS25 - Easy Access Rules for Large Aeroplanes.” Nov-2018.
[23] Ehernberger, L. J., “High altitude turbulence for supersonic cruise vehicles,” Dryden Flight Research Center, NASA, Edwards, California, Technical Memorandum 88285, 1987.
[24] Elshabasy, M. M., “Mitigating Crack Propagation in a Highly Maneuverable Flight Vehicle Using Life Extending Control Logic,” Old Dominion University, Viriginia, 2009.
[25] Erickson, L. L., “Panel Methods - An Introduction,” Ames Research Center, NASA, California, Technical Paper 2995, 1990.
[26] European Aviation Safety Agency, “Easy Access Rules for Large Aeroplanes (CS-25) (Initial issue).” European Aviation Safety Agency, Nov-2018.
[27] FAA, “FAR25 - Airworthiness Standards: Transport Category Airplanes.” FAA, 2019.
[28] FAA, “Tentative Airworthiness Standart for Supersonic Transports.” Jan-1971.
[29] Fuller, J. R., “Evolution and Future Development of Airplane Gust Loads Design Requirements,” presented at the World Aviation Congress, Anaheim, CA, USA, 1997.
[30] Gern, F. H., Inman, D. J., and Kapania, R. K., “Computation of Actuation Power Requirements for SmartWings with Morphing Airfoils,” presented at the AIAA Journal, Virginia, 2005, vol. 43.
[31] Gibson, D. H., “Evolution of F-16 Loads and Requirements,” presented at the Loads and Requirements for Military Aircraft, Florence, Italy, 1997.
[32] Gilbreath, G. P., “Prediction of Pilot Induced Oscillations (PIO) Due To Activator Rate Limiting Using the Open-Loop Onset Point (OLOP) Criterion,” Air Force Institute of Technology, Ohio, 2001.
[33] Grantham, W. D., Nguyen, L. T., and Neubauer, M. J., “Simulator Study of the Low-Speed Handling Qualities of a Supersonic Cruise Arrow-Wing Transport Configuration During Approach and Landing,” Langley Research Center, NASA, Edwards, California, 1960.
[34] Haghighat, S., Liu, H. H. T., and Martins, J. R. R. A., “A Model-Predictive Gust Load Alleviation Controller for a Highly Flexible Aircraft,” in *Journal of Guidance, Control, and Dynamics*, 2012, https://doi.org/10.2514/1.57013.
[35] Handojo, V., “Contribution to Load Alleviation in Aircraft Predesign and Its Influence on Structural Mass and Fatigue,” Technische Universität Berlin, Göttingen, 2020.
[36] Handojo, V., and Klimmek, T., “Böenlastanalyse der vorwärts gepfeilten ALLEGRA-Konfiguration,” presented at the Deutscher Luft- und Raumfahrtkongress 2015, Göttingen, 2015.
[37] Hoblit, F. M., *Gust Loads on Aircraft: Concepts & Applications*. AIAA, 1988.
[38] Holzapfel, F., “Flugsystemdynamik II,” presented at the Lecture of the Institute for Flight System Dynamics, Technical University of Munich. Germany., 2011.
[39] Houbolt, J. C., “Manual on the Flight of Flexible Aircraft in Turbulence,” NATO AGARD, France, Manual 317, 1991.
[40] Houbolt, J. C., and Press, H., “Some Applications of Generalized Harmonic Analysis to Gust Loads on Airplanes,” *JAS*, vol. 22, no. 1, 1955.
[41] Jensen, S. C., Jenney, G. D., and Dawson, D., “Flight Test Experience With An Electromechanical Actuator On The F-18 Systems Research Aircraft,” Dryden Flight Research Center, NASA, Edwards, California, Conference Paper H-2425, Oct. 2000.

[42] Kaminski, M., “A Rapid Robust Fault Detection Algorithm for Flight Control Reconfiguration,” Technical University Munich, Munich, 2017.
[43] Katz, J., and Plotkin, A., *Low-speed aerodynamics: from wing theory to panel methods*. New York: McGraw-Hill, 1991.
[44] Khodaparast, H. H., and Cooper, J. E., “Rapid Prediction of Worst-Case Gust Loads Following Structural Modification,” presented at the AIAA, 2014, vol. 52, p. 13.
[45] Klimmek, T., “Parameterization of topology and geometry for the multidisciplinary optimization of wing structures,” presented at the CEAS 2009 - European Air and Space Conference, Manchester, UK, 2009.
[46] Klimmek, T., “Parametric Set-Up of a Structural Model for FERMAT Configuration for Aeroelastic and Loads Analysis,” *Journal of Aeroelasticity and Structural Dynamics*, vol. 3, pp. 31–49, 2014.
[47] Lighthill, M., and Newman, M., “On boundary layers and upstream influence. I. A comparison between subsonic and supersonic flows,” 1953.
[48] Liu, D. D., James, D. K., Chen, P.-C., and Pototzky, A. S., “Further studies of harmonic gradient methods for supersonic aeroelastic applications,” *Journal of Aircraft*, vol. 28, pp. 598–605, 1991.
[49] Liu, D. D., Silva, R., and Chen, P.-C., “Transonic AIC Weighting Method using Successive Kernel Expansion,” presented at the Structural Dynamics and Materials Conference, 2005.
[50] Love, B. J., and Ehernberger, L. J., “High Altitude Gust Acceleration Environment as Experienced by a Supersonic Airplane,” NASA, Washington D.C., Technical Note TN D-7868, Jan. 1975.
[51] Luber, W., Becker, J., and Sensburg, O., “The Impact of Dynamic Loads on the Design of Military Aircraft,” presented at the AGARD Structures and Materials Panel, Florence, Italy, 1996.
[52] MSC Software Corporation, “MSC Nastran 2021 - Aeroelastic Analysis User’s Guide.” 2021.
[53] Murrow, H. N., Pratt, K. G., and Houbolt, J. C., “NACA/NASA Research Related to Evolution of U. S. Gust Design Criteria,” presented at the AIAA Structures, Structural Dynamics and Materials Conference, 1989, vol. 4.
[54] National Research Council, “Understanding and Preventing Unfavorable Pilot-Vehicle Interactions,” Aeronautics and Space Engineering Board, Commission on Engineering and Technical Systems, National Research Council, Washington D.C., 1997, http://nap.edu/5469.
[55] NATO, “Flight Control Design – Best Practices,” NATO RTO, France, Technical Report 029, 2000.
[56] Naval Aviation Schools Command, “Fudnamentals of Aerodynamics - Trainee Guide.” Naval Aviation Schools Command, Apr-2017.
[57] Neubauer, M., and Günther, G., “Aircraft Loads,” presented at the RTO AVT Lecture Series on “Aging Aircraft Fleets,” Sofia, Bulgaria, 2000.
[58] Nguyen, L. T., Ogburn, M. E., Gilbert, W. P., Kibler, K. S., Brown, P. W., and Deal, P. L., “Simulator Study of Stall/Post-Stall Characteristics of a Fighter Airplane With Relaxed Longitudinal Static Stability,” Langley Research Center, NASA, Hampton, Virginia, Technical Paper 1538, Dec. 1979.
[59] Noback, R., “Comparison of discrete and continuous gust methods for the determination of airplane design loads,” presented at the ICAS, Amsterdam, Netherlands, 1984, vol. 4.3.2.
[60] Numerous Authors, “Preliminary Design Aspects of Military Aircraft,” presented at the NATO AGARD Conference No.62, The Hague, 1970.
[61] Peckham, C. G., “A Summary of Atmospheric Turbulence recorded by NATO Aircraft,” NATO AGARD, France, Technical Report 586, 1971.
[62] Pike, J., “F-22 Raptor Weapons,” *Global Security*, 2016. https://www.globalsecurity.org/military/systems/aircraft/f-22-weapons.htm.

[63] Pototzky, A. S., and Moses, R. W., “A Method to Analyze Tail Buffet Loads of Aircraft,” in *RTO-AVT-123*, Budapest, Hungary, 2005.
[64] Pratt, K. G., “A Survey of Active Controls Benefits to Supersonic Transports,” NASA, Langley Research Center Hampton, Virginia, Technical Note, Aug. 1976.
[65] Pratt, K. G., and Walker, W. G., “A revised Gust-Load Formula and a re-evaluation of V-G data taken on Civil Transport Airplanes from 1933 to 1950,” NACA, Langley Research Center Hampton, Virginia, 1206, 1954.
[66] Press, H., “An Approach to the Prediction of the Frequency Distribution of Gust Loads on Airplanes in Normal Operations,” NACA, Langley Research Center Hampton, Virginia, Technical Note 2660, Apr. 1952.
[67] Prosser, M., Williams, P., Marlton, G., and Harris, R., “Evidence for Large Increases in Clear-Air Turbulence Over the Past Four Decades,” *American Geophysical Union*, Jun. 2023.
[68] Quero-Martin, D., “DLM Unsteady Correction Using Non Linear CFD Gust Aerodynamics,” Deutsches Zentrum für Luft- und Raumfahrt, Institut für Aeroelastik, 2014.
[69] Rasmussen, C., Canfield, R., and Blair, M., “Joined-wing sensorcraft configuration design.,” *Journal of Aircraft*, 2009.
[70] Rhode, R., and Lundquist, E., “Preliminary study of applied load factors in bumpy air,” NACA, Technical Report 374, 1931.
[71] Riccius, R., “Designer’s View on Structural Problems,” in *No. 62*, France, 1970, vol. 62, p. 306.
[72] Roberts, B. J., “Sytem and Method for Flaperon and/or Aileron Control,” EP 3 363 730 A1.
[73] Rodden, W., Kalman, T., and Giesing, J., “Application of the Doublet-Lattice Method and the Method of Images to Lifting-Surface/Body Interference,” Technical Report AD893825, 1972.
[74] Roger, K. L., “Airplane Math Modeling Methods For Active Control Design,” presented at the AGARD-CP-228, 1977.
[75] RTO Task Group, “Design Loads for Future Aircraft,” NATO RTO, France, Technical Report 45, Feb. 2002.
[76] Rumpfkeil, M., and Beran, P., “Gust Simulations and Optimizations for an Efficient Supersonic Air Vehicle,” presented at the AIAA SciTech Forum, San Diego, CA, 2022, p. 14.
[77] SAAB, “A future-proof fighter jet,” *SAAB Stories*, May-2020. https://www.saab.com/newsroom/stories/2019/may/a-future-proof-fighter-jet.
[78] Smith, J. W., “Analysis of a Lateral Pilot-Induced Oscillation Experienced on the First Flight of the YF-16 Aircraft,” Dryden Flight Research Center, NASA, Edwards, California, Technical Memorandum 72867, Sep. 1979.
[79] Smith, J. W., Lock, W. P., and Payne, G. A., “Variable-Camber Systems Integration and Operational Performance of the AFTI/F-111 Mission Adaptive Wing,” Dryden Flight Research Center, NASA, Edwards, California, Technical Memorandum 4370, Apr. 1992.
[80] Staff of the Flight Research Center, “Experience with the X-15 Adaptive Flight Control System,” Dryden Flight Research Center, NASA, Edwards, California, TN D-6208, Mar. 1971.
[81] Stevens, B., and Lewis, F., *Aircraft Control and Simulation*, 2nd ed. John Wiley & Sons, 2003.
[82] Thormann, R., and Dimitrov, D., “Correction of aerodynamic influence matrices for transonic flow,” 2014.
[83] Tolefson, H. B., “Summary of Derived Gust Velocities Obtained from Measurements within Thunderstorms,” NACA, Langley Research Center Hampton, Virginia, Technical Note 1285, Jul. 1955.
[84] US Department of Defense, “JSSG-2006 - Aircraft Structures.” 30-Oct-1998.
[85] US Department of Defense, “MIL-A-8861B - Airplane Strength and Rigidity Flight Loads.” 07-Feb-1986.

[86] US Department of Defense, "MIL-DTL-9490 - Flight Control Systems - Design, Installation And Test Of Piloted Aircraft." 2008.
[87] US Department of Defense, "MIL-F-8785C - FLYING QUALITIES OF PILOTED AIRPLANES." 1980.
[88] US Department of Defense, "MIL-HDBK-530-2 - Aircraft Usage and Service Loads Statistics." 2019.
[89] US Department of Defense, "MIL-STD-1797A - Flying Qualities of Piloted Aircraft." 1990.
[90] US Department of Defense, "MIL-STD-3013B - Glossary of Definitions, Ground Rules and Mission Profile." 01-Sep-2022.
[91] Van den Bossche, D., "The A380 Flight Control Electrohydrostatic Actuators, Achievements And Lessons Learnt," presented at the 25TH INTERNATIONAL CONGRESS OF THE AERONAUTICAL SCIENCES, Hamburg, 2006.
[92] Vechtel, D., Hauber, B., and Looye, G., "Analysis of a multi-functional high-lift system driven by an active differential gear box," presented at the German Aerospace Congress, Stuttgart, 2013.
[93] Voß, A., "An Implementation of the Vortex Lattice and the Doublet Lattice Method," Deutsches Zentrum für Luft- und Raumfahrt, Institut für Aeroelastik, Göttingen, Oct. 2020.
[94] Voß, A., "Design and Structural Optimization of a Flying Wing of Low Aspect Ratio Based on Flight Loads," Technische Universität Berlin, Göttingen, 2020.
[95] Voß, A., "Loads Kernel User Guide Version 1.03," Deutsches Zentrum für Luft- und Raumfahrt, Institut für Aeroelastik, Göttingen, 136, Oct. 2020.
[96] Voß, A., and Klimmek, T., "Aeroelastik Modeling, Loads Analysis and Structural Design of a Fighter Aircraft," presented at the ICAS 33 Congress, Stockholm, Sweden, 2022, p. 18.
[97] Voß, A., and Klimmek, T., "Parametric aeroelastic modeling, maneuver loads analysis using CFD methods and structural design of a fighter aircraft," *Elsevier*, vol. 136, Mar. 2023.
[98] Walker, W. G., "Summary of Revised Gust-Velocitiy Data Obtained from V-G Records taken on Civil Transport Airplanes," NACA, Langley Research Center Hampton, Virginia, Technical Note 3041, Nov. 1953.
[99] Waszak, M., Buttrill, C., and Schmidt, D., "Modeling and Model Simplification of Aeroelastic Vehicles: An Overview," NASA, Langley Research Center Hampton, Virginia, Technical Report 107691, 1992.
[100] Waszak, M., and Schmidt, D., "Flight dynamics of aeroelastic vehicles," 1988.
[101] Williams, J., and Page, R. K., "Some Fluid-Dynamics Considerations Realting to the Preliminary Design of Combat Aircraft," in *No. 62*, France, 1970, vol. 62, p. 306.
[102] Wilson, E. B., and Hunsacker, J. C., "Theory of an Aeroplane Entering Gusts," NACA, Technical Report 1, 1915.
[103] Xu, J., "Aircraft Design with Active Load Alleviation and Natural Laminar Flow," Stanford University, Stanford, 2012, http://purl.stanford.edu/hz528zb1688.
[104] ZONA Technology Inc., "ZAERO - User's Manual." ZONA Tech. inc., 2019.